COLLISION INDUCED SELF ORGANIZATION IN SHAPE CHANGING ROBOTS

A Dissertation
Presented to
The Academic Faculty

By

Akash Vardhan

In Partial Fulfillment
of the Requirements for the Degree
Doctor of Philosophy in the
School of Physics

Georgia Institute of Technology

May 2025

COLLISION INDUCED SELF ORGANIZATION IN SHAPE CHANGING ROBOTS

Thesis committee:

Dr. Daniel I. Goldman, Advisor
School of Physics
Georgia Institute of Technology

Dr. Dana Randall
College of Computing
Georgia Institute of Technology

Dr. Kurt Wiesenfeld
School of Physics
Georgia Institute of Technology

Dr. Kirsten H. Petersen
Electrical and Computer Engineering
Cornell Engineering

Dr. D. Zeb Rocklin
School of Physics
Georgia Institute of Technology

Date approved: 25th April 2025

To the source: That which arises through me, I offer to you in reverence.

For my Parents, Teachers & Bros.

Collision induced self-organization in shape-changing robot collectives

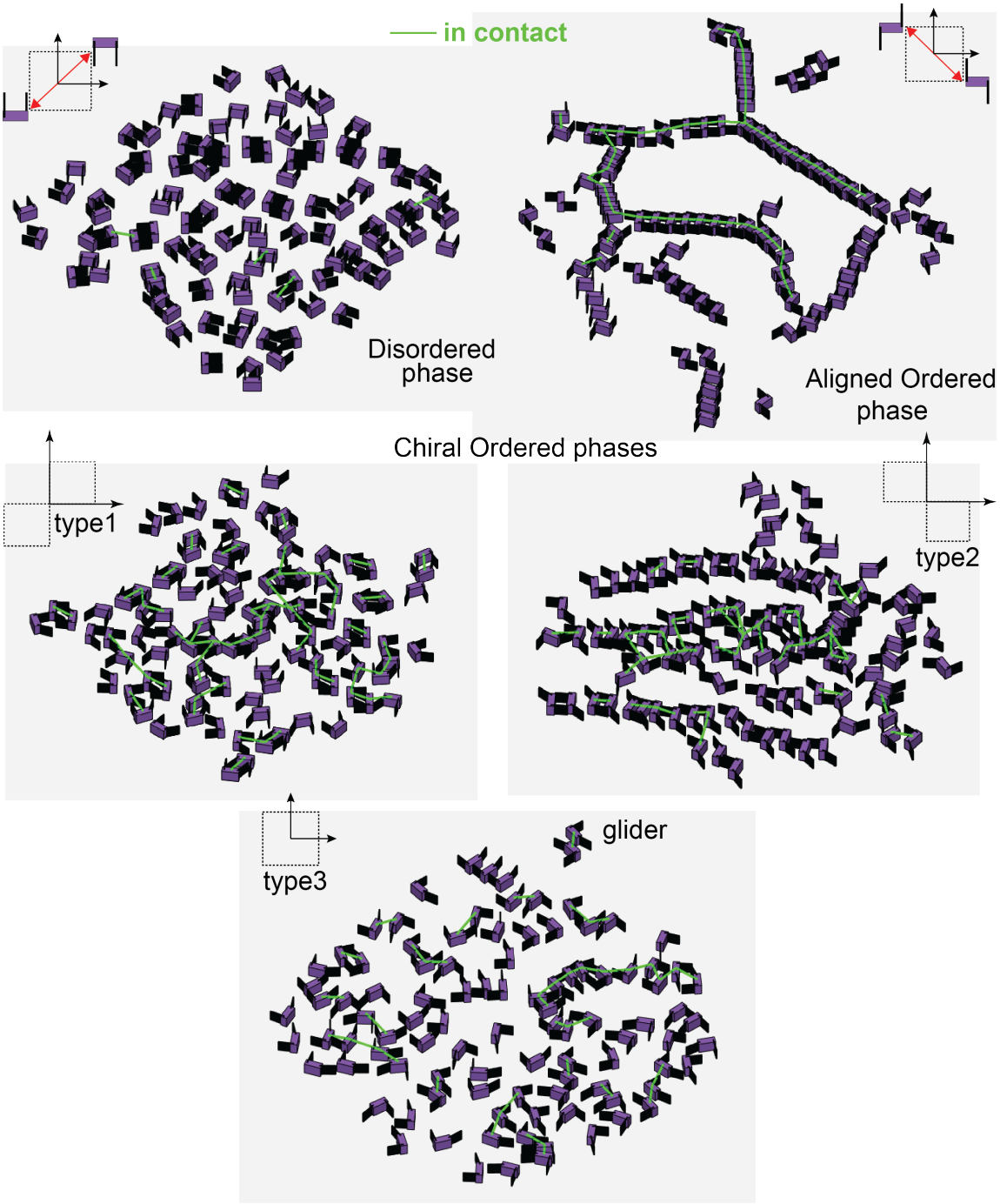

ACKNOWLEDGMENTS

I am sincerely grateful to my advisor, Prof. Daniel I. Goldman, for accepting a misfit like me into his wonderland of exotic nonlinear dynamics and reviving a long-forsaken dream of pursuing a PhD in physics. His steady support, especially during my most difficult moments, kept me grounded. I am especially thankful for his constant encouragement to think more clearly, synthesize ideas more deeply, and communicate more effectively—not just to do science, but to truly understand and explain it. I also admire his unwavering commitment to finding joy in scientific exploration, even during challenging times, and, of course, the dependable supply of donuts that sweetened our group meetings.

I thank Prof. Joshua Weitz for bringing me into the QBioS program and for his distinctive Foundations of Quantitative Biosciences course, which introduced me to computational modeling across biological scales. I am especially grateful for his early funding support during a period of uncertainty in my dissertation direction—it gave me the space to explore and ultimately pivot to Physics.

I am grateful to my committee members: Prof. Kurt Wiesenfeld, for his warmth, mentorship, and for steering me toward the gliders project that shaped this dissertation. I also thank him for his lucid teaching of Statistical Mechanics II, which offered a sweeping and insightful overview of the field. Prof. Zeb Rocklin, for his astute insights on symmetry breaking, for showing me how to build and test ideas from first principles, and for heroically driving through snowstorms in Aspen. Prof. Dana Randall, for for curating engaging weekly Muri discussions on emergence in distributed systems-and for two wonderful in person meetings. Prof. Kirstin Petersen and her student Danna, for the fun yet insightful robotic experiments that contributed to the penultimate chapter. Prof. Predrag Cvitanović, for his energy, flair, and unwavering belief in the power of symmetry reduction to make sense of dynamics.

I'm thankful to ARO MURI, the School of Physics and the QBios graduate program

for supporting my research and travel during the course of this dissertation. Huge thanks to Prof. Ed Greco for graciously overlooking my TA blunders—your patience deserves its own award. And to Gary LongStreet and Lisa Redding, thank you for rescuing me from the clutches of missed deadlines and getting me back in classes like true registration superheroes. I owe you all snacks, gratitude, and fewer mistakes.

I thank Prof. Simon Sponberg and Prof. Flavio Fenton for their engaging Neurophysics course, which offered a concise and compelling introduction to biophysics. I am deeply grateful to my mentors, Professors Namrata Gundiah and Sanjay Sane, for offering me refuge when I was disillusioned with industry, for ushering me into biomechanics and pointing me to a graduate program that provided such profound exposure to dynamical systems. Their scientific and personal generosity was invaluable. The camaraderie in their labs made that phase not just intellectually rich, but genuinely fun and full of shenanigans. Thanks to Avi and Sidhu for their bursts of amusement—looking forward to lively scientific exchanges ahead. I also thank Prof. Sandeep Krishna for illuminating conversations on coupled oscillator models in living systems—discussions that inspired me to seek the mechanisms underlying self-organized synchronized states in diverse systems governed by nontrivial couplings.

I am indebted to my undergraduate mentors, Prof. Jayanta Kumar Dutt and Prof. Anindya Sundar Das, for introducing me to research through nonlinear vibrations and control theory. Huge thanks to Dr. Ram Avinery, Dr. Hridesh Kedia, and Dr. Shengkai Li for their mentorship, sharp acumen, critical discussions and contributions, which enriched the gliders project—especially Ram and Shengkai, for exhorting me to refine my algorithmic thinking. I thank Venny, Tianyu, and Daniel for their valuable input and contributions during the design and implementation of the contact-sensing-enabled smarticles and for their ingenuity in designing and experimenting with highly advanced robots. I thank Dr. Hosain Bagheri for his valuable input in refining the manuscripts that form the core of this work and his vibrating ants. I'm grateful to Dr. Luning Fang and Prof. Dan Negrut for guiding

us through collision handling in Chrono and helping us compare results across different solvers. I thank Dr. Pavel Chvykov for showing me how to design tabletop experiments for testing theoretical predictions, and Dr. Chvykov, Dr. Zachary Jackson, and Aryaman Jha for many stimulating discussions on statistical and nonlinear physics in the context of smarticles. To all my labmates—from high schoolers and undergrads to postdocs—thank you for your dedication and the inspiration you brought to this journey. I learned a great deal simply by observing the problems you tackled and how creatively you solved them. My utmost thanks to Prof. Tanvi Deora for teaching me dissections, Micro-CT, and sharing her exuberant drive for science. And to Abin Ghosh—for introducing me to high-speed videography and being a fun dude to work with.

I appreciate my high school teachers—Partho, Baby, and Maity Sir—for making Physics and Math exciting, and for crafting some of the most notorious exam problems in Calcutta.

At every stage of my life, mother nature spontaneously self-assembled a crew of criminally gifted, gloriously ungovernable souls—Raj (unlicensed genius), Binku (late bloomer), Omi (totally domesticated now), Jeet (reformed but still dangerous), Mamba (machismo), Haldaar (ticking inferno), Pritesh (domesticated in body, never in spirit), Ishu (thirsty alligator), Sir (the one and only) , Tupan (forging boys into men), Simca (glutes God) , Ritwik (toddlerfaced kingpin), Banjo (such a prettyboy), Subho Da (nightingale of Tollygunge), Thakur (maverick) , Bhaam (beast with horns), Swaggy (beyond redemption now), Suraj (batting masterclass), PaaJi(coal-dusted comedy), SharmaJi (silken voiced rogue), Vats (vandal vagabond), Saxena (artillery addict), Dinesh (rebel in residence), Abin (honor roll outlaw), Leo (legend), Brantt (charms unlimited) and Gman (ghetto superstar)—you scoundrels turned this lifetime into a beautiful, feral rampage. Deepest thanks to Omi, Parna, and the newest recruit, Lio, for being my home away from home—and to Parna, for her culinary magic.

Shout-out to Leo Prinzi for his steadfast brotherhood, service-minded spirit, and to his family for their open-heartedness; to the SigEp boys for welcoming me as an honorary

member; and to the Food4Lives volunteer squad for making Saturdays in Atlanta unforgettable. To Soniya, for her stream of good food and bad humor. Thanks to Keli, Fabian, Adiel Enrique, and Margot for the fun hangouts. I extend my gratitude to Margot and her family for their kind hospitality during my visit to LA. I'm grateful to Aditya, Dida, and the late Brother Shankara for their uplifting company as housemates. I'm grateful to the Griffins for being understanding and accommodating landlords and to Shivank and Agniva for being considerate housemates. To Amita Balaram, for all the lunch boxes and his friendship. To Dr. Andras Karsai, for his excellent presentation skills and dead-lifting ability. To Dr. Baxi Chong, for his dissemination of geometric mechanics. To Dr. Chris Pierce, for his pleasant demeanor and cheerful whistling. To Lila, for her fiery intensity and dangerously good desserts. To Madison, for her unswerving effort to bring happiness to those around her. To Enda, for sharing his frustrations. To Astou, for constantly checking in. And to Steven, for his lip-smacking heritage sweets that left me wanting more. Big thanks to Thakur for his relentless reality checks and for stepping in when support was needed most.

To Veda and Todd (Roderick), for helping instill the habits of consistency, humility and detachment — and to my fellow practitioners, who show up every morning with steady commitment, rain or shine — thank you!

To my baby sisters — Meghna, Shelly, Shambhavi, Mansi, and Nandini — and baby brothers — Piyush, Harsh, Monkey, Nishu, Shubham, Shivam, and Shrey — your boundless love and adoration mean the world to me.

To my family, who supported every decision I made — Nani, and Nana, Baba, and Dadi, wherever you are — thank you for your unconditional love. And to my father, for instilling the virtues of integrity, dedication, and self-mastery — thank you for laying the foundation, Paa.

And lastly, to my mother—my hero since day one. For giving up a flourishing career to focus on family. For being my pillar of support, and for sowing in me the seeds of academic pursuit with your own PhD—this is for you, Maa.

TABLE OF CONTENTS

LIST OF TABLES

LIST OF FIGURES

SUMMARY

This dissertation investigates the emergence of collective behaviors in active, shape-changing robotic particles that interact via collisional impacts on a Coulomb friction substrate. These robots, inspired by the granular materials (GM) paradigm, belong to a broader class of systems characterized by macroscopic, discrete, athermal, and dissipative particles. While granular materials have traditionally been composed of passive convex particles, incorporating internal actuation and concave geometries—such as in staple-inspired three-link robots—opens new avenues for exploring how shape and gait coordination enable dynamic self-organization and emergent material properties.

An initial study demonstrated the selection of low-rattling states in a pinned collective of three planar shape-changing robots. Synchronized and repeatable motion patterns were observed, resulting from the coupled influence of internal actuation and environmental constraints. This interplay between drive and environment was crucial in guiding the system toward dynamically stable configurations—a feature common to many high-dimensional dynamical systems with effectively random components, where some regions in the huge parameter space causally give rise to self-organized, low-rattling behavior on the macroscale, while surrounding regimes remain chaotic and unpredictable. This study laid the groundwork for the investigations that form the core of this dissertation.

The next project explores the binding mechanism of the minimal interaction unit: a pair of shape-changing robots. Through experiments and simulations, we demonstrate a nontrivial binding mechanism in which dynamically coordinated, yet locally repulsive, collisions produce long-lived, mobile gliders. These gliders spontaneously emerge from unconfined ensembles, exhibit two distinct asymmetric configurations, and persist for hundreds of actuation cycles. We identify a novel dynamical attraction mechanism resulting from appropriately timed and oriented repulsive contacts. Notably, shape-induced concavity plays a critical role in stabilizing these bound structures, with tactile feedback enabling

real-time modulation of inter-robot coordination.

Building upon this, the subsequent project investigates the transport properties and symmetry-breaking dynamics of these gliding dyads. We analyze how shape oscillations and internal gait symmetries control collective motion. In particular, we show that non-reciprocal square gaits, which break time-reversal symmetry, generate robust translation through non-commutative displacements in configuration space. By systematically increasing gait area, we map transitions between bound states, showing how locomotion onset and mode stability depend on the symmetry of internal dynamics. Remarkably, dyad trajectories acquire chirality under time-irreversible actuation, enabling steerable motion with minimal feedback via gait inversion. These results shed light on the design of self-organizing robotic collectives capable of persistent and programmable locomotion.

The final part of this thesis expands to the many-body regime, where dense robot ensembles self-organize into spatially extended structures such as chains and loops. Simulations reveal that the same principles of concavity-mediated entanglement observed in dyads underpin the formation of these structures with long-range order. The diversity of emergent patterns—from aligned filaments to dynamic, loopy assemblies—is governed by the gait templates executed by individual robots. Further, experiments with a variant of the robot design, limited to asymmetric reciprocal actuation, demonstrate similar clustering behavior. In this case, a passive adhesion mechanism, akin to a velcro strip, reinforces contact and promotes long-range order through mechanically stabilized chains.

These studies demonstrate how active shape change, collisional interactions, and minimal feedback enable self-assembly and transport in robotic granular systems, advancing the design of programmable collectives with emergent, decentralized behavior.

CHAPTER 1
INTRODUCTION

Overview

Granular materials (GM), composed of athermal, dissipative, and macroscopic particles, have long served as a model system for studying emergent behavior in non-equilibrium physics. Through contact interactions alone, passive grains can exhibit clustering, jamming, and transitions between fluid- and solid-like states [1, 2, 3]. Active granular systems extend this landscape by incorporating internal drive, giving rise to richer dynamical phases including motility-induced clustering and spontaneous collective motion—even in the absence of attractive forces [4, 5, 6, 7, 8].

This dissertation advances a third frontier: *shape-changing active granular matter*, where individual agents deform cyclically using internal actuation. Unlike traditional active systems, these particles possess additional internal degrees of freedom, enabling novel interaction modes—particularly when shape and motion are coupled through frictional and collisional dynamics [9, 10, 11]. A key advantage of this framework is that complex emergent behavior can arise even with small numbers of agents, due to the richness of their internal state space and their non-linear, geometry-mediated interactions [12, 13, 14].

Central to this work is the role of *non-reciprocity* in the deformation patterns. Non-reciprocal gaits that trace closed loops in shape space break time-reversal symmetry due to the fixed direction of gait traversal, resulting in non-commutative displacements and enabling directed transport over each cycle [15, 16, 17, 18]. When agents actuated via such templates [19] collide, they exchange time-ordered impulses that can lead to effective attraction and stable, mobile bound states. These collisional and friction mediated dynamics, offer a new route to self-organization via local, antagonistic interactions [20, 21].

Through experiments and simulations of three-link robots on frictional substrates, this thesis explores how *shape-changing templates & collisions* together produce coordinated behaviors: from low-rattling states and glider formation, to symmetry-controlled transport and large-scale chaining. The results illuminate how programmable collective dynamics can emerge from minimal feedback and local rules, with implications for both active matter and robotic material design [22, 23, 24, 25].

Granular Media and Emergent Phenomena

Collisional dynamics form a unifying principle across physics—governing emergent behavior in systems ranging from macroscopic granular assemblies [1, 2] and ultracold quantum gases [26, 27] to particle interactions in the early universe [28]. In classical systems, collisions underlie inelastic collapse, clustering, and jamming transitions [29, 30, 3]; in quantum systems, they dictate scattering cross sections, decoherence, and thermalization [31, 32, 33]; and at cosmological scales, collisional processes in the early universe shape structure formation and relic particle abundances [28]. Across these regimes, collisions not only mediate interactions but also serve as mechanisms for the emergence of collective order in far-from-equilibrium systems.

Granular media (GM) refer to collections of discrete, macroscopic particles interacting primarily via contact forces. These systems are inherently athermal: thermal fluctuations are negligible compared to gravitational or inertial effects, and energy is lost through inelastic collisions and friction. Despite this dissipative character, granular systems exhibit a striking range of collective phenomena: clustering in vibrated layers [1, 2], spontaneous crystallization and compaction [34], convection and segregation under shear [35, 36, 37], and inelastic collapse in driven gases [29, 38, 30].

A hallmark of granular systems is their *ability to transition between fluid-like and solid-like states* depending on density, forcing, and boundary conditions [39, 3]. These transitions—jamming, shear-thickening, dilatancy—are inherently non-equilibrium and often

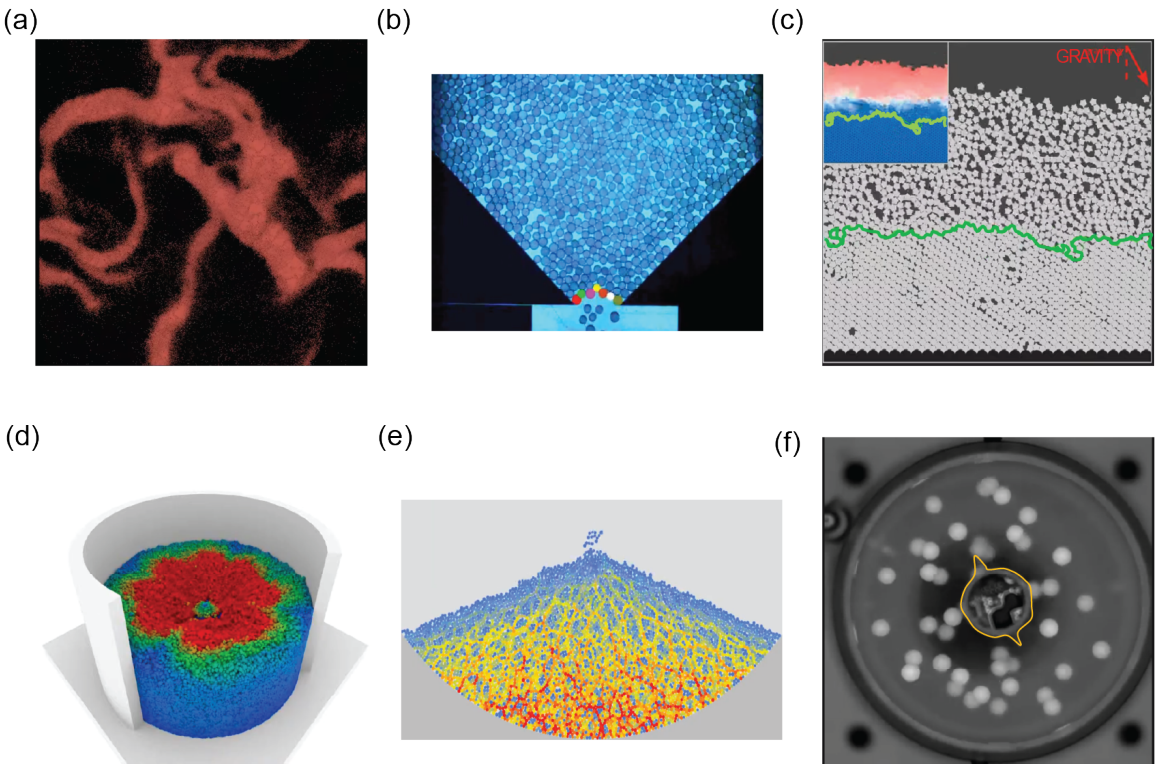

Figure 1.1: Emergent phenomena in granular materials captured from experiments and simulations: (a) Inelastic collapse in a simulation of 100,000 colliding particles [Video]. (b) Jamming of granular flow through a hopper, resulting in intermittent clogging [Video]. (c) Coexistence of solid-like and fluid-like phases in vibrated granular disks [Video]. (d) Large-scale granular mixing of 200,000 rigid bodies in a rotating drum [Video]. (e) Emergence of force chains as grains are slowly poured into a pile [Video]. (f) Directed rotation of a granular ratchet driven by thermal fluctuations [Video].

hysteretic [40, 41]. The jamming transition, in particular, exemplifies how local constraints and dissipation can lead to emergent rigidity in the absence of thermal equilibration [42, 43]. Unlike in molecular fluids, granular flow is governed not by equilibrium statistical ensembles but by the interplay of geometric constraints, contact mechanics, and driving protocols. The force distributions supporting granular solids have been elegantly visualized via photo-elastic force chains [44].

In vibrated granular layers, particles gain mobility from an external energy source (such as a shaking table or vertical tapping), which induces momentum transfer via interparticle collisions. However, a new class of systems—*active granular media*—emerges when particles possess their own source of energy for propulsion or deformation. These active

agents include motorized grains, colloidal particles, self-deforming particles, and internally driven robotic elements. The transition from passively agitated to internally actuated particles mirrors developments in colloidal systems, where externally driven particles—such as those manipulated via optical or magnetic fields—contrast with truly self-propelled ones like Janus colloids, which exhibit autonomous motility due to built-in chemical or physical asymmetries [45].

Biological active matter spans a wide range of systems across length scales. At the microscopic level, examples include motile bacteria, sperm cells, and cytoskeletal filaments propelled by molecular motors [46]. At mesoscopic to macroscopic scales, flocking birds [47, 48], swarming insects, and herds of cattle [49] exhibit emergent collective motion governed by local interactions and alignment rules. These organisms often combine self-propulsion with sensing, memory, and adaptive feedback, allowing them to respond dynamically to their environments.

In contrast to synthetic active matter, which often relies on programmed or physical actuation without intrinsic feedback, biological systems operate with distributed control architectures and energy conversion mechanisms evolved for robustness and adaptability. This distinction not only highlights differences in complexity but also inspires the development of robotic collectives that aim to replicate the rich, lifelike behaviors observed in natural systems [50].

In colloidal active matter, self-organization into non-equilibrium structures such as living crystals [51], active molecules [52, 53], and self-assembly via chemical signaling [54] illustrates how local activity can be harnessed for emergent order. Similar behaviors are observed in macroscopic robotic systems, from Bobbots inspired by living crystals, where magnetic attraction competes with Brownian-driven repulsion [55], and the membrane enclosed robotic swarms comprised of bristlebots [56, 57].

These systems, often described under the umbrella of active matter [46, 6, 58], break time-reversal symmetry at the single-particle level and violate momentum conservation due

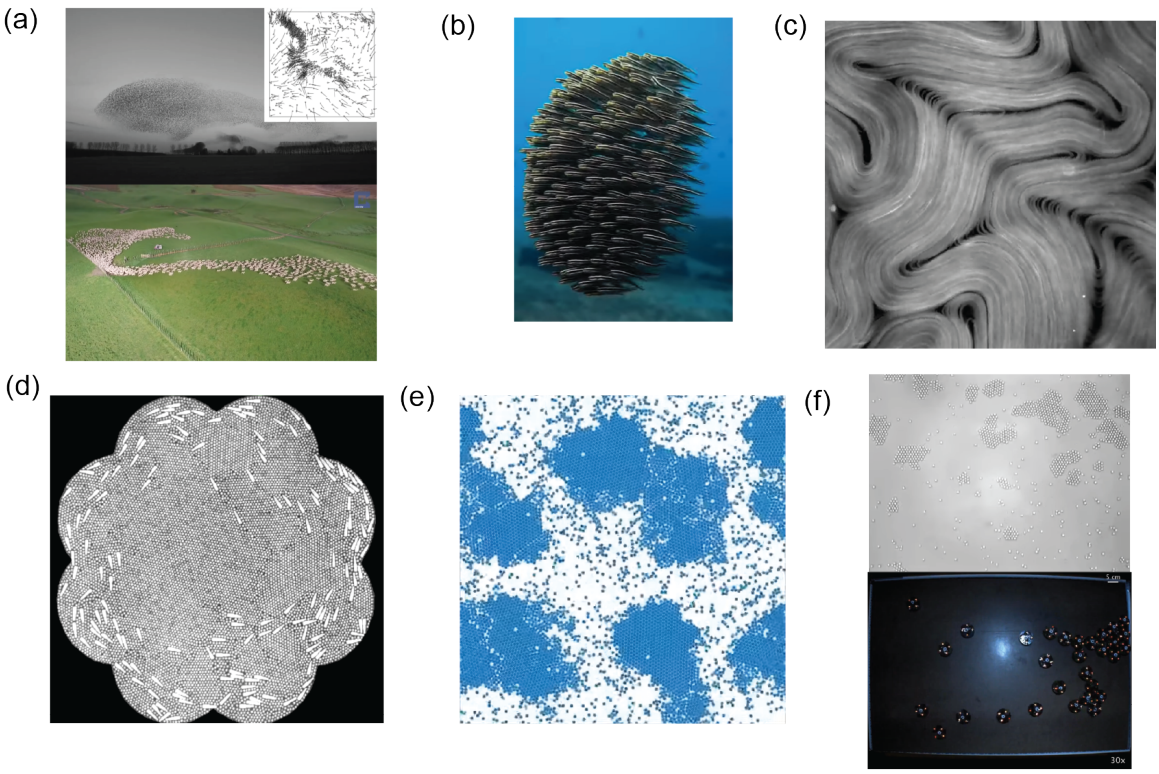

Figure 1.2: Emergent collective phenomena across different scales and systems of active matter, illustrated through experiments and simulations: (a) Large-scale biological flows: flocking in a murmuration of starlings (Top) alongside a simulation of hard inelastic disks to mimic flocking with granular matter (inset) [Starlings Video], and herding dynamics in a group of sheep (Bottom), [Sheep Video]. (b) Synchronized swimming in a school of fish exhibiting coordinated turning and spacing [Fish Video]. (c) Emergence of turbulent swirling and defect dynamics in an active nematic formed by microtubules and motor proteins [Turbulence Video]. (d) Milling behavior in vibrated polar rods interacting via a dissipative granular medium [Milling Video]. (e) Motility-induced phase separation (MIPS) observed in a simulation of self-propelled particles [MIPS Video]. (f) Light-activated colloidal aggregation into dynamic clusters [Living Crystals Video], with a robotic analog in the form of BobBots [BobBots Video].

to substrate interactions and frictional forces. As a result, they exhibit behaviors far from the reach of classical thermodynamics.

One striking consequence of activity is the *emergence of collective motion from purely repulsive interactions*. Systems of vibrated rods [59], self-propelled disks [4], and synthetic swimmers [60, 61] all exhibit pattern formation, swarming, and spontaneous alignment. These systems do not require cohesive forces; alignment and clustering arise from geometry and steric interactions, often mediated by dissipative collisions. A particularly

dramatic example is *motility-induced phase separation (MIPS)*, where self-propelled particles spontaneously separate into dense and dilute phases purely due to their activity [8].

Granular analogs of these phenomena have been observed in shaken layers of polar rods [5], where local actuation leads to the formation of dynamic clusters and persistent currents. In these systems, boundaries and substrates play a central role in shaping collective behavior. For example, bacteria and granular robots tend to accumulate near walls [62, 63], a behavior that emerges from persistent motion and frequent reorientation upon contact. Similarly, "flocking at a distance" has been observed in vibrated granular monolayers [7], where alignment emerges even when particles are not in direct contact—mediated instead by the medium or substrate. These observations underscore the crucial role that boundary enclosures and environmental interactions play in determining emergent dynamics.

Most passive granular materials studied to date consist of convex particles—spheres, rods, and disks—that interact through well-defined contact forces. However, systems composed of *concave or topologically complex* particles offer a rich, underexplored plethora of emergent mechanics. Examples include biological aggregates such as worm blobs [14, 64, 65], bird nests composed of branched twigs [66], bent-staple particles that entangle [67] and entangled cellular or multicellular assemblies [68, 69], where mechanical entanglement, interlocking, and steric frustration generate collective rigidity and support nontrivial phase transitions. These systems possess many internal degrees of freedom and allow for the formation of dynamically stable configurations through geometry-mediated interactions. Their behavior challenges conventional force-chain models and opens new directions for understanding self-assembly and robustness in disordered matter.

Taken together, these studies highlight the *versatility of granular systems as a platform for exploring emergence*, whether in passive, driven, or active regimes. Their minimal ingredients—contact, dissipation, and geometry—give rise to high-dimensional behavior that often defies intuition. As such, granular media serve not only as a physical playground for non-equilibrium statistical mechanics but also as a design framework for robotic collectives

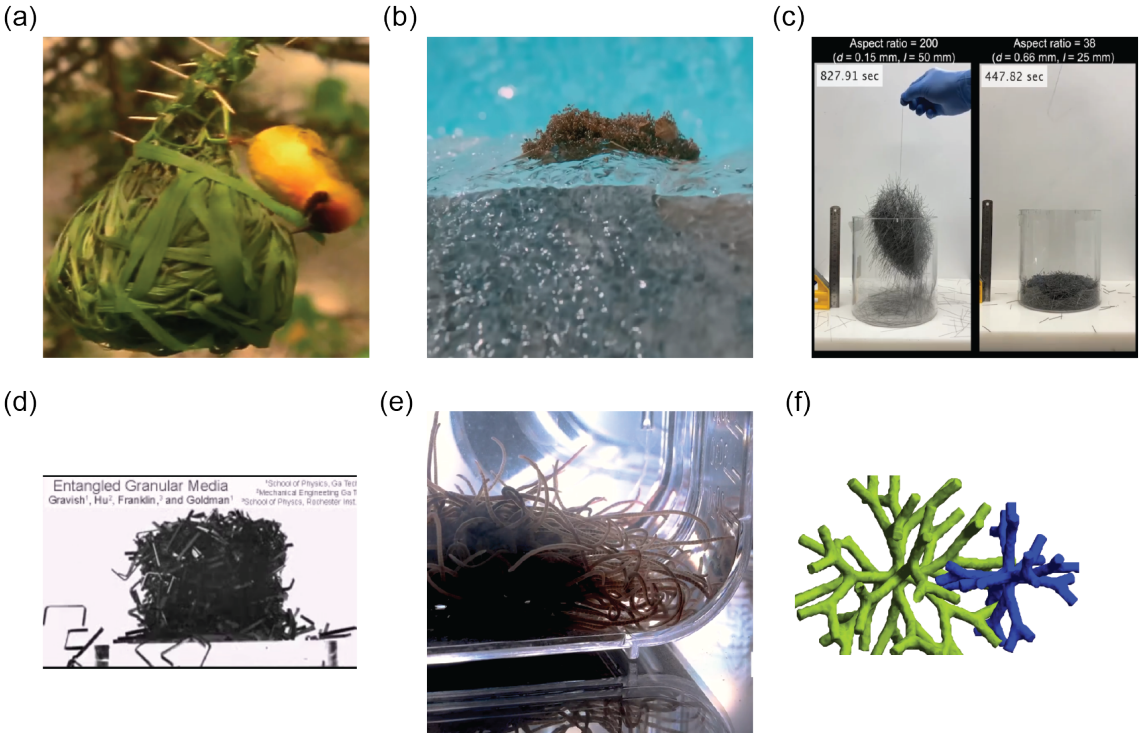

Figure 1.3: Examples of collective structures formed by granular matter or organisms with varying shapes and modes of entanglement: (a) A weaver bird constructs its nest by stitching together grass blades, forming a mechanically interlocked structure [Video]. (b) Fire ants link their bodies to form a floating raft that dynamically adapts to perturbations such as water waves [Video]. (c) A disordered packing of rods demonstrates topological entanglement dependent on aspect ratio, supporting an entanglement transition [SI Video]. (d) Staple-shaped particles form an entangled granular solid with high resistance to deformation under perturbation [SI Video]. (e) California blackworms exhibit active cohesion by self-organizing into highly motile and task-capable blobs [Video]. (f) Engineered multicellular yeast exhibit morphological entanglement via branched growth, enabling the formation of space-filling cohesive structures [SI Video].

and programmable materials.

Emergent Phenomena in Shape-Changing Active Matter

While passive granular systems reveal the power of geometry, contact, and dissipation in driving emergence, active matter systems composed of *shape-changing or internally deformable agents* bring forth a distinct layer of complexity. These systems not only convert internal energy into motion but also dynamically reconfigure their body shape to interact with the environment in adaptive ways [70, 71, 9, 10, 72, 73, 74, 75]. Such capability places

them apart from conventional self-propelled particles, enabling access to high-dimensional control strategies even at low population numbers.

A defining feature of shape-changing active agents is their *intrinsic coupling between internal dynamics and external locomotion*, which gives rise to emergent behaviors even in small collectives. For example, studies on mechanical diffraction in soft robotic metamaterials have shown how geometric constraints and time-asymmetric gaits can produce spatial propagation of motion resembling optical diffraction patterns [12, 76, 13]. Similarly, agents capable of lattice traversal can harness their shape-change cycles to overcome environmental barriers in programmable ways [77], offering pathways for adaptive navigation in obstacle rich terrains [78] leveraging gait design techniques from geometric mechanics.

Beyond locomotion, collective dynamics among such agents can lead to *spontaneous synchronization*, a hallmark of many biological systems. Metachronal wave formation in arrays of cilia and flagella, for instance, exemplifies how internal oscillatory dynamics become phase-locked through hydrodynamic and mechanical coupling [79, 80, 81, 82]. Analogous behavior has been observed in clusters of undulatory robots [83, 84], where the interplay of local sensing and timing control leads to globally coordinated movement. In dense systems of nematodes and synthetic analogs, gait synchronization further manifests as group-level transport and alignment [85, 84, 86, 87].

Shape-changing agents also contribute to the *self-assembly of functional structures*. Biological examples include the formation of worm blobs that act as adaptive materials [14, 64] and ant bridges that solve physical routing problems through distributed coordination [88]. These aggregations exhibit not just robustness, but also responsiveness, adapting their topology and internal state in real time to external stimuli.

To better understand the principles underlying such behavior, researchers have turned to model systems like *Purcell-inspired three-link swimmers* and their robotic counterparts, such as *smarticles* (smart active particles) [15, 11, 22, 89]. While isolated smarticles possess limited motility, their interactions—mediated through collisions, boundaries, and col-

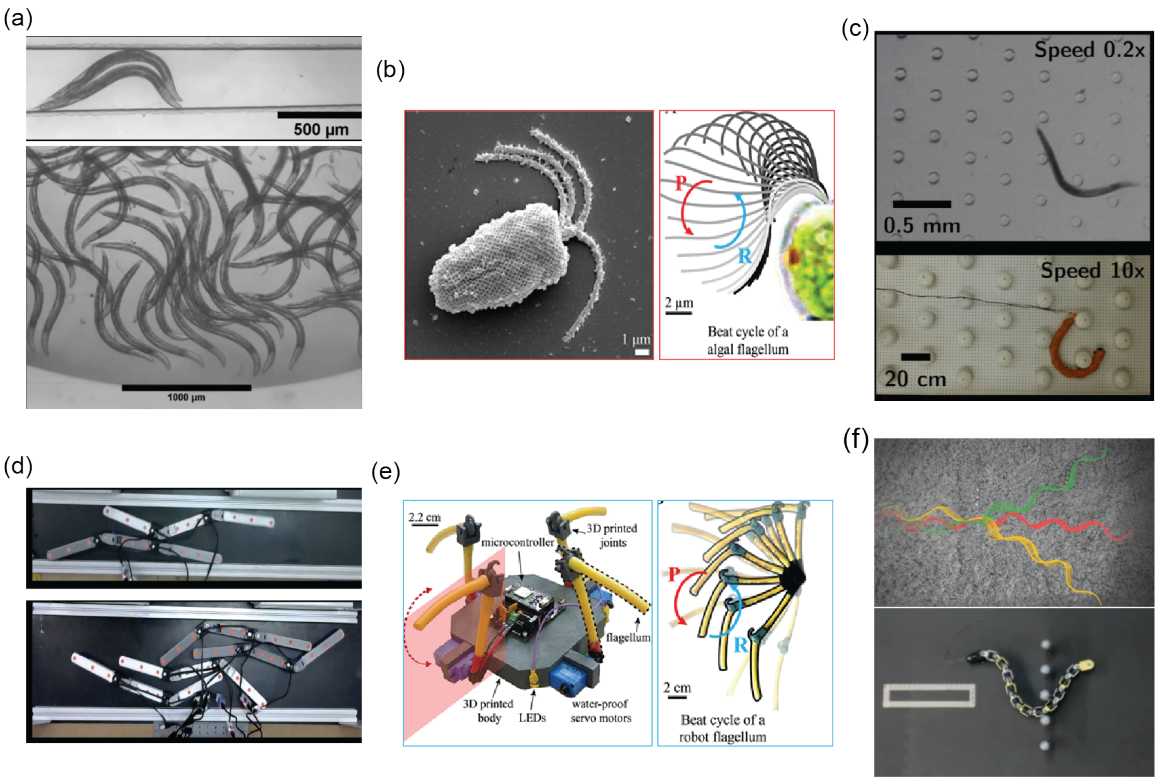

Figure 1.4: Representative examples of emergent phenomena in shape-changing active matter, observed in both biological systems and their robotic analogs: (a) Collision-mediated gait synchronization in dense clusters of nematode worms, leading to the emergence of metachronal waves [SI Video]. (b) A quadri-flagellated alga displaying a coordinated ciliary deformation pattern [SI Video]. (c) Lattice traversal enabled by mechanical intelligence in nematode worms and directionally compliant robotic designs [SI Video]. (d) 3 link swimmers as robotic analogs of nematodes exhibiting contact-mediated longitudinal cohesion via lateral interactions [SI Video]. (e) A minimal robophysical model for investigating principles of quadri-flagellated swimming [SI Video]. (f) Mechanical diffraction patterns produced by snakes and snake robots traversing periodic lattices [Snake SI Video], [Snake Robot SI Video].

lective confinement—yield emergent bound states that exhibit persistent translation, a form of mechanical ratcheting enhanced by noise and shape-change cycles. These systems exemplify how minimal actuation and shape deformation, when embedded in the right context, can produce rich emergent dynamics.

Critically, when such systems are augmented with *feedback mechanisms*—whether through embedded sensors, light-sensitive actuation, or real-time computation—they transition from passive responders to adaptive, task-oriented entities. Recent theoretical and

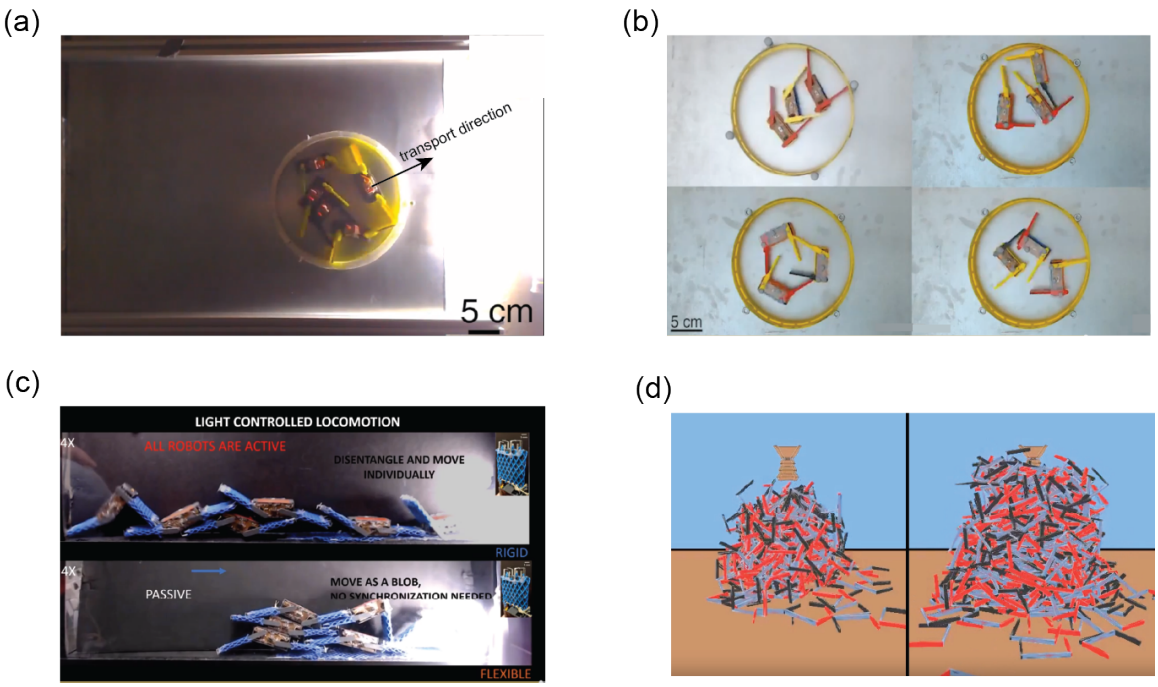

Figure 1.5: Robophysical investigations using smart-active-particles ("smarticles") to study emergent collective behaviors: (a) Directed transport and phototaxis in a swarm of five immotile smarticles confined within a rigid ring, enabling force transmission and structural cohesion [SI Video]. (b) Self-organized, low-rattling "dances" exhibited by a collective of three pinned smarticles [SI Video]. (c) Robotic mimicry of worm-blob entanglement and phototaxis by augmenting smarticle arms with meshy fabric and staple-shaped pins, with heterogeneous roles in the swarm enabling collective navigation [SI Video]. (d) Shape sculpting with dense ensembles of staple-shaped robots, demonstrating programmable self-assembly in 3D. [SI Video].

experimental efforts have begun to frame this capability in terms of *informational active matter* and *programmable collectives*, where control loops are embedded in the material body itself [90, 50, 25, 24]. These studies point toward a future where shape-changing active agents not only reveal fundamental insights into non-equilibrium physics but also inspire new paradigms in soft robotics, swarm intelligence, and adaptive materials.

Non-Reciprocity mediated Emergent phenomena

Non-reciprocal interactions—those that violate Newton's third law of motion by breaking action-reaction symmetry—play a foundational role in the emergence of collective behavior across biological, physical, and engineered systems. Unlike conservative forces that

derive from a potential, non-reciprocal interactions are inherently non-Hamiltonian and often arise in systems maintained far from equilibrium. As such, they provide a fertile playground for studying pattern formation, self-organization, and emergent dynamics [21, 20, 91].

In biological contexts, non-reciprocal interactions frequently govern developmental, ecological, and social dynamics. For example, in microbial communities, chemically mediated antagonism between competing species drives spontaneous spatial segregation, lane formation, and the emergence of interfacial instabilities [92, 93, 94].Similarly, cross-regulatory gene networks with promoter-inhibitor feedback loops guide cell differentiation processes, such as in zebrafish pigmentation patterns [95].

Beyond the microscale, human crowds also display signatures of non-reciprocity, where social forces and directional preferences can lead to non-reciprocal effective interactions among individuals. Models incorporating such interactions successfully reproduce dynamic features observed in pedestrian flows and evacuation scenarios [100, 101, 102, 103]. In animal behavior, leader-follower dynamics in flocking birds reveal asymmetries in influence that can be effectively modeled through non-reciprocal couplings [104, 105, 106].

At the mesoscopic scale, non-reciprocity often emerges when particles interact via a non-equilibrium medium. For instance, in dusty plasmas or colloidal suspensions, asymmetric hydrodynamic or phoretic interactions can yield direction-dependent forces [107, 108]. Catalytically active colloids provide a model system where non-reciprocity can be tuned via surface reactivity, enabling complex behaviors such as persistent pairing, waltzing, and formation of chiral or polar "active molecules" [52, 53, 109, 97]. A recent study demonstrates how non-reciprocal interactions between living cells can drive the self-assembly of a starfish-like chiral crystal, with non-reciprocity emerging as a key mechanism that breaks time-reversal symmetry and endows the structure with persistent rotational motion and chirality [96].

Recent developments in non-Hermitian physics have provided powerful mathematical

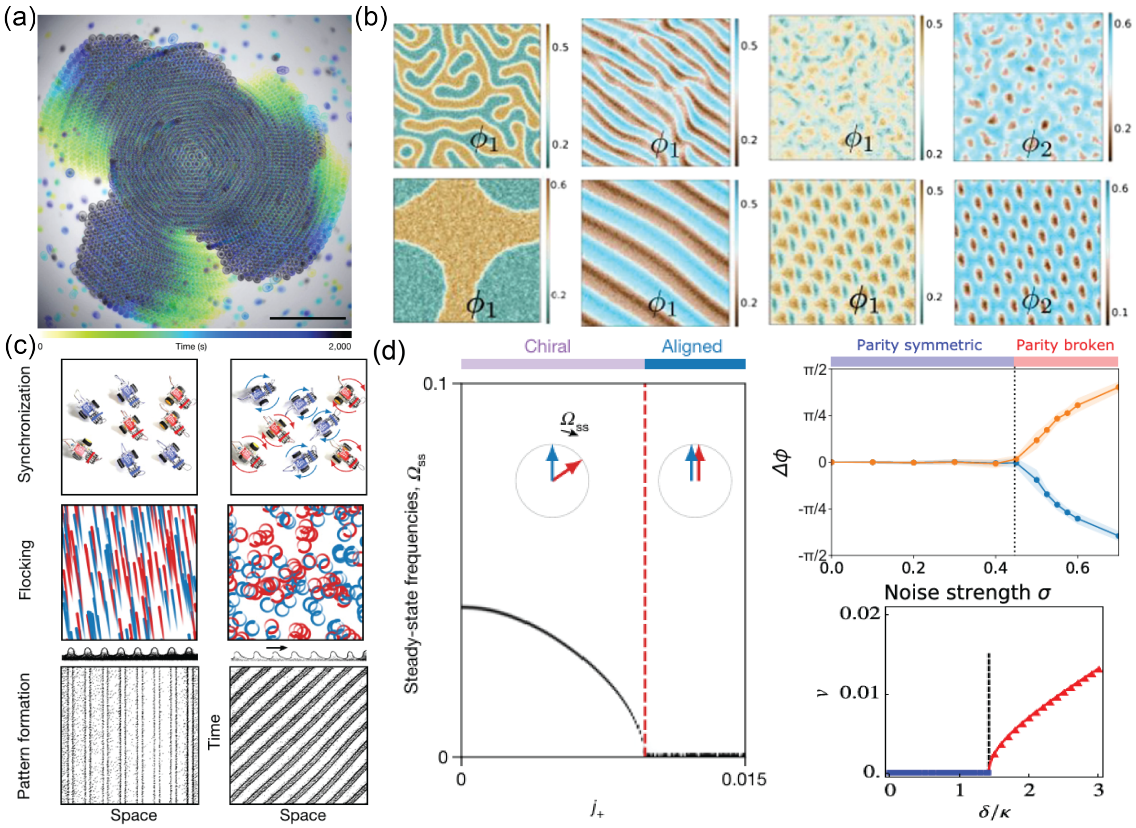

Figure 1.6: Some examples of emergent phenomena mediated by non-reciprocity in their interactions: (a) Emergence of chiral living crystals in starfish embryo undergoing development due to non-reciprocal interactions between autonomous multi-cellular components, adapted from [96]. (b) Scalar mixtures of the Non-reciprocal cahn hilliard model (NRCH) produce dynamic patterns such as lamellae and moving droplets as a function of the non-reciprocity parameter, taken from [97]. (c) Non-reciprocal phase transitions are a unifying theme across active collectives with antagonistic interactions among agents adapted from, [21]. (d) Different systems undergo a transition wrt the non-reciprocity parameter to produce symmetry broken time ordered states with mobility, taken from [21, 98, 99].

tools to describe and classify non-reciprocal systems. The breakdown of reciprocity leads to non-symmetric interaction matrices, whose spectral properties determine stability and pattern selection. In particular, exceptional points and the non-Hermitian skin effect have been linked to unidirectional wave propagation and localization phenomena [110, 21]. A follow up study shows that non-reciprocal interactions can give rise to time crystalline order and a spin-glass-like state through geometrical frustration, revealing new organizing principles in non-equilibrium many-body systems [98]. Studies have also showed that engineered

nonreciprocal interactions in acoustic and elastic media enable directional wave control and signal isolation through symmetry breaking and time-variant modulations [111].

These ideas have found experimental realization in mechanical and robotic metamaterials. For instance, lattices of coupled robotic units with programmed phase delays exhibit unidirectional soliton and anti-soliton propagation, mimicking topological insulators but in a dynamic, out-of-equilibrium setting [112, 113]. Similar principles have been used to engineer mechanical diodes and circulators, enabling novel forms of energy transport and signal routing.

Non-reciprocal interactions thus offer a unifying perspective on the origin of complex dynamics in diverse systems. As experimental techniques and synthetic platforms advance, the ability to engineer and tune such interactions will pave the way for new modes of control and functionality in active matter. From living tissues and swarming robots to self-organizing colloids and programmable metamaterials, non-reciprocity provides a fertile ground for exploring the rich physics of far-from-equilibrium systems.

Organization of this Thesis

This dissertation explores how shape-changing robots interact via collisions to exhibit emergent behaviors ranging from self-organized dances to pairwise binding and transport to many-body organization. The thesis is organized as follows:

- **Chapter 2: Demonstration of Low-Rattling States in Pinned Smarticle Collectives**

  Demonstrates how environmental constraints and synchronized actuation guide a confined three-robot collective into low-rattling, dynamically stable states, adapted from sections of a publication [23],

- **Chapter 3: Emergent Binding in Shape-Changing Dyads**

  Reveals how pairs of robots form mobile gliders via repulsive, yet coordinated, colli-

sions enabled by concavity and tactile feedback, adapted from a manuscript in prep. [114].

- **Chapter 4: Symmetry Breaking and Transport in Gliding Dyads**

  Shows how breakdown of exchange symmetry due to non-reciprocal gaits induce robust, chiral locomotion in dyads through non-commutative shape changes, adapated from a manuscript in prep. [115].

- **Chapter 5: Many-Body Dynamics and Long-Range Order**

  Phenomenology of dense robot ensembles self-assembling into chains and loops through gait mediated collisional binding and Velcro based adhesion, extending dyad-scale principles.

- **Chapter 6: Future Directions**

  Outlines how these results inform future work in robotic swarms and active matter studies with programmable collectives of these robots.

CHAPTER 2
DEMONSTRATION OF LOW-RATTLING STATES IN PINNED SMARTICLE COLLECTIVES

2.1 Introduction

Smarticle swarms offer a rich experimental platform to study emergent collective behavior in active matter systems with many degrees of freedom. Each smarticle is a simple robot composed of a central body and two rotating arms, yet when placed in dense environments, their motion becomes highly complex. This complexity arises from frequent collisional interactions and Coulomb friction damping between smarticles and with their environment, leading to strongly nonlinear, disordered, and noisy dynamics. Despite this apparent randomness, specific drive protocols can guide the system into ordered, low-rattling states—configurations where the force fluctuations are minimized despite ongoing actuation. To ensure consistency across trials, these drive protocols were carefully entrained to a fixed frequency using an external speaker, which phase-locked the actuation of all robots and minimized noise due to phase-slipping between the motors of individual smarticles. In this chapter, we demonstrate how tailored driving patterns and energy dissipation can reduce rattling and induce robust spatio-temporal self-organization in a system of three smarticles confined within a rigid ring.

2.1.1 Emergence of Self-Organized States in 3-Smarticle Systems

Rattling in smarticle collectives arises from the interplay between internal actuation and external constraints. Each drive protocol can thus be interpreted as imposing a distinct "rattling landscape" over the configuration space. Analogous to energy landscapes in equilib-

[0]This chapter is adapted from sections of the manuscript *Low rattling: A predictive principle for self-organization in active collectives*. DOI: https://doi.org/10.1126/science.abc6182

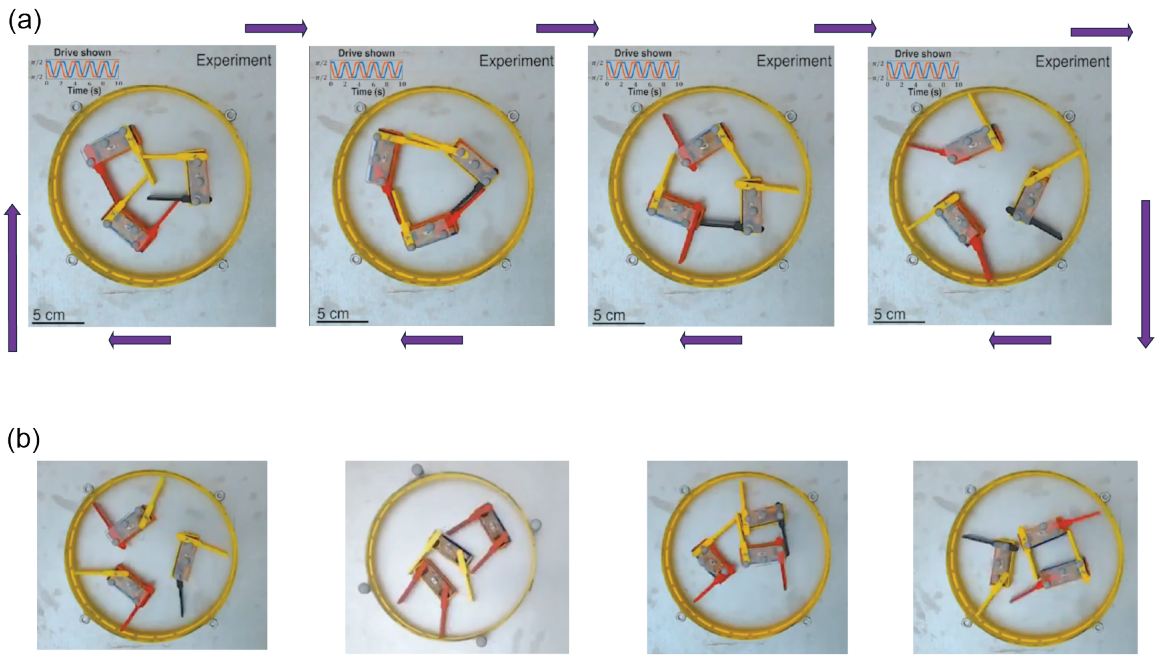

Figure 2.1: Different self-organized dances exhibited by the three robot collective: (a) Time snaps of the different robot postures exhibited by the rotationally symmetric configuration during it's actuation cycle. (b) Four distinct low rattling states, visited most frequently by the robot collective.

rium statistical mechanics, low-rattling configurations are favored similarly to low-energy states in a Boltzmann distribution. For example, under the drive protocol 3 depicted in Figure 2.3—where all three smarticles execute the same time-periodic motion—the resulting rattling landscape is visualized. The corresponding steady-state spatial distribution exhibits localization in regions of minimal rattling, highlighting a strong correlation between rattling and configurational occupancy. This relationship is quantitatively validated by plotting steady-state density as a function of the local rattling amplitude.

2.1.2 Drive-Specific Emergence of Low-Rattling States

To systematically investigate how different drive protocols shape the rattling landscape and guide the emergence of organized states, we implemented four distinct actuation patterns Fig. Figure 2.3.

- **Drive 1**: Each smarticle actuates both arms independently and randomly between

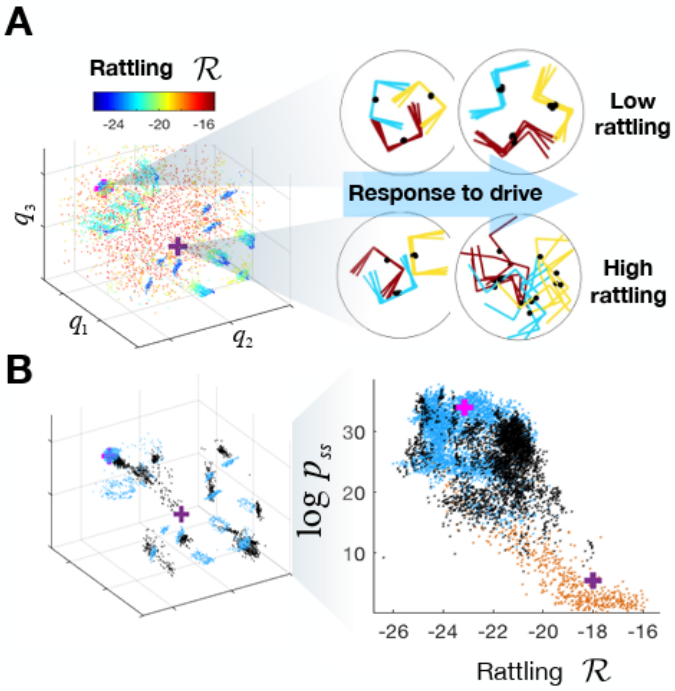

Figure 2.2: Rattling landscape predicts steady-state configurations: (A) The rattling landscape corresponding to the drive 3 of Figure 2.3 is shown, with two representative configurations—one low-rattling (pink cross) and one high-rattling (purple cross)—highlighted. The short-time responses of five nearby configurations are shown to contrast stability under drive. (B) The steady-state distribution concentrates in low-rattling regions, shown both in configuration space and by plotting steady-state density as a function of rattling. Red points represent uniformly sampled configurations, while blue and black show data drawn from the steady-state—black indicating experimental data. Together, these reveal how low-rattling regions dominate the long-time dynamics.

$\pm\pi/2$. This protocol is memoryless and shown in Fig. Figure 2.3, left most column.

- **Drive 2**: The same random arm motions are synchronized across all three smarticles, introducing coordination without temporal determinism.

- **Drive 3**: The synchronized motion is now temporally deterministic and periodic. This protocol, used in the third column of Fig. Figure 2.3 and represents a fully coherent collective drive.

- **Drive A**: Each smarticle follows a distinct, deterministic motion sequence. Although

all motions are periodic for each robot, they differ across smarticles, as shown in the right-most column of Fig. Figure 2.3.

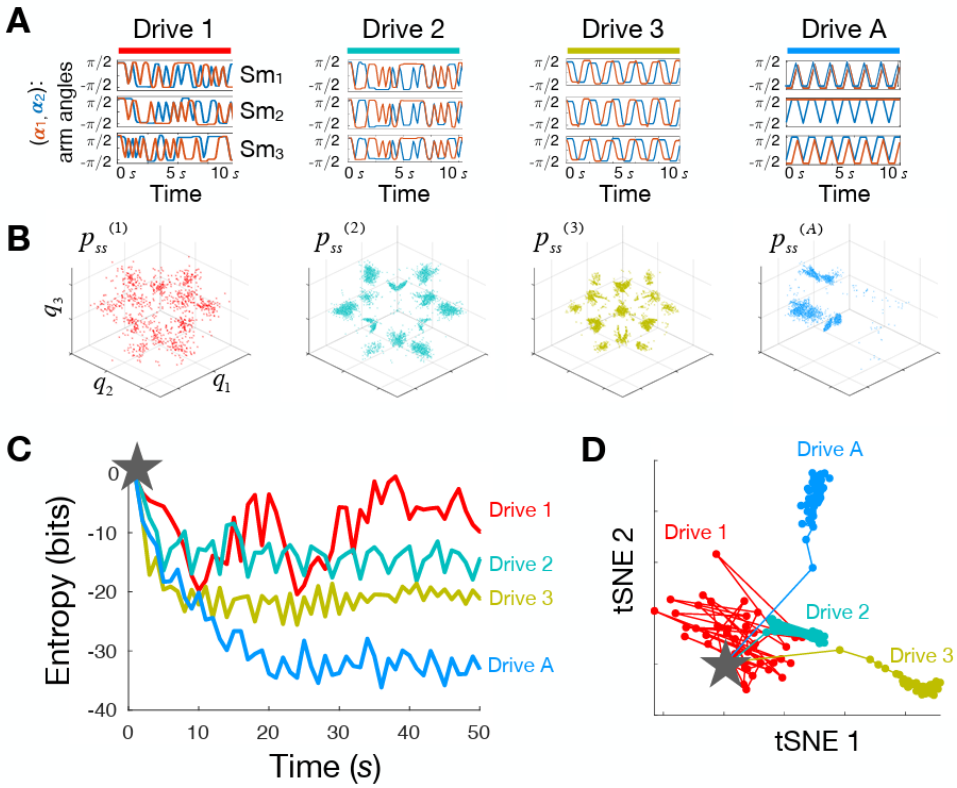

Figure 2.3: Role of drive in shaping emergent self-organization: (A)Four distinct smarticle arm-drive patterns are shown, ordered by increasing temporal and spatial structure—from random and uncoordinated to deterministic and individual-specific. (B) Each drive yields a unique steady-state spatial distribution in configuration space, with more structured drives resulting in increasingly localized states. (C) The temporal evolution of spatial entropy reveals how structured drives progressively constrain the system into lower-rattling regions, with entropy decreasing more steeply for drives with higher predictive content. (D) A t-SNE projection of the distributions over time illustrates how each drive sculpts the system's trajectory from an initially uniform state toward a characteristic steady-state shape, with divergence increasing in accordance with drive specificity.

These drives can be ordered by their *predictive information*—the extent to which past knowledge of the drive aids in predicting future motion. Drive 1 contains no temporal correlations, making future predictions impossible beyond the constraint of angular bounds. Drive 2 introduces permutation symmetry, revealing that all smarticles perform identical actions at each moment. Drive 3 adds temporal structure through periodicity. Drive

A, being both temporally structured and spatially nonuniform, requires encoding the full identity-specific motion sequence of each smarticle to anticipate future behavior.

2.1.3 Destroying self-organization with friction

The emergence of self-organized states in smarticle collectives depends critically on the system operating in a sufficiently overdamped regime. In this regime, collisions between smarticles and with the boundary do not lead to persistent ballistic motion or scattering, but instead result in rapid momentum loss and confinement to a bounded region of configuration space. This overdamped behavior is governed by the velocity decay time τ, which characterizes how quickly kinetic energy dissipates after actuation. A small τ ensures that collisions are effectively inelastic and that the drive-induced motion remains localized, enabling the formation of low-rattling steady states.Figure 2.4 explores how varying τ influences the steady-state distribution in simulations under Drive 3.

To experimentally modulate the friction between the smarticles and the stage, we reduced contact friction by spreading a loose monolayer of small plastic beads across the surface. This layer effectively allowed the smarticles to move with significantly lower resistance, as they were able to roll over the beads rather than slide directly against the stage. Importantly, the beads were chosen to be light and non-reactive, ensuring they did not exert significant back-forces on the smarticles and served purely to reduce friction. This setup enabled us to access a low-friction regime and explore how reduced damping influenced the collective dynamics. For comparison, we also conducted simulations that interpolated between high- and low-friction regimes by continuously tuning the damping coefficient Figure 2.4.

It has also been shown that diverse classes of dynamical systems tend to exhibit intermittent transitions between metastable macroscopic behaviors, with long-lived dynamical patterns often corresponding to low-fluctuation—or low-rattling—states where the system's long-term dynamics tend to reside [116]. Examples studied include a simulated

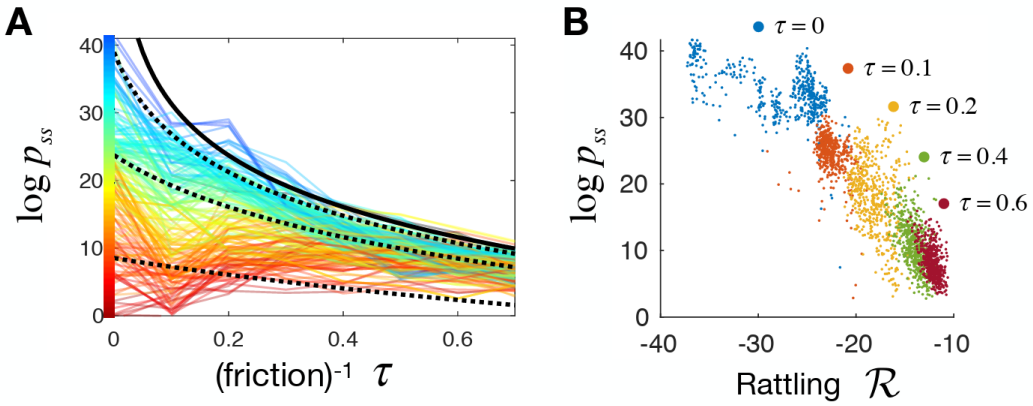

Figure 2.4: Rattling landscape can be melted by increasing inertia in the system, via friction reduction: Panel (A) shows the steady-state probabilities $\log P_{ss}$ across 200 system configurations subjected to drive A, with friction progressively reduced via increasing values of the velocity decay timescale τ (inversely proportional to friction). Each line corresponds to a configuration, colored by its probability in the strongly overdamped limit ($\tau \to 0$). The solid black line represents the theoretical decay for low-rattling configurations, while the dotted lines denote model fits using a decay constant $\gamma = 3.1$. Panel (B) confirms that the relationship between probability and rattling $\mathcal{R}$, given by $\log P_{ss} \sim -\mathcal{R}$, holds consistently across values of τ. Together, the panels demonstrate that behaviors in the high-friction limit are predictive of dynamics at lower friction levels.

metronome array on an oscillating platform, the Lorenz attractor, and the motion of a particle in a bistable potential landscape influenced by noise. In each case, varying a control parameter—such as the distribution of oscillator detunings in the metronome system, the parameter ρ in the Lorenz system, or the noise distribution in the particle model—induces a transition from a relatively disordered regime to an ordered one, often mediated by a regime rich in oscillatory dynamics. Notably, all these systems exhibit a "sweet spot" in parameter space characterized by persistent, coherent oscillations and intermittent switching, suggesting a unifying theme: systems with sufficiently many degrees of freedom, and whose dynamics are approximately stochastic, can generically self-organize into low-rattling states under appropriate conditions.

Building on these studies that use rattling to characterize the stability of configurations in driven systems, recently it was cast as a general local-to-global principle for nonequi-

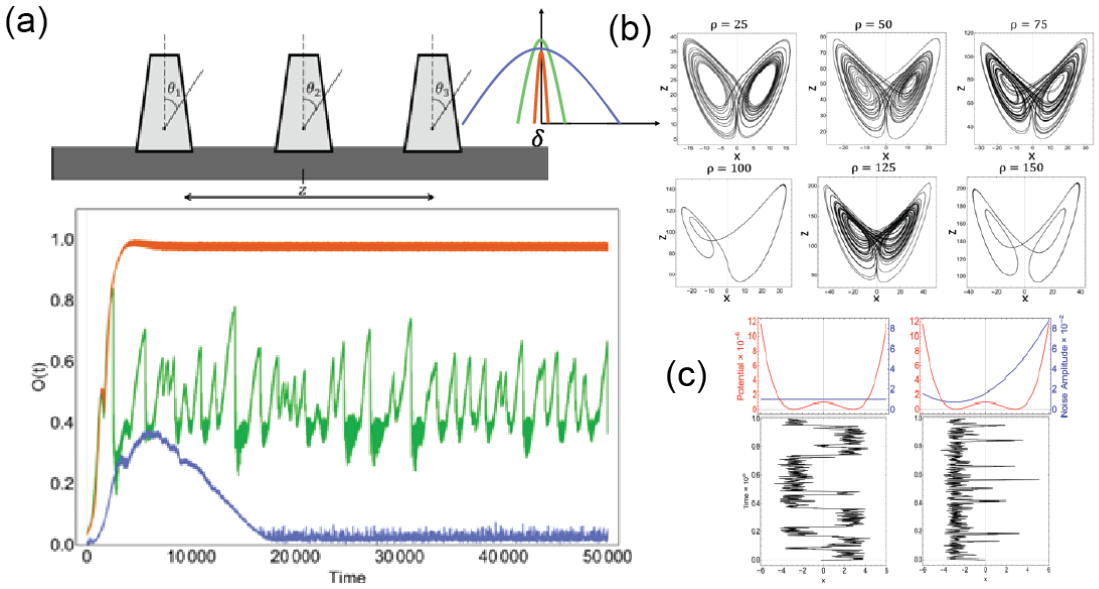

Figure 2.5: Deterministic and stochastic dynamical systems exhibit low rattling behaviors, adapted from [116]: (a) A simulated array of metronomes interacting via an oscillatory platform, with varying distributions of detuning exhibits a regime of intermittent oscillatory dynamics, where clusters of metronomes locally exhibit synchronized activity and drift in and out of phase. The time series for the order parameter reveals this. (b) Modified lorenz attractor with the parameter ρ allowed to vary with x. (c) 1D motion in a bistable potential well with varying intensities of noise indicating hopping and localization between wells.

librium steady states, showing that rattling—a local property—can predict the global organization of a wide range of nonequilibrium systems even in the absence of an energy-like potential [117].

CHAPTER 3
COLLISIONAL BINDING AND TRANSPORT OF SHAPE-CHANGING ROBOT PAIRS

3.1 Summary

We report in experiment and simulation the spontaneous formation of dynamically bound pairs of shape changing robots undergoing locally repulsive collisions. Borrowing terminology from Conway's simulated Game of Life, these physical 'gliders' robustly emerge from an ensemble of individually undulating three-link two-motor robots and can remain bound for hundreds of undulations and travel for multiple robot dimensions. Gliders occur in two distinct binding symmetries and form over a wide range of angular oscillation extent. This parameter sets the maximal concavity which influences formation probability and translation characteristics. Analysis of dynamics in simulation reveals the mechanism of effective dynamical attraction – a result of the emergent interplay of appropriately oriented and timed repulsive interactions. Tactile sensing stabilizes the short-lived conformation via concavity modulation.

3.2 Introduction

Collisional dynamics, a cornerstone of physics, govern interactions across scales, from particle collisions revealing fundamental forces to the scattering of electrons in crystals. While classical inelastic collisions, which do not conserve energy, can lead to emergent phenomena like clustering [1, 2], inelastic collapse [29, 30, 38, 118], jamming, and transitions between fluid- and solid-like states [39, 3], active systems — comprising agents driven by internal energy and dissipative interactions — display even richer dynamics [58].

[0]This chapter is adapted from sections of a manuscript in preparation.

These systems challenge traditional conservation laws as momentum and energy can be redistributed through environmental interactions [119, 6], leading to non-trivial behaviors such as wall-accumulation in bacteria [120] and spontaneous reorientation in cockroaches [63]. Other remarkable phenomena include the emergence of patterns and collective order driven by repulsive interactions, observed in systems such as molecular motors [60, 121, 122], and shaken grains [4, 5, 7]

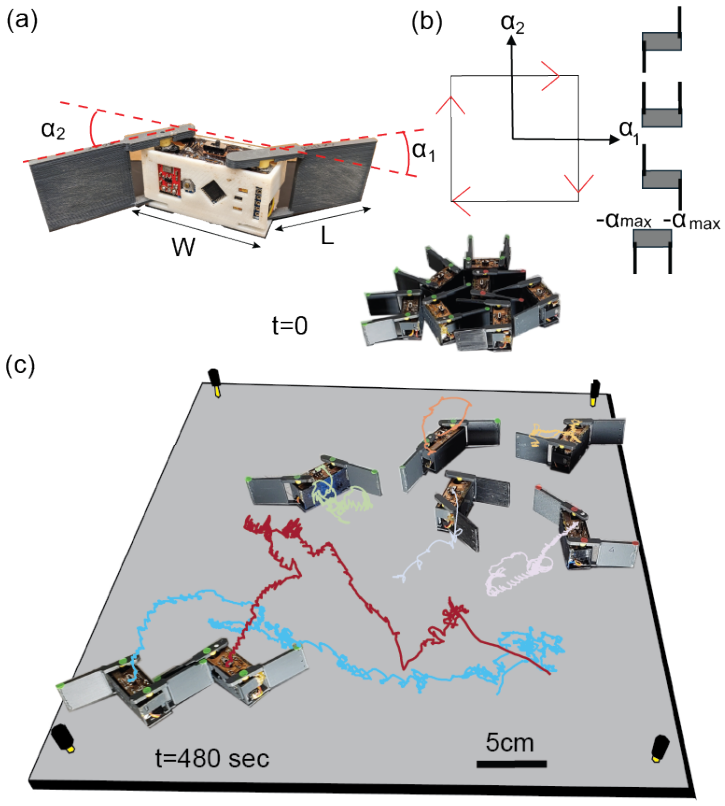

Figure 3.1: Emergence of a glider from an unconfined collective of 7 smarticles synchronized to start at the same initial phase: (a) Configuration of a smart active particle (smarticle), parametrized by arm angles α_1 and α_2 relative to the body. The smarticle rests on its central body, with arms having slight ground clearance. (b) Square gait configurations of a smarticle in the shape space defined by α_1, α_2 with amplitude α_{max}. Red arrows indicate the direction of gait traversal. (c) The emergence of a locomoting glider from a collective of seven smarticles, visualized through body center trajectories, with the final path traced at $t = 480$ seconds. Top: compressed collective at $t = 0$.

Active extended objects capable of self-deformation using internal energy exhibit dis-

tinctive locomotion and mechanical properties [70, 9, 10, 71, 72, 73, 74, 75], distinguishing them from regular active agents. While traditional active agents reveal compelling behaviors in large numbers, shape-changing objects demonstrate unique emergent phenomena such as mechanical diffraction [12, 76, 13], emergent locomotion [112], and lattice traversal [77], even with fewer agents due to their high degrees of freedom. Collectively they exhibit phenomena like gait synchronization in nematode clusters and coordinated movement in undulatory robots [83, 84, 85, 86, 87], and form complex structures such as worm blobs and ant bridges [14, 64, 88]. Purcell-inspired three-link robots, including *smarticles* (smart active particles) [15, 11, 22, 89], serve as a versatile platform for studying these systems. Though isolated smarticles exhibit limited motility, they demonstrate nontrivial dynamics through collisions, forming dynamically stable bound states that translate persistently despite noise and complex internal dynamics. By coupling shape-deformation with feedback mechanisms, these systems offer insights into emergent task-oriented behaviors [24, 50, 25, 90].

Here, we study unconfined smarticle collections, where we observe that the individally immotile robots can emergently and dynamically bind to form physical "gliders." These gliders ballistically travel several body lengths through repulsive collisional interactions. Experimentally validated simulations provide insights into glider formation and stability; these principles are applied to stabilize an otherwise unstable gliding mode through a contact sensor-based feedback strategy.

3.3 Experimental Apparatus.

The smarticles, each with a mass of m = 34.8 $\pm$ 0.6g, are studied under open-loop control. They consist of three links: two side arms, each having a length of L = 5.0 cm and a thickness of 0.3 cm, and a central link (body) with a width of W = 5.4 cm and a depth of D = 2.2 cm Figure 3.1(a). 7 robots were placed on a $60 \times 60\,\mathrm{cm}^2$ aluminum plate, leveled to $\leq 0.1^\circ$. The gait – the sequence of shape-changing motions – of each smarticle

(depicted in Figure 3.1(b)) was inspired by the dynamics of Purcell's three-link swimmer [15, 123, 75]. The periodic shape-changing motions are achieved by actuating the revolute joints connecting the central link to the side arms using a programmable servo motor, with a gait period of 1.6 seconds. The side arms were rotated at the maximal motor speed until reaching the target arm rotation amplitude angle. The ground clearance of the arms prevents the inertial impulse of the actuated arms from being transmitted to the central body, which results in negligible motion of the central link. In addition, any motion induced by arm actuation is limited by the fiction between the central link and the underlying surface, contributing 0.0015 W (75 μm) per cycle.

The friction between the smarticle and the underlying surface limited the motion induced by the arm rotations to approximately 0.0015 W (body lengths), equivalent to 0.0075 cm per cycle. Therefore, individual smarticles do not move significant distances on their own. To enable contact feedback sensing, we designed a scaled-up version with a total mass of m = 175 $\pm$ 0.5g, arm width and thickness of 6.0 cm and 0.7 cm, respectively, and body width and depth of 6.5 cm and 3.5 cm, respectively. We mounted force resistive sensors on all four arm faces to detect contacts based on impact thresholds (Figure 3.8(a), Fig. S6).

Observation of Gliders. A collection of seven smarticles was initialized in a densely packed configuration, with all robots beginning their shape-changing motions simultaneously and in phase, triggered by an audio frequency of 1000 Hz, as shown in Figure 3.1(c). We expected the smarticles to push each other away through collisions, causing them to expand into a relaxed state, where no robots were in contact with each other. However, in 64% of trials (97 out of 151), we observed that a pair of robots moved together for ≥ 100 gait periods, traveling an average distance of $2.9 \pm 0.2\ W$, as shown in Figure 3.1(c). The formation, stability, and locomotion of these *gliders* were remarkable, given that the robots interacted locally repulsive collisions. The discrete and highly nonlinear collisions made theoretical analysis challenging. To systematically study the gliders, we developed

a simulation based on the open-source physics engine Chrono and calibrated it against experiments (see Fig. A1). In the following sections, we discuss the anatomy, binding mechanism, and stability of the gliding dyads. To test our understanding of the stabilized binding and gliding, we conclude by demonstration how a simple control strategy extends the lifetime of the short-lived glider.

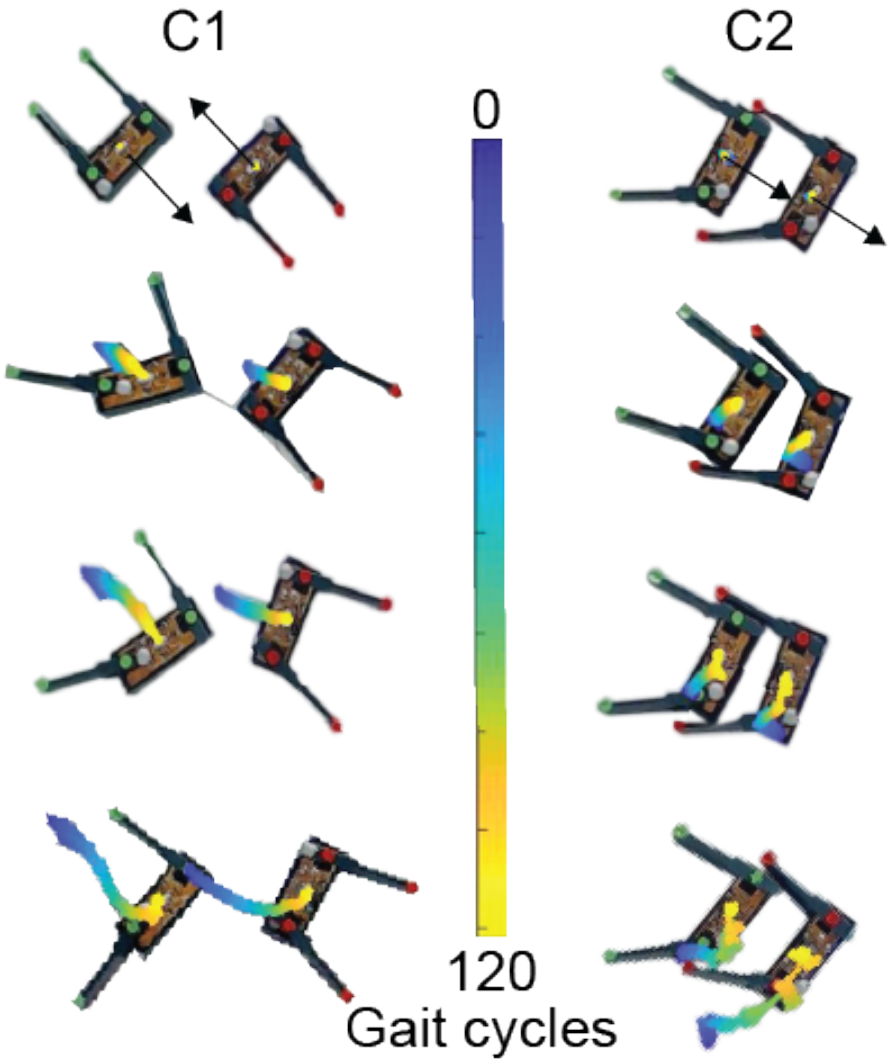

Figure 3.2: Strobed snapshots of the asymmetric emergent dyad configurations ($C1$ - almost anti-aligned, $C2$ - almost aligned), gliding as a bound entity over time. Arrows represent the body normal vectors.

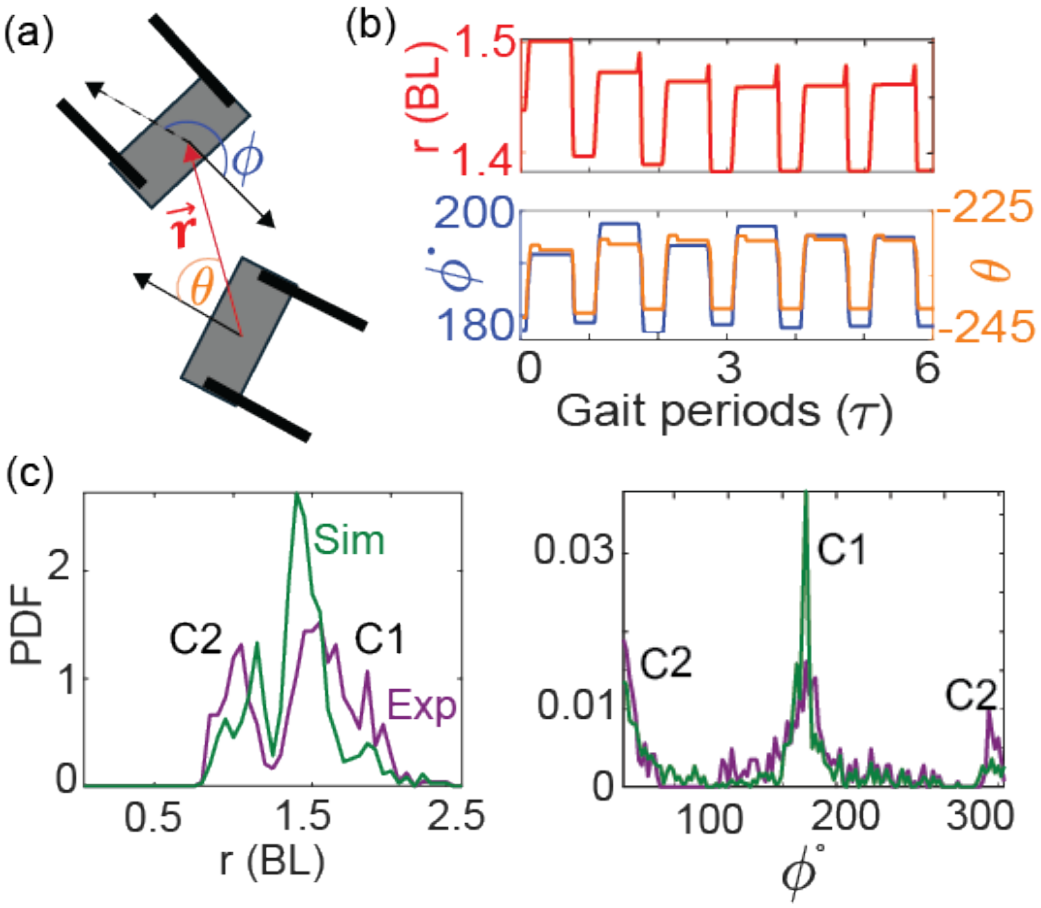

Figure 3.3: Distributions of relative coordinates reveal two peaks highlighting the two emergent modes: (a) A gliding dyad is defined by a pair of smarticles with relative position $(\vec{r}, \theta)$ in polar coordinates and relative body orientation (ϕ) as the difference between their normal vectors. (b) Temporal evolution of r in body lengths and the angular coordinates θ, ϕ over six periods for a gliding dyad. (c) Distributions of r and ϕ for all emergent dyads in simulations and experiments, showing two peaks corresponding to modes C1 and C2.

3.4 Glider Configurations.

Experiments and simulations (N = 151 trials) revealed that the gliders adopted two distinct configurations. These configurations exhibit a slight deviation from perfect anti-alignment and alignment, similar to chiral phases observed during non-reciprocal phase transitions [21] in various non-equilibrium systems. We refer to them as: (i) "$C1$," where the two smarticles are nearly anti-aligned, with their absolute orientations differing by approximately 180 degrees, and (ii) "$C2$," where the two smarticles are oriented in approximately

the same direction. Snapshots of the glider configurations are shown in Figure 3.2. To characterize these distinct configurations, we measured their inter-smarticle distance r, the polar angle θ and their relative orientation ϕ, as defined in Figure 3.3(a). The time evolution of the relative coordinates r, θ, and ϕ over 6 periods for a glider trajectory (Figure 3.3(b)) demonstrates consistent behavior across many periods, characteristic of a limit cycle [124]. The distribution of the relative coordinates of the gliders observed in experiments and simulation shows distinct peaks in their histograms (Figure 3.3(c)(i-ii)), corresponding to the glider configurations $C1$ and $C2$. Furthermore, the two glider configurations exhibited distinct lifetimes (Figure 3.4), with $C1$ gliders persisting longer than $C2$ gliders, as shown by the long tail in the $C1$ lifetime distribution. For trials lasting 300 gait periods, some $C1$ gliders remained bound and locomoting until stopped. The phase drift in the gaits of glider-forming smarticle pairs during experiments caused slight variations in the distribution of r & ϕ, compared to simulations (Figure 3.3(c)(i-ii)).

3.5 Glider Lifetimes.

The C1 glider, or nearly antisymmetric mode, remained sterically stable due to sustained periodic attraction from the hooking interaction between its arms (Figure 3.7(a)(i)). In contrast, the C2 glider disintegrated under cyclic compression interactions (Figure 3.7(a)(ii)). Lifetimes of emergent gliders exceeding 30 periods -— the time for the expanding cloud to reach steady state -— plotted against relative orientation ϕ show that C1 gliders, clustered around $\phi = 180°$, persist throughout the trial (Figure 3.4(a)). In contrast, C2 gliders, characterized by symmetric clusters at $\phi = 0, 360°$, break apart faster, lasting only 70–100 cycles. To highlight these effects, we plotted lifetimes on a semi-log scale (Figure 3.4(b)), where the sharp peak at 300 indicates that the surviving gliders at the end of the trial remained in the C1 configuration.

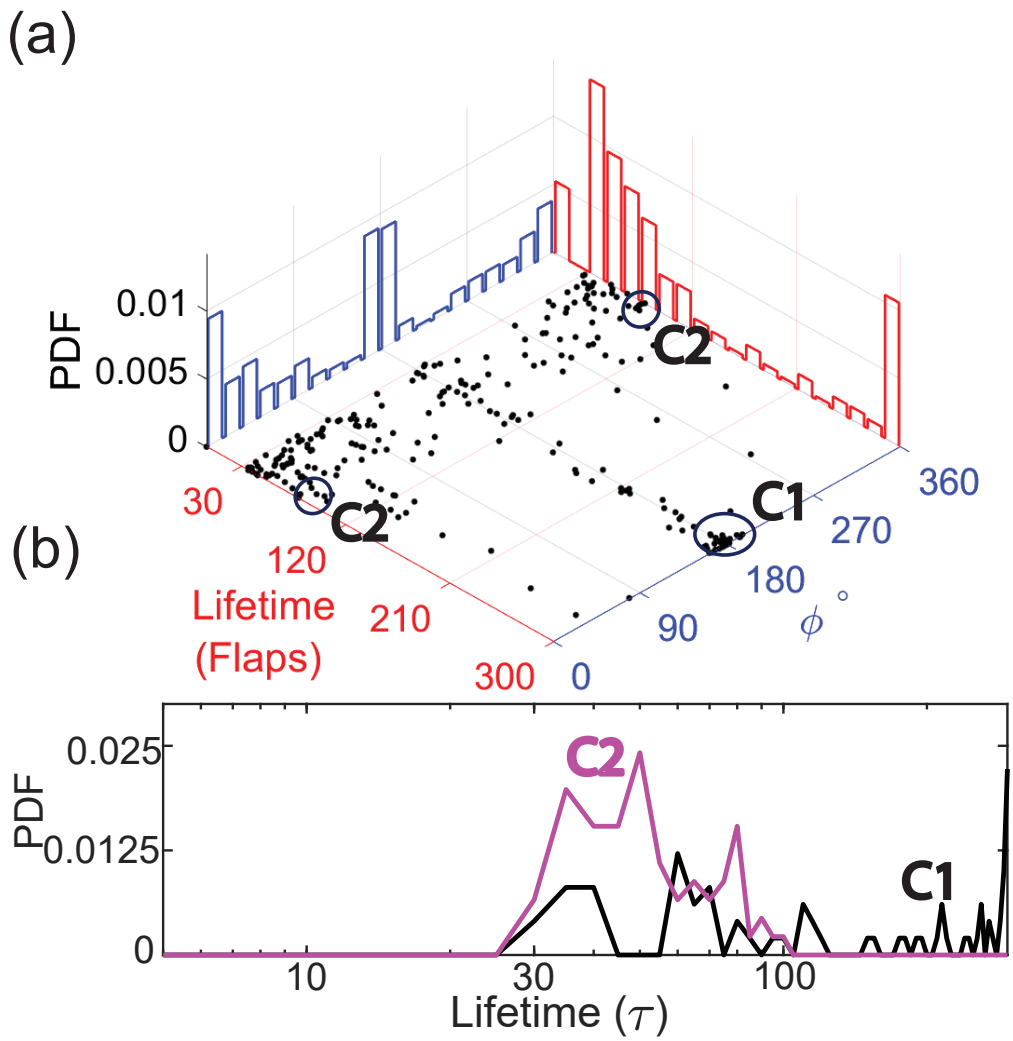

Figure 3.4: Distributions of glider lifetimes with ϕ: (a) Lifetime of emergent dyads vs. relative angle ϕ, showing the lifetimes of the two configurations. The scatter plot shows that the C1 configuration is more stable dynamically bound mode, with lifetimes spanning the entire trial. Histograms display the individual distributions for lifetime and relative orientation ϕ. (b) Lifetimes of the two configurations on a semi-log scale, illustrating the presence of long-lived C1 gliders, denoted by the peak around 300 flaps.

3.6 Glider Robustness and Transport.

To test the robustness of bound-pair states and their subsequent locomotion, we systematically varied the arm amplitude (maximum rotation angle α_{max}) while keeping the rotational speed constant. We then studied the persistence of bound pairs for shapes with different concavities [125] We performed experiments by fixing one smarticle and initializing the

other at 21 points on a polar grid of radius 1 BL, across a range of α_{max}. We observed different types of bound states: some in which the smarticles maintained periodic contact over multiple cycles, and others where they disengaged for a few cycles before re-establishing contact.

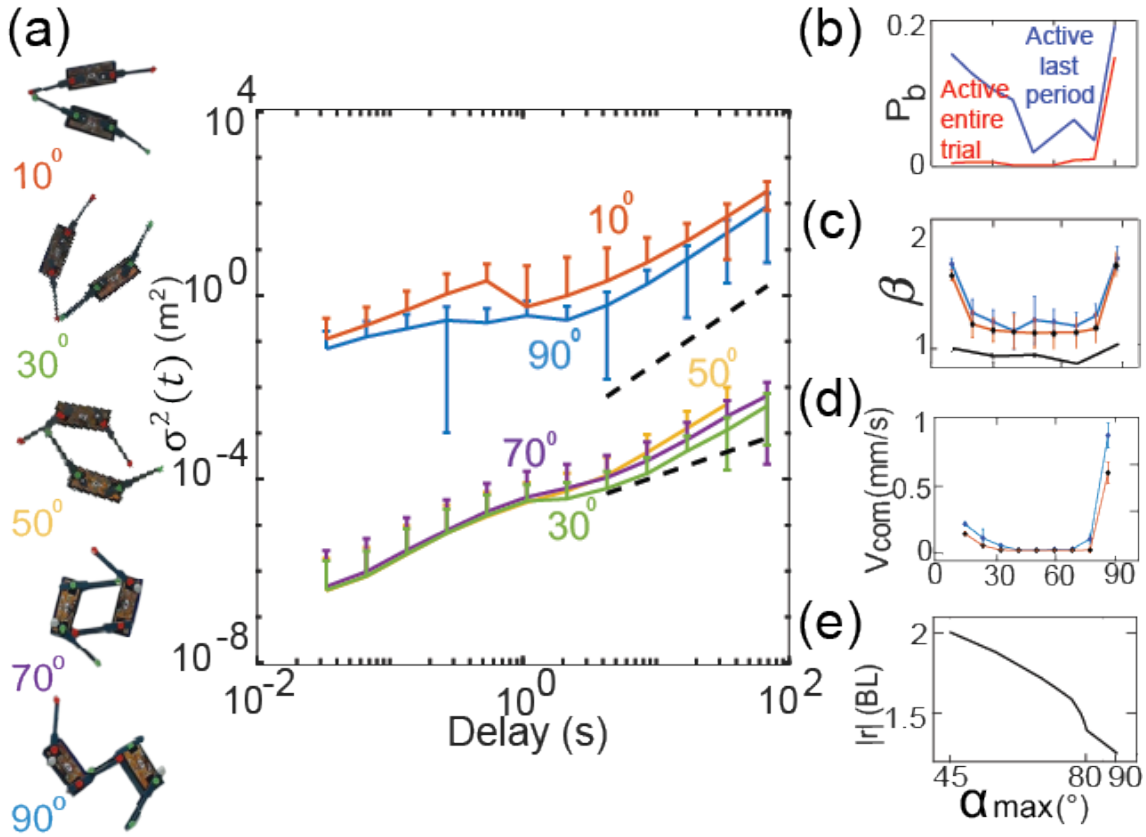

Figure 3.5: Transport properties of gliders with gaits of different concavities: (a) MSD $\langle\sigma^2(t)\rangle$ vs. time delay for five arm amplitudes, with snapshots of the corresponding bound pairs. (b) Binding probability P_b vs. arm amplitude for random initial conditions; blue: pairs active at trial end, red: pairs active throughout the trial. (c) MSD exponent β vs. $\alpha_{\max}$ for bound pairs; blue (experiment) and orange (simulation) curves with standard deviation bars. Black: exponent for time-symmetric gait in simulations. (d) Bound pair center-of-mass speed V_{com} vs. $\alpha_{\max}$. (e) Steady-state separation r vs. $\alpha_{\max} > 45°$ from simulations of initially bound smarticles.

The mean-square displacement (MSD) vs. time for glider trajectories surviving more than 30 cycles is shown in Figure 3.5(a) for five different arm amplitudes. The bound pairs for $90°$ and $10°$ move nearly ballistically, with $\langle\sigma^2(t)\rangle \propto t^\beta$ (where MSD $\langle\sigma^2(t)\rangle = \langle\vec{x}^2(t)\rangle - \langle\vec{x}(t)\rangle^2$ and exponent $\beta \approx 1.8$), For intermediate arm amplitudes, the motion is

almost diffusive. We observed that gliders in experiments exhibit a higher β and center-of-mass speed V_{com} than those in simulations, as shown in Figure 3.5. We posit that experimental noise from the motors, collisions, and friction with the floor enhances the transport of bound pairs with intermediate arm amplitudes ($40°-60°$), but the pairs bind and unbind frequently. The lack of stability for intermediate α_{max} correlates with a decrease in binding probability (Figure 3.5(b)).

Bound pair speed and transport decreased sharply as α_{max} decreased from $90°$, but surprisingly increased again in the low-amplitude regime (see $10° - 20°$ range in Figure 3.5(c-d)). We attribute this anomaly to inertial effects, which enhance the drift of a single smarticle, as shown in Fig. A2. Since the smarticle arms were driven at a constant motor speed, at low rotation angles, the arm rotation time matched the overlap time between the motions of two arms, as shown in Fig. A3. This significantly increased the motility of individual smarticles. As a result, dyad pairs that remained bound at low α_{max} also showed improved gliding speed, as shown in Figure 3.5(c-d). To probe how arm amplitude affects glider locomotion, we simulated smarticles pairs in a bound formation, performing gaits with varying α_{max} values greater than $45°$. A clear trend appears, where r monotonically decreases as α_{max} increases (. Figure 3.5(e)), with a rapid drop in r around $85°$. Coincidentally, this is also roughly the amplitude at which the β and V_{com} increase sharply (Figure 3.5(c-d)). Simulations revealed that for $\alpha_{max} \leq 85°$, the smarticles interact with only one arm, while above this threshold, they experience an additional collision with the other arm. The additional collision brings the smarticles closer together, leading to a third collision between an arm and the central link. Since super-diffusive transport becomes effective for $\alpha_{max} \geq 85°$, we attribute most of the locomotion to these additional collisions.

3.7 Binding Mechanism.

Repulsive collisions between two convex-shaped bodies typically cause them to repel. However, smarticle pairs can remain bound as they develop concave shapes during their shape-changing motions. This enables the net contact impulse during a collision between the two robots to produce an attractive effect, causing them to move together at least once during the gait. Friction between the smarticle's base and the underlying surface prevents coasting, while periodic attractive contact forces during collisions keep them bound over multiple gait periods. However, under certain conditions —- dependent on the smarticle pairs' relative positions, orientations, and gait phase -— the pairs can harness attractive collisions that keep them bound. To identify the binding conditions, we simulated collisions by fixing one robot (gray) and varying the absolute heading of the second robot across a constant-radius polar grid ($r = 1.3$ BL, θ, ϕ) for two gait phases, $p = 0, 0.25$, as shown in Figure 3.6(a). Once initialized at the same phase, we tracked the lifetimes of bound pairs over 75 gait periods and partitioned the relative configuration space into regions of attraction (pink) and repulsion (blue), based on the outcome of each robot pair. The attracted configurations correspond to initial conditions that formed stable glider and survived the entire trial. These configurations converge to the periodic deformation pattern characteristic of the attractor (Figure 3.3(b)) within a few periods. Moreover, robot pairs' binding status can be determined from their configuration after the first gait period, where their relative orientations dictate whether the subsequent collision results in attraction or repulsion.

The results indicate that the formation of a bound pair between two smarticles is governed by a non-reciprocal binding affinity, which depends on their polar angle θ and relative headings ϕ. Robot pairs with initial configurations in the first and fourth quadrants (with respect to θ) of the interaction range are likely to form bound pairs (pink sectors) when their normal vectors are antiparallel. Conversely, robot pairs with parallel normal vectors

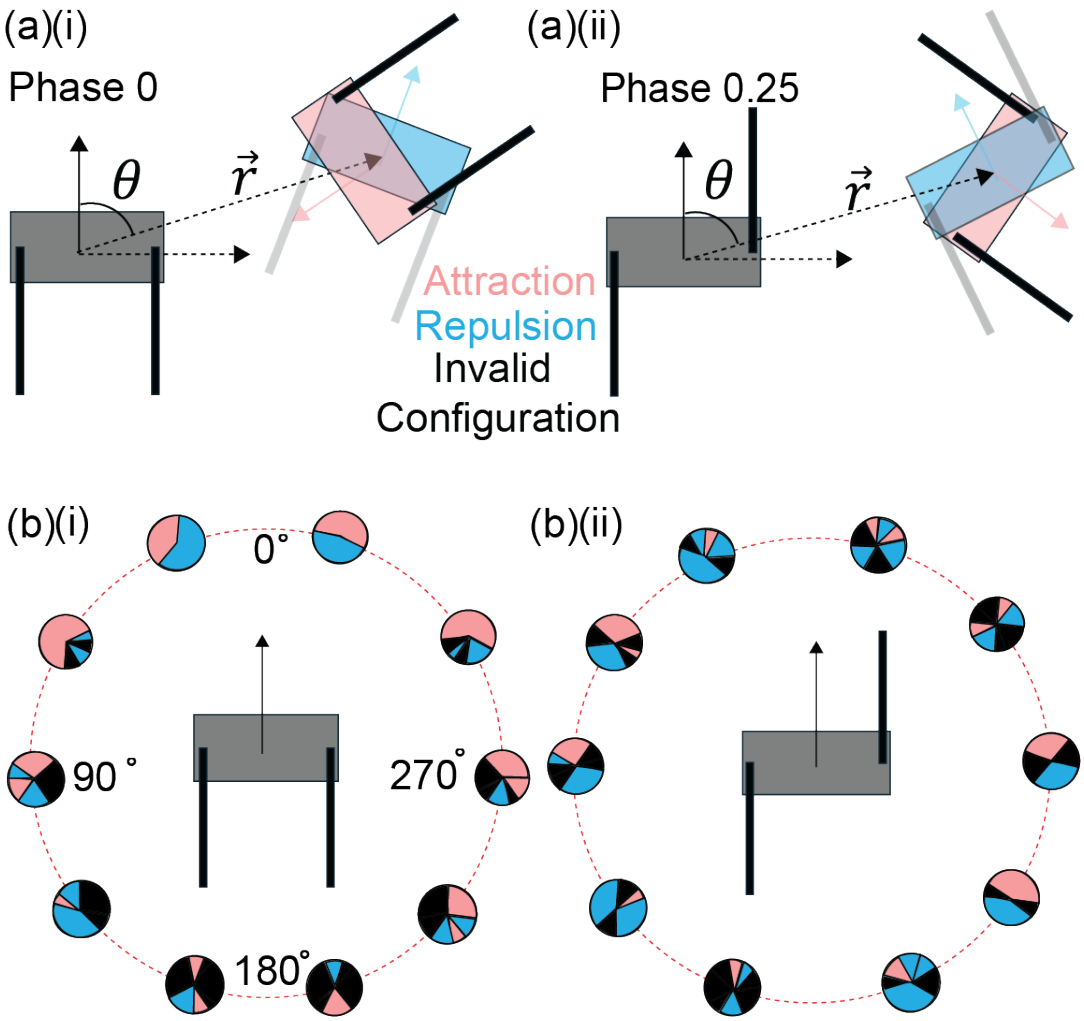

Figure 3.6: Constant radius polar grid scan reveals the sterically allowable regions for glider formation:(a) (i) Polar grid scan around a reference smarticle (gray) at a constant radius ($r = 1.3$ BL) for initial phase 0, showing an attracted (pink) and repelled (blue) initial configuration. The heading of the second smarticle is varied at a fixed polar angle, θ. (ii) The corresponding scan for phase 0.25 shows the change in the basin of attraction across different initial robot shape spaces. (b) (i-ii) The scanned space is divided into regions of attraction (pink), repulsion (blue), and invalid configurations (black) for the two phase values.

are likely to repel (blue sectors) or be physically inadmissible (black sectors). In contrast, configurations in the second and third quadrants are generally repelled or physically inadmissible, as shown in Figure 3.6(b)(i-ii) and Figs. A4 and A5. Once on the attractor, we analyzed a single gait period for the two glider configurations to identify collisions driving attraction and transport during the cycle. Plotting the instantaneous change in robot separa-

tion, $\Delta r = r_i - r_{i-1}$, over time reveals that for the C1 dyad, attraction arises when the arms briefly hook onto each other during the cycle (Figure 3.7(a)(i), collision 2). In contrast, Figure 3.7(a)(ii) reveals that for the C2 dyad, attraction results from the robots' alternating arms bracing each other's bodies (collisions 1 and 3). Both events are marked by a sharp decrease in Δr, as seen in Figure 3.7(b)(i-ii).

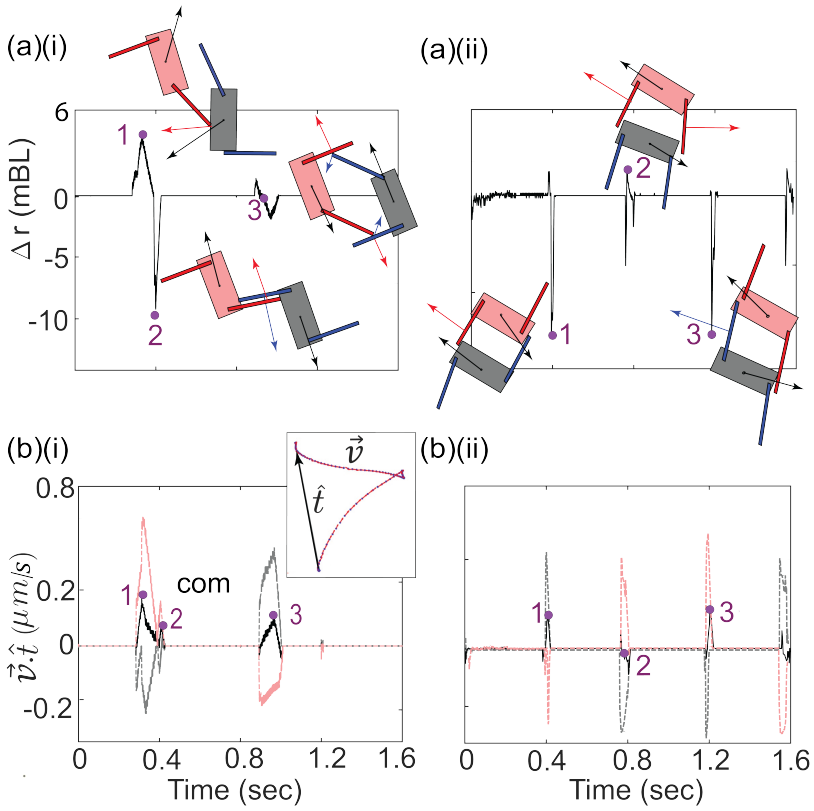

Figure 3.7: Collisions leading to attraction and transport within a gait cycle: (a) Collision events for a C1 dyad (i), where attraction arises from arm hooking and repulsion from arm-body collisions, and for a C2 dyad (ii), where attraction results from alternate arms colliding with each other's bodies and repulsion from steric interactions when one robot's body is fully enveloped by the arms of the other. The change in robot separation, Δr, over time shows sharp spikes that correlate with attraction events for both dyads. (b) Projections of the robots' instantaneous velocities onto the effective stepping vector reveal individual displacements along the transport direction, highlighting a leader-follower dynamic where one robot leads and the other is carried along. This links transport to repulsive collisions in both dyad types (i-ii).

The net displacement of the paired robots in the heading direction during a single cycle is calculated by taking the area under the curve of the dot product of their instantaneous

velocity $\vec{v}$ and the glider's effective stepping vector of the center of mass $\hat{t}$ for the cycle. For the C1 dyad, transport occurs primarily when the arm of the robot maintaining the orientational asymmetry (Leader) briefly collides with the body of the other robot (Follower) before hooking onto its arm to create attraction. This collision 1, shown in panel Figure 3.7(a)(i), causes the robots to move in opposite directions, with the leading robot driving the net transport (Figure 3.7(c)(i)). In contrast, the C2 dyad exhibits transport driven by collisions, where one robot's arms alternatively envelope the body of the other every half-cycle, as shown in collision 2 of Figure 3.7(a)(ii). These collisions cause both robots to move in opposite directions (Figure 3.7(c)(ii)). However, the displacement magnitudes for both robots are almost similar, and the effect accumulates over multiple cycles, eventually causing the dyad to break

3.8 Feedback Stabilization of Sterically Unstable Configuration with Tactile Sensing

The slightly asymmetric C2 glider typically unbound permanently (and thus stopped translating) within 60-70 cycles as the smarticles compressed each other into a non-colliding state. This glider conformation involved the two robots fully enclosing each other in the space between their arms every half cycle, as shown in collision 2 of Figure 3.7(a)(ii), causing them to move further apart due to compression. These steric effects, accumulated over multiple cycles, caused the bound pair to eventually disengage and remain barely in contact. To mitigate this repulsion, we employed a simple contact-sensing feedback strategy. We constructed slightly larger robots and mounted resistance-based force sensors on all four faces of the arms, as shown in Figure 3.8(a). We calibrated these force sensors based on the forces generated during the compression collision in the typical C2 conformation (Fig. A6). Using this impact threshold, we implemented a feedback strategy where the robots stopped moving their arms upon detecting an impact within that range and resumed movement from that position in their next gait cycle, as shown in Figure 3.8(b). This impact-based amplitude modulation stabilized the C2 glider. Figure 3.8(c) shows a plot

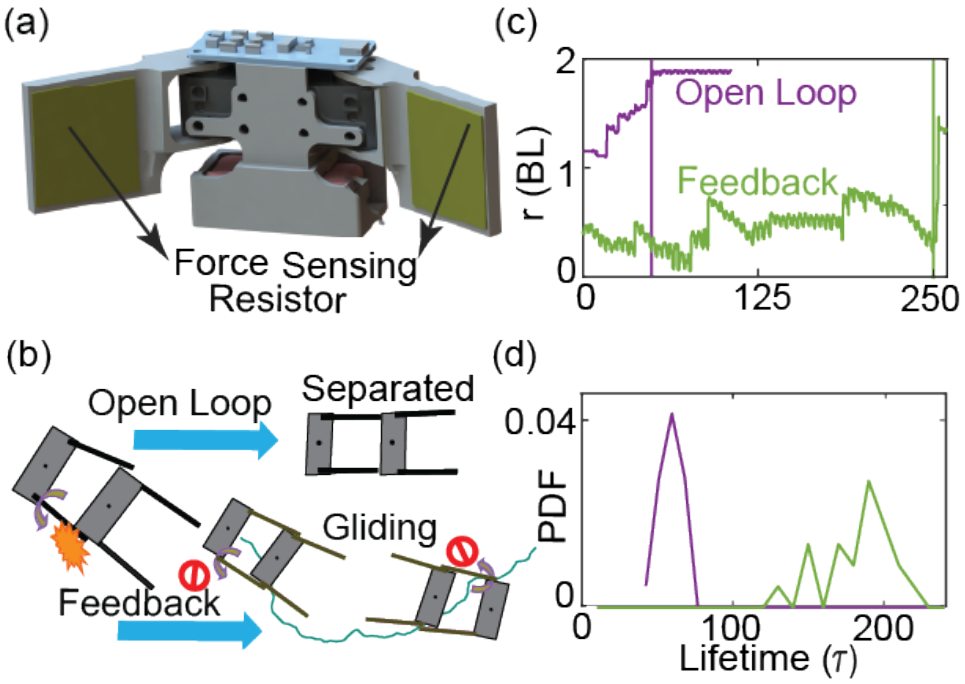

Figure 3.8: Stabilizing the sterically unstable mode via tactile sensing: (a) Smarticles equipped with force sensing resistors on the four arm faces stabilize the sterically unstable C2 configuration (details in SI). (b) Mechanism illustrating the destabilization of open-loop and stabilization of feedback-enabled C2 gliders. (c) Time evolution of r for a representative open-loop and feedback-glider trial. Open-loop dyads push apart to stable fixed points, while feedback-enabled dyads remain in a transient mode for longer periods due to concavity modulation. Solid lines mark glider break-down. (d) Glider lifetime distributions for open-loop and feedback-enabled trials.

of r vs. time (in gait periods) for a representative open-loop and feedback-controlled C2 glider, illustrating how the closed-loop strategy keeps the value of r fluctuating transiently. The distribution of lifetimes for C2 gliders with different open-loop arm amplitudes (with 70° as the cutoff, beyond which no C2 gliders form) compares to the feedback-stabilized glider in Figure 3.8(d). The control strategy significantly improved the lifetime of this unstable open-loop excitation, keeping it dynamically evolving, as shown in the relative configuration space in Fig. A7. The transport properties of the various C2 gliders with different arm amplitudes are shown in Fig. A8. The open-loop C2 glider with an amplitude of 85° and the feedback-controlled C2 glider move almost ballistically, but the longer lifetime of the feedback-stabilized glider ensures it to transport over longer distances.

3.9 Conclusion.

We studied ensembles of shape-changing robots (smarticles) in experiments and simulations, revealing the novel phenomenon of *gliders*– dynamically bound pairs that travel together with almost ballistic locomotion, over many body lengths and enduring hundreds of rigid-body collisions between them. We characterize gliders by their relative spacing and orientation, demonstrating that their formation emerges from a delicate interplay between the robot's geometric positioning and arm phasing. The stability and lifetime of these gliders depends on how the robots collide and envelop each other within the space between their arms during a gait cycle. Using an impact-sensing feedback strategy to modulate the concavity, we significantly enhanced the binding of the unstable mode. Surprisingly, these physical gliders can assemble into long structures upon colliding with other robots, giving rise to long-range order in the collective, similar to non-reciprocally interacting spin models [126, 127]. We also observed a transition from static bound states to locomoting gliders, depending on the amount of non-reciprocity programmed into the gaits. A detailed analysis of how glider transport can be understood and modulated by enumerating the symmetries of glider configurations and the gaits executed by the robots is in preparation[115]. We suggest that gliders may emerge in diverse active matter systems, where interacting shape-changing objects adopt concave shapes during non-reciprocal deformations in a sufficiently damped environments, highlighting the rich dynamics of highly deformable active bodies. These findings highlight principles for dynamically entangling collectives, paving the way for directed self-assembly and transport in active shape-changing systems.

CHAPTER 4
SYMMETRY BREAKING TRANSPORT IN GLIDING DYADS FORMED BY COLLISIONS

4.1 Summary

The asymmetry between the two bound modes of the dyad suggests a deeper connection between broken symmetries and the mechanism of transport. In this chapter, we investigate how transport in "gliding dyads" emerges from the interplay between dynamical and configurational symmetries. We show that initial collisions between robots break exchange symmetry, establishing a leader-follower relationship that underlies persistent gliding motion in the dyad's center-of-mass frame. By systematically biasing robot shapes, we enhance and rectify transport by amplifying non-commutative displacements generated by non-reciprocal square gaits. Using simulations, we explore how increasing the gait area drives transitions from time-reversible straight-line gaits to time-irreversible square gaits.

Along one transition pathway, the anti-parallel conformation forms the only stable bound state, which remains stationary until a critical gait area is exceeded, beyond which it begins to glide. In contrast, the parallel conformation remains unstable and transient. Along a different transition path, increased configurational freedom during shape oscillations leads to stable coexistence of both gliding modes. The time-irreversibility of the gaits is reflected in the chirality of dyad trajectories, allowing directional control by simply time-reversing the gait with minimal feedback. These results provide new design principles for self-assembling robotic collectives that harness symmetry breaking and time-asymmetric dynamics for robust coordination and locomotion.

[0]This chapter is adapted from sections of a manuscript in preparation.

4.2 Introduction

Symmetry and its breaking are central to physics, governing conservation laws, phase transitions, and emergent phenomena across classical, quantum, and cosmological systems [128, 129]. In phase transitions, ferromagnetism arises when randomly oriented spins align below the Curie temperature, breaking rotational symmetry and inducing spontaneous magnetization [130]. Similarly, crystallization transforms a liquid into a solid by breaking continuous translational symmetry, giving rise to periodic atomic structures and phonon excitations [131]. In superconductivity, the spontaneous breaking of U(1) gauge symmetry—linked to the conservation of the electromagnetic four-current—leads to Cooper pair condensation [132, 133], manifesting in the Meissner effect as magnetic fields are expelled and the photon acquires an effective mass [134]. This, in turn, gives rise to the Higgs mode as a collective excitation [135, 136]. More generally, in many-body systems, increasing levels of broken symmetry correlate with greater complexity and functional specialization [137]. In active matter, where nonequilibrium dynamics inherently break time-reversal symmetry, symmetry breaking acquires an even richer dimension. Sustained energy injection and dissipation drive emergent behaviors beyond equilibrium constraints, producing novel collective dynamics and multi-scale symmetry-breaking patterns [138, 58, 139].

Non-reciprocal interactions, which break action-reaction symmetry, drive self-organization across diverse collective systems and scales [20, 91]. Antagonistic forces underlie emergent dynamics in a wide range of systems, from strain competition in epidemics and promoter-inhibitor interactions in cell differentiation [95] to microbial suspensions of competing species [92, 93, 94], social interactions in human crowds [100, 101, 102, 103], and leader-follower dynamics in hierarchical pigeon flocks [104]. At the mesoscopic scale, non-reciprocity naturally emerges when interactions are mediated by a non-equilibrium medium [108, 107]. Catalytically active colloids with tunable non-reciprocity exhibit rich emergent behaviors, including transport, waltzing, and self-assembly into active molecules [52, 53,

109, 140] . Most studies of emergent spatiotemporal dynamics under non-reciprocity employ models of conserved fields [97, 141], excitable media [142], spins [126, 127], motile rods [143] , and coupled oscillators [144] . Non-reciprocity manifests through antagonistic cross-diffusivities in concentration fields, asymmetric coupling in oscillator phases, and alignment torques in spins and rods. As non-reciprocity increases, these systems undergo phase transitions, giving rise to distinct self-organized states, with traveling states emerging at high non-reciprocity levels [99, 21]. Insights from non-Hermitian physics have guided the design of non-reciprocal robotic metamaterials [145] and enabled unidirectional soliton and anti-soliton propagation in active metamaterials [113].

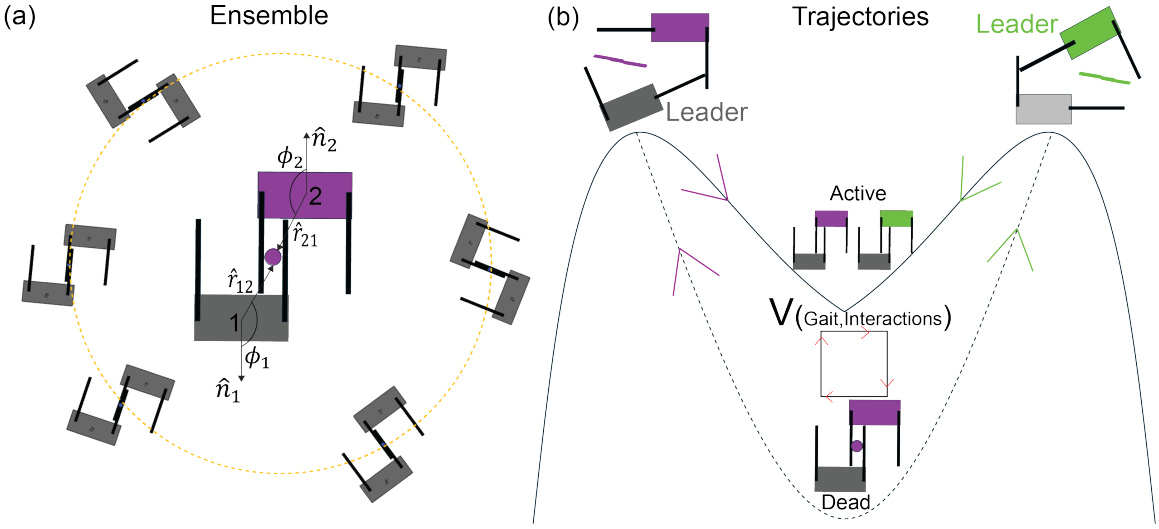

Figure 4.1: Breaking exchange symmetry. (a) An ensemble of perfectly anti-parallel dyad configurations was generated by translating and rotating the configuration in space. Two overlaid trials of the initial condition, with COM trajectories shown in the frame of robot 2's (purple/green) initial heading. Angular coordinates, ϕ_1 and ϕ_2, capture exchange symmetry between the robots. (b) Post-collision positions reveal stochastic exchange symmetry breaking, designating one robot as the leader and the other as the follower. When robot 2 (green) becomes the leader, the dyad moves right; when robot 1 (dark gray) leads, it moves left (shown in purple to indicate it's in the initial frame of robot 2). A schematic illustrating symmetry breaking, where the non-reciprocal square gait coupled with the collisional interactions determines the potential landscape. Transport direction is set by the first collision.

The asymmetry of the two emergent glider modes in [114]—one nearly antiparallel, the other nearly parallel—suggests a deeper link between broken symmetries and their transport [146, 124]. Since large-scale asymmetry often arises from asymmetry at smaller

scales [147], this motivates a systematic study of their emergence and transport in relation to the symmetries of their dynamics and prescribed deformation patterns. The square gait executed by the three-link robots is inherently non-reciprocal due to the time asymmetry introduced by one arm moving independently of the other [148, 123]. This sequential asymmetry breaks time-reversal symmetry, causing net locomotion over a full gait cycle [19, 149, 150]. This deformation pattern breaks action-reaction symmetry, akin to non-reciprocal interactions driving self-organization in biological and active systems. Formulated as a gauge field theory, the swimmer's arm motion traces a closed loop in shape space with a finite enclosed area, making non-reciprocity an intrinsic geometric property of its shape deformations [16, 151, 152, 17, 153]. Such geometric non-reciprocity underlies transport mechanisms in microswimmers and robotic locomotion in various overdamped environments. For dynamically bound dyads, Coulomb friction at the robot bases is strong enough to suppress internal motion from arm movements in isolated robots. However, it allows differential sliding between the robots due to time-ordered impulses exchanged between them—a signature of the commanded gait. As a result, the dyad undergoes directed transport maintaining a fixed asymmetry in the bound configuration, showing how non-reciprocal collisions drive coordinated transport of a robotic dimer.

We analyze the perfectly anti-parallel glider configuration; the sterically stable mode in an overdamped geometric regime, to show that transport directly correlates with dyad asymmetry. The first collision stochastically breaks exchange symmetry, causing one robot to deviate slightly from perfect anti-alignment. Nonlinear forces underlying the *active collisions* where the drive creates persistent contact between the bodies, brings about this indeterminism, designating the deviating robot as the leader [76, 154, 155]. Minute variations in the arms' contact points across different trials from the ensemble determine which body yields upon collision. This ensemble is generated by translating and rotating the anti-symmetric initial configuration in space, as shown in Fig. Figure 4.1(a). These variations arise from the nonlinear forces imparted during active collisions, breaking the exchange

symmetry between the robots for the trajectory. It then directs transport by striking the follower's body with its arm each cycle maintaining that asymmetry, as shown in (fig:Binding and Transport Mechanism)(a)(i) of [114]. The perfectly antisymmetric configuration exhibits no net transport due to its invariance under inversion or $R(\pi)$ rotation in the plane, making both left and right directions equally likely. The transport direction is determined by which robot stochastically breaks exchange symmetry to become the leader, serving as a clear demonstration of exchange symmetry breakdown, as shown in Fig. Figure 4.1(b). The commanded non-reciprocal square gait coupled with the underlying collisional interaction between the robots governs the effective potential between the robots during an active dyad.

We show that the direction and magnitude of transport is directly correlated with the transient oscillations in the exchange symmetry factored angular coordinates ϕ_1 and ϕ_2. Left and right heading trajectories, shown in robot 1's initial heading frame, have angular coordinates that are mirrored reflections of each other. Equipped with the understanding of how the dyad's spontaneous choice of heading stems from the stochastic breaking of exchange symmetry, we demonstrate that explicitly breaking this symmetry allows us to tune its transport direction and magnitude. By positively and negatively biasing the gaits of the two robots with fixed offsets from the standard square template, we impose a deterministic preference, rectifying the dyad's movement. We further show that dyad transport can be understood in terms of emergent noncommutativity, arising from the interplay between the commanded gait and collisions between the robots. We varied the non-reciprocity in the gaits parametrized by the gait area along two distinct paths in configuration space. One path led to the emergence of only the bound state deviating from anti-alignment, while the other produced both types of bound states. The configurations adopted by the robots along these paths explain the stability of the emergent modes. We also show that beyond a critical gait area (non-reciprocity), the transport of the anti-symmetric dyad undergoes a transition reminiscent of non-reciprocal excitations in other systems, shifting from static bound states

to gliders[21]. This transition underscores the fundamental role of non-reciprocity in sustaining locomotion [99], distinguishing the discrete hybrid-event nature of this system from the continuous systems where such transitions are typically observed. Lastly, we explore the subtle connection between non-reciprocity and chirality in these robots [58]. The direction of loop traversal determines which arm moves first, assigning each robot a chirality that manifests as curvature in the dyad's trajectory. By time-reversing the gaits via audio feedback, we can steer the glider, reinforcing the role of chirality in harnessing emergent transport.

4.3 Dyad Transport from broken Exchange Symmetry

4.3.1 Perfectly anti-symmetric initial configuration.

To demonstrate the breakdown of exchange symmetry between the robots, we define two angular coordinates, ϕ_1 and ϕ_2. These angles are evaluated by measuring the orientation of the relative position vector between the two robots with respect to each robot's body normal. Specifically, ϕ_1 is the angle between the unit vector $\hat{r}_{12}$, which points from robot 1 to robot 2, and robot 1's body normal unit vector $\hat{n}_1$. Similarly, ϕ_2 is the angle between the unit vector $\hat{r}_{21}$, which points from robot 2 to robot 1, and robot 2's body normal unit vector $\hat{n}_2$ as shown in Fig. Figure 4.1(a). We define the dyad (glider) configuration as

$$\mathbf{S} = (\hat{r}_{12}, \hat{r}_{21}, \phi_1, \phi_2). \tag{4.1}$$

The exchange transformation is

$$E(\hat{r}_{12}, \hat{r}_{21}, \phi_1, \phi_2) = (\hat{r}_{21}, \hat{r}_{12}, \phi_2, \phi_1). \tag{4.2}$$

Since the smarticles are identical, E is a symmetry of the evolution map f, which takes the dyad configuration at the beginning of a period and advances it to the configuration at the

start of the next period, i.e.,

$$E\big(f(\mathbf{S})\big) = f\big(E(\mathbf{S})\big). \tag{4.3}$$

If

$$f(\mathbf{S}) = (\hat{r}'_{12}, \hat{r}'_{21}, \phi'_1, \phi'_2), \tag{4.4}$$

then symmetry requires

$$f(\hat{r}_{21}, \hat{r}_{12}, \phi_2, \phi_1) = (\hat{r}'_{21}, \hat{r}'_{12}, \phi'_2, \phi'_1). \tag{4.5}$$

For an anti-parallel configuration with $\phi_1 = \phi_2 = \phi_0$, we have

$$f(\hat{r}_{12}, \hat{r}_{21}, \phi_0, \phi_0) = (\hat{r}'_{12}, \hat{r}'_{21}, \phi'_1, \phi'_2), \tag{4.6}$$

and by symmetry,

$$(\hat{r}'_{12}, \hat{r}'_{21}, \phi'_1, \phi'_2) = (\hat{r}'_{21}, \hat{r}'_{12}, \phi'_2, \phi'_1). \tag{4.7}$$

Thus, $\phi'_1 = \phi'_2$, ensuring the anti-parallel configuration remains unchanged under the dynamics. This invariant angle equality, combined with inversion symmetry, makes the configuration ideal for illustrating the breakdown of exchange symmetry after the first collision. Moreover, inversion symmetry guarantees zero net transport, as confirmed by simulations in the highly over-damped regime. We introduce the transformation

$$R_\pi(\hat{r}_{12}, \hat{r}_{21}, \phi_1, \phi_2) = (-\hat{r}_{12}, -\hat{r}_{21}, \phi_1 + \pi, \phi_2 + \pi). \tag{4.8}$$

to demonstrate the effect of rotation by π on the dyad configuration. Since both E and R_π are symmetries, the evolution map $f(\mathbf{S})$ satisfies

$$E\big(f(\mathbf{S})\big) = f\big(E(\mathbf{S})\big), \quad R_\pi\big(f(\mathbf{S})\big) = f\big(R_\pi(\mathbf{S})\big). \tag{4.9}$$

For a perfectly anti-symmetric configuration we set

$$\phi_2 = \phi_1 + \pi. \tag{4.10}$$

By shifting the origin to

$$\hat{r} = \frac{\hat{r}_{12} + \hat{r}_{21}}{2}, \tag{4.11}$$

the state becomes

$$\mathbf{S} = (\hat{r}, -\hat{r}, \phi, \phi + \pi), \tag{4.12}$$

which satisfies

$$E\, R_\pi\, \mathbf{S} = \mathbf{S}. \tag{4.13}$$

Assume that after one cycle the configuration rotates by an angle ψ and translates by Δr. Then

$$f(\mathbf{S}) = \Big(R_\psi(\hat{r}) + \Delta r,\ R_\psi(-\hat{r}) + \Delta r,\ \phi + \psi,\ \phi + \psi + \pi\Big). \tag{4.14}$$

Applying R_π gives

$$\begin{aligned} R_\pi\big(f(\mathbf{S})\big) = \Big(& -R_\psi(\hat{r}) - \Delta r, \\ & -R_\psi(-\hat{r}) - \Delta r, \\ & \phi + \psi + \pi, \\ & \phi + \psi \Big). \end{aligned} \tag{4.15}$$

By symmetry,

$$\begin{aligned} f\big(R_\pi \mathbf{S}\big) = E\Big(f\big(E\, R_\pi \mathbf{S}\big)\Big) = \Big(& R_\psi(-\hat{r}) + \Delta r, \\ & R_\psi(\hat{r}) + \Delta r, \\ & \phi + \psi + \pi, \\ & \phi + \psi \Big). \end{aligned} \tag{4.16}$$

Equating the corresponding components yields

$$-R_\psi(\hat{r}) - \Delta r = R_\psi(-\hat{r}) + \Delta r. \tag{4.17}$$

Since $R_\psi(-\hat{r}) = -R_\psi(\hat{r})$, we conclude that

$$\Delta r = 0. \tag{4.18}$$

Thus, with $\Delta r = 0$, the perfectly anti-symmetric dyad configuration shows no net transport.

Figure 4.2(a) confirms this by displaying an ensemble of simulated trajectories (see SM of [114] for simulation details) that spread equally and oppositely. These trajectories were obtained by rotations and translations of the perfectly anti-symmetric initial configuration and are represented in a common frame attached to the initial heading of the second (col-

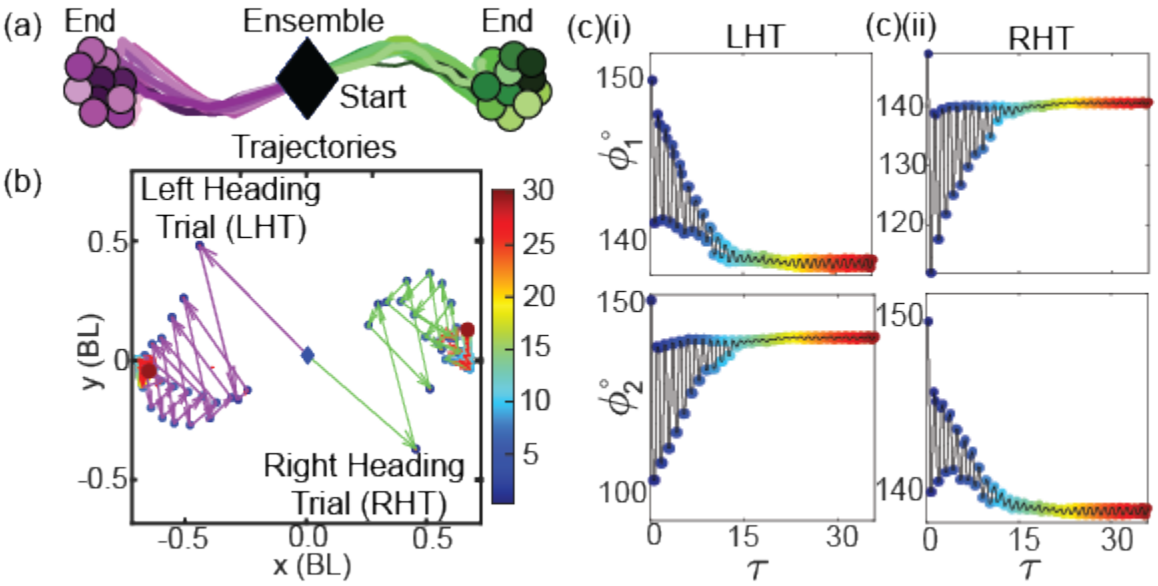

Figure 4.2: Symmetry breaking data. (a) Resultant trajectories from the ensemble are plotted in the frame of the initial condition attached to robot 2 (colored) in Figure 4.1. The black diamond denotes the common starting point for all trajectories and the circles indicating the end points for the trials, depicting the spread in the ball of initial conditions sampled. (b) Zoomed in representation of the com trajectory for a left and right heading trial color coded with the gait period. (c) The exchange symmetry is broken by the first collision, making one robot the leader. The leader exhibits a larger deviation from equilibrium, reflected in transient oscillations before relaxing back to a fixed point. (i) The time evolution of ϕ_1 and ϕ_2 (in terms of gait period τ) for a left-heading trial. Similarly (ii), represents the corresponding values for a right-heading trial.

ored) robot in Figure 4.1. Individual trajectories from the ensemble transiently break the exchange symmetry, causing one robot to become asymmetrical in it's relative orientation w.r.t. the other and drive transport. This robot becomes the leader for the trajectory and determines the direction of transport. Two individual trajectories from the ensemble which went left and right respectively are shown in Figure 4.2(b). The spontaneous selection of a leader is clearly evident in the time evolution of ϕ_1 and ϕ_2 shown in Figure 4.2(c). Notably, the angular coordinates are swapped between the left and right heading trials, providing a clear marker of how the leader stochastically selects the direction of transport. Further, the magnitude of transport is correlated with the transient oscillations in these coordinates and transport ceases, when the values of ϕ_1 & ϕ_2 relax back to the fixed point, which is the perfectly anti-parallel configuration. The initial anti-parallel configuration is inert, while

the relaxed configuration is active—sustained by continuous energy injection and dissipation. This distinction is marked by the dotted curve in Figure 4.1(b), which denotes the equilibrium energy landscape. This stable equilibrium spontaneously bifurcates into two unstable periodic orbits which drive transport transiently along two different directions, before relaxing back to the active fixed point.

4.3.2 Generalized scan depicting steady state attractor topology and transport.

To characterize the basin of attraction of generic emergent gliders, we performed a generalized scan by fixing one robot (gray) and randomly initializing the second robot in various positions and orientations within a 6.5 BL radius. Figure 4.3 visualizes this scan, where the robots are represented as spins aligned with their body normal. Grey arrows denote repelled configurations, while black arrows indicate those that are attracted.

To visualize the steady-state attractor, we represent the dynamics using exchange symmetry-factored relative coordinates, as shown in Fig. Figure 4.4. The C1 glider dominates as the primary attractor, forming a *saddle*-like structure in the full 3D representation (panel a). Its two wings correspond to unstable periodic orbits where symmetry was transiently broken for the perfectly anti-symmetric initial configuration. In generic asymmetric configurations, these orbits tend to stabilize and persist as long-lived transients. A smaller cluster of red points represents the transient C2 glider, a sterically unstable mode described in [114]. Fig. Figure 4.4(b) projects this structure onto the ϕ_1-ϕ_2 plane, revealing near-perfect reflection symmetry across $\phi_2 = \phi_1$ with a slight imbalance in state occupancy between the symmetry-broken wings. Unstable periodic orbits define the wings of the saddle-shaped C1 attractor, where spontaneous symmetry breaking guides the system onto one branch. Since the attractor emerges from collisional interactions modulated by the commanded gait, the effective potential is dynamically generated and non-conservative. The C2 transient, an unstable mode, represents a high-energy saddle point in this potential, ultimately relaxing into the stable equilibrium of two separated robots, highlighting the decisive influence of

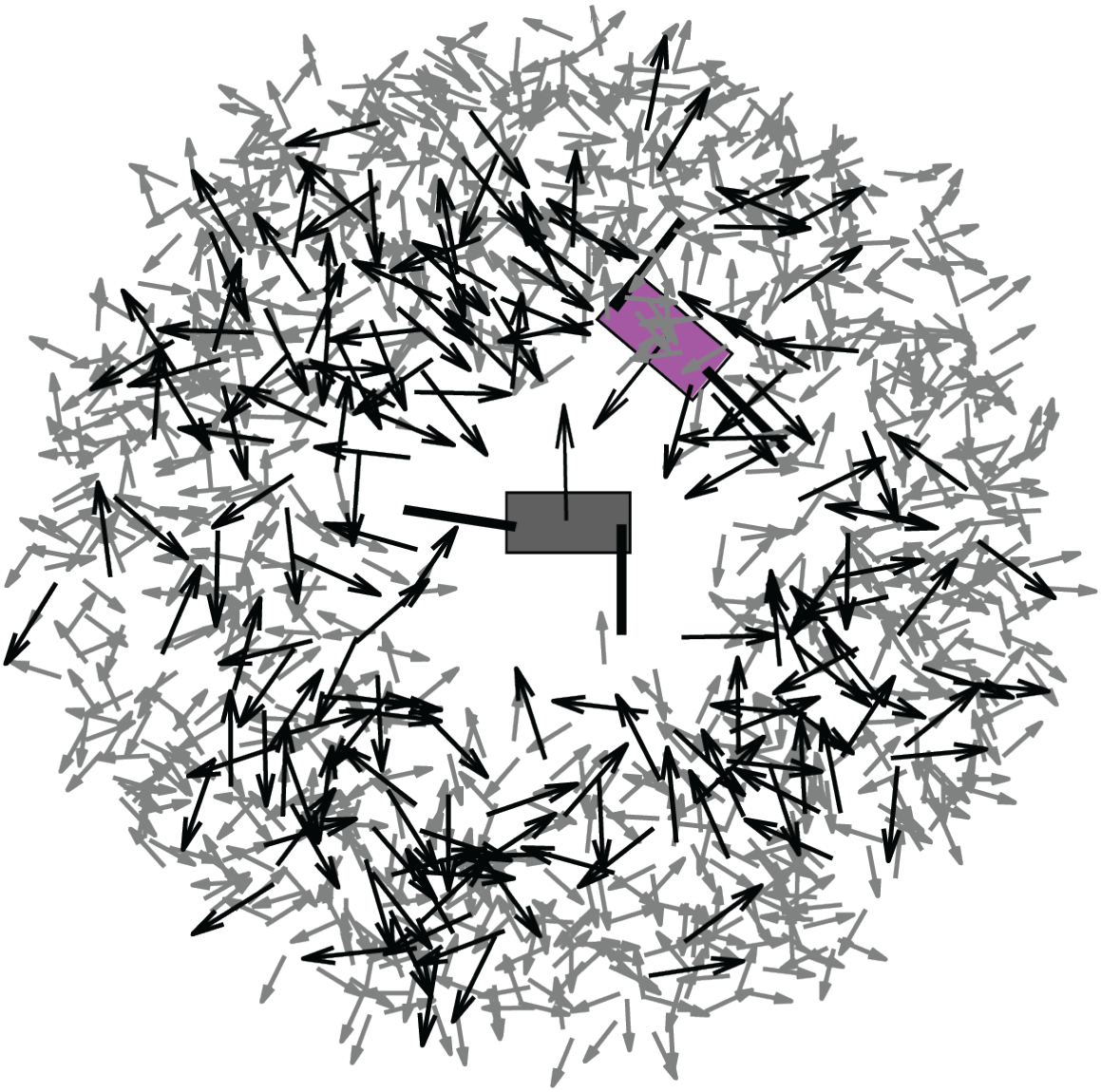

Figure 4.3: Representation of a generalized scan wrt the reference (grey) robot upto $r = 6.5BL$ at a constant initial phase. The scanned robots are depicted with their normal vectors attached to their body centers. Grey arrows represent repelled configurations, while black arrows represent attracted configurations.

steric constraints in shaping the potential. The attractor topology is fundamentally determined by the prescribed gait, emphasizing that different commanded templates will sculpt distinct dynamical landscapes.

Figure 4.5 shows a scatter plot of the center-of-mass (CoM) displacement per cycle for steady-state gliders in the lab frame. The nearly isotropic distribution suggests an almost equal likelihood of movement in all directions. Figure 4.6 presents the distributions of

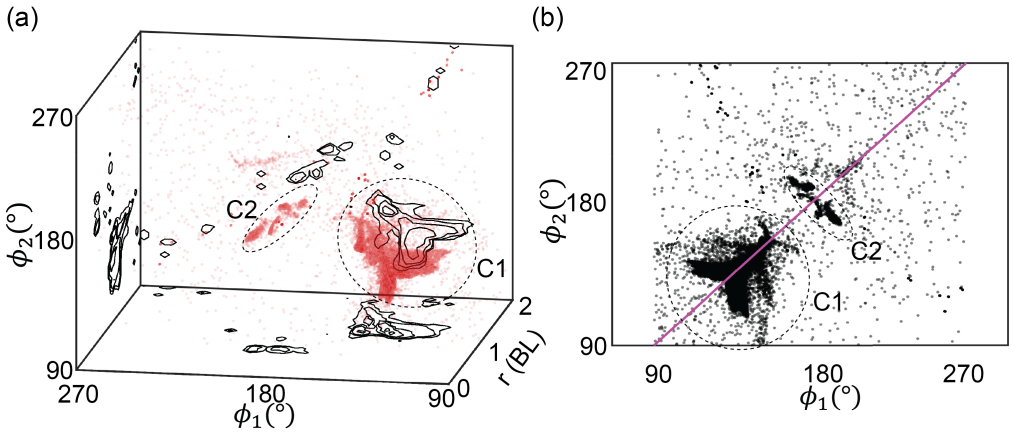

Figure 4.4: Topology of steady state attractors. (a) Steady state attractors formed by the dyads surviving the entire duration of the trial. (b) Attractor projection in the ϕ_1 & ϕ_2 plane highlighting the broken symmetry about the fixed point.

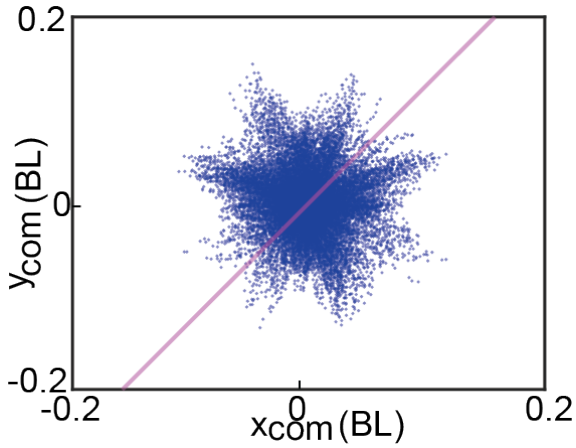

Figure 4.5: Scatter plot of the center-of-mass coordinates for steady-state gliders, strobed per cycle, expressed in the lab frame.

the dyad com displacement components and angular displacement. The translational and angular displacement of the com are computed by transforming the robot coordinates into a co-moving frame centered at the com and aligned with the average heading of both robots. This transformation ensures that displacements are measured relative to the dyad's intrinsic motion rather than in the lab frame.

We transform the robot coordinates into a co-moving frame centered at the com and aligned with the vector pointing from robot1 to robot 2. At each timestep, the center of mass (CoM) of the dyad is computed as the mean position of the two robots C_i:

Its displacement is then given by:

$$\Delta C_i = C_{i+1} - C_i.$$

The intrinsic reference frame is defined using the unit vector from $\vec{S}_1$ to $\vec{S}_2$ and is given by:

$$\hat{r}_i = \frac{\vec{S}_2 - \vec{S}_1}{\left\| \vec{S}_2 - \vec{S}_1 \right\|}$$

To express the CoM displacement in this reference frame, we apply the rotation matrix:

$$R = \begin{bmatrix} 0 & -1 \\ 1 & 0 \end{bmatrix},$$

which rotates a vector by 90°. The CoM displacement components in this intrinsic frame are then:

$$s_{\hat{r}_x} = \Delta C_i \cdot \hat{r}_i, \quad s_{\hat{r}_y} = \Delta C_i \cdot (R\hat{r}_i).$$

These quantities characterize the dyad's movement along its principal directions.

The resulting distributions illustrate the dyad com displacement is predominantly along the principal direction $s_{\hat{r}_y}$, while the other main direction $s_{\hat{r}_x}$ has slightly smaller displacements. Both translational and angular displacement $\Delta\theta$ exhibit almost symmetrical distributions, capturing the isotropic nature of displacements around the main heading directions. There is a nominal directional bias along$-s_{\hat{r}_y}$ that reflects the slight asymmetry in the steady-state attractor, indicating a slight preference for one lateral direction. Asymmetries in attractor wings often emerge in systems that undergo spontaneous symmetry breaking, typically driven by inherent real-world imperfections. Such asymmetries have been observed in various physical systems, where controlled asymmetry can stabilize symmetry-broken states, as seen in oscillator networks [156, 157] and spontaneous symmetry breaking in optical systems [158].The symmetric distribution of $\Delta\theta$ centered on 0° with

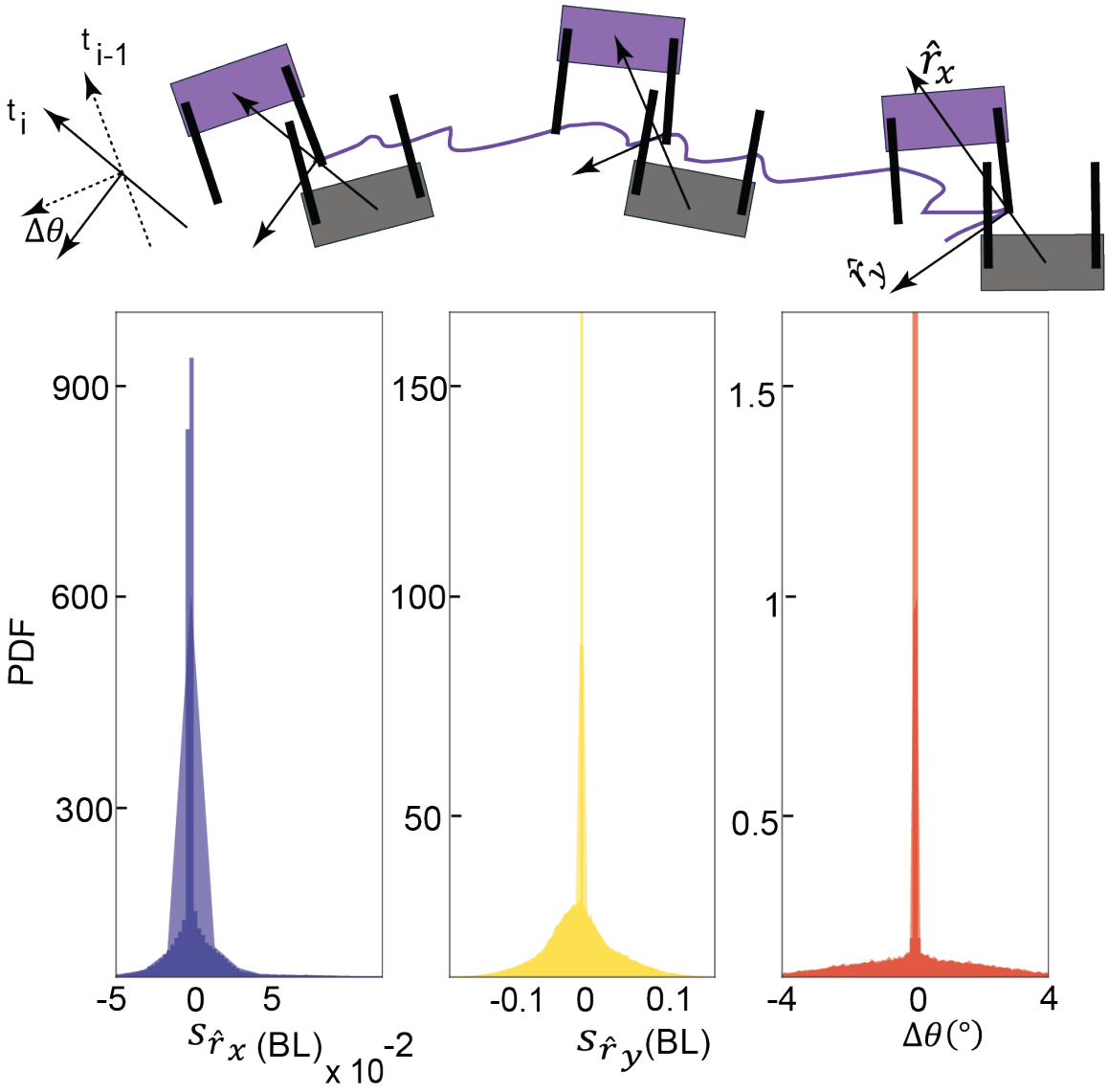

Figure 4.6: The translational and angular displacement of the dyad center of mass (CoM) are computed by transforming coordinates into a co-moving frame centered at the com and aligned with the vector pointing from robot 1 (grey) to robot 2 (purple). This yields the distributions for the com displacement components $s_{\hat{r}_x}$, $s_{\hat{r}_y}$, and the angular displacement $\Delta\theta$.

a small variance suggests minimal directional fluctuations and strong persistence in the dyad's heading over time, indicating that individual trajectories maintain their orientation with little deviation.

4.3.3 Mapping an asymmetric dyad configuration across attractor wings to modulate transport.

Generic dyad configurations deviate systematically from perfect anti-alignment, directly influencing their transport direction. To map an asymmetric initial configuration onto its counterpart on the reflected attractor wing, we transform both robots into a common reference frame centered at their initial center of mass, with robot 1's (gray) body normal aligned along the x-axis as shown in Figure 4.7 (a).

Given an initial dyad configuration $\mathbf{S} = (\hat{r}_{12}, \hat{r}_{21}, \phi_1, \phi_2)$, we apply a rotation:

$$\begin{bmatrix} x_i' \\ y_i' \end{bmatrix} = R_{-\phi_1(0)} \begin{bmatrix} x_i \\ y_i \end{bmatrix}, \quad \phi_i' = \phi_i - \phi_1(0), \tag{4.19}$$

which aligns robot 1 with the x-axis. We then swap the robots, exchanging their relative positions and orientations:

$$E(\hat{r}_{12}', \hat{r}_{21}', \phi_1', \phi_2') = (\hat{r}_{21}', \hat{r}_{12}', \phi_2', \phi_1'). \tag{4.20}$$

This transformation rotates the dyad's center-of-mass trajectory by approximately the same angle:

$$\mathbf{C}'(t) = R_{-\phi_1(0)}\mathbf{C}(t), \tag{4.21}$$

demonstrating that relative asymmetry dictates transport and providing a direct means to control dyad locomotion by tuning initial asymmetry.

The central configuration in Figure 4.7 (a) illustrates this mapping, where an asymmetric initial state (green and gray robots) is mapped onto a new asymmetric configuration with the purple robot replacing the green one. This subtle change in relative positioning determines which robot's arm strikes the other's body, establishing a leader and setting the direction of locomotion. By constructing ensembles for these two initial states, we track

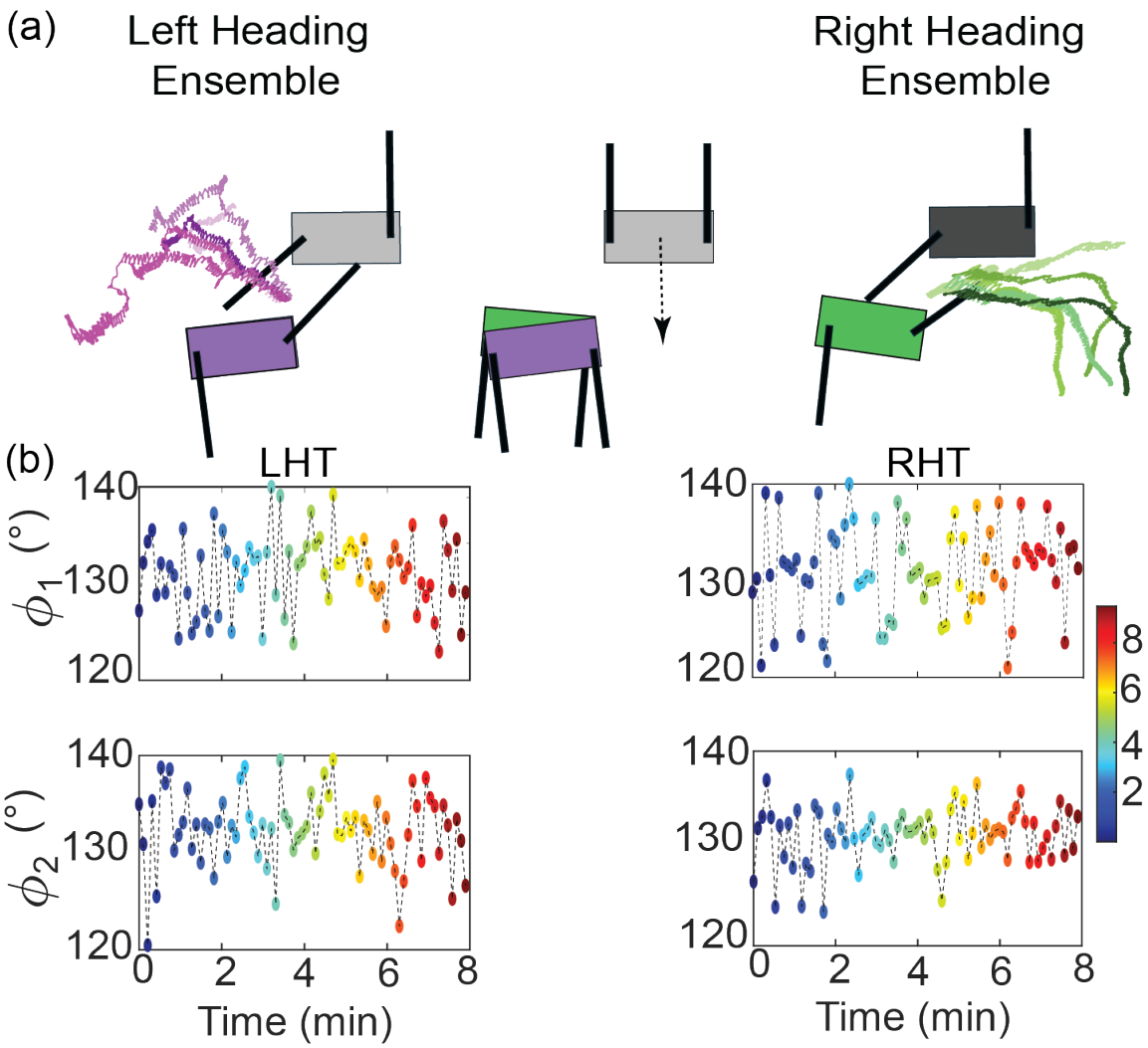

Figure 4.7: Modulating dyad transport by mapping an asymmetric dyad across attractor wings. (a) An asymmetric initial configuration maps onto its counterpart on the reflected attractor wing (center), resulting in two overlaid configurations with asymmetries related by symmetry operations. Subtle differences in relative robot positioning dictate a deterministic left or right movement, with trajectory rotated by approximately the same angle as the initial configuration. (b) The time evolution of the angular coordinates ϕ_1 & ϕ_2 for two representative trajectories from the ensemble.

their center-of-mass trajectories, revealing a deterministic preference for direction based on the initial asymmetry.

As shown in Figure 4.7 (b), the strobed angular coordinates ϕ_1, ϕ_2 fluctuate persistently in representative trials, sustaining transport for asymmetric initial conditions. In contrast, a perfectly antisymmetric configuration reverts to its original state, as discussed in Sec-

tion subsection 4.3.1.

4.4 Rectifying transport by controllably breaking exchange symmetry.

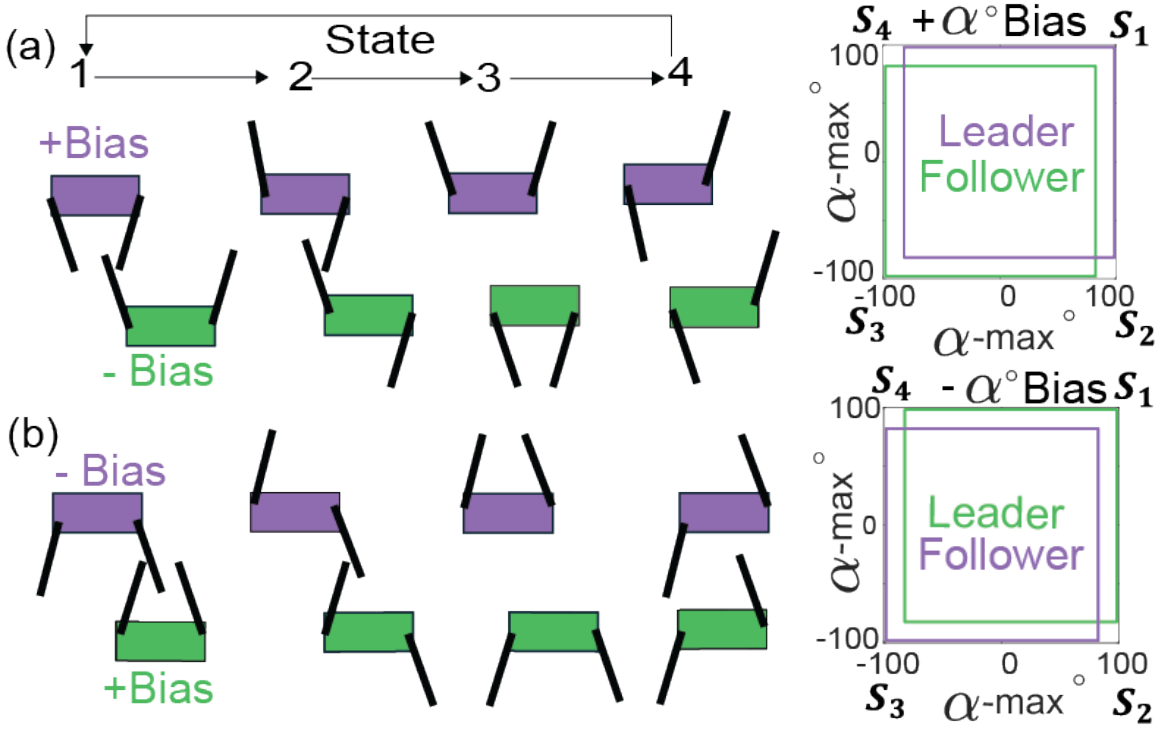

Figure 4.8: Breaking exchange symmetry explicitly by biasing configuration space of the robots. (a) Robots traverse four key configurations in their biased gaits, with bias introduced at the four corners as additional opening/closing from the arm angles $\{-\alpha_{\max}, -\alpha_{\max}\}$ and $\{\alpha_{\max}, \alpha_{\max}\}$. The shape space of arm angles is shown alongside the physical configurations. (b) Swapping gaits reverses the roles of the robots, enabling the sweep of a full range of bias values.

A perfectly antisymmetric initial configuration, which initially shows no net transport, can be rectified to deterministically select a heading and achieve persistent motion. This is done by altering the robots' gaits and introducing a fixed offset from the perfect square template with $\alpha_{\max} = 90°$. The magnitude of this bias is identical for both robots, but one is positively biased while the other is negatively biased. The effective bias being defined with respect to robot 1. Figure 4.8(a) illustrates this biasing in shape space, causing each robot to follow distinct deformation paths during their periodic cycles. This breaks the initial exchange symmetry, setting a clear leader similar to the asymmetric initial configuration

described in Section subsection 4.3.3. The biases introduce a phase shift of half a cycle (T/2) between the gaits of the two robots. Robot 1 (positively biased, purple) follows the sequence $1 \rightarrow 2 \rightarrow 3 \rightarrow 4$, while Robot 2 (negatively biased, green) performs the same gait in a different order $3 \rightarrow 2 \rightarrow 1 \rightarrow 4$. The gait of Robot 2 is obtained by translating Robot 1's gait forward in time by half a cycle, $\tau \rightarrow \tau + T/2$, followed by a time-reversal transformation, $\tau \rightarrow -\tau$. Swapping the robots' gaits while keeping their positions unchanged reverses their roles and direction of motion, as shown in Figure 4.8(b).

This enables precise control over bias values, explicitly breaking exchange symmetry in a controllable manner and modulating transport, as opposed to modulation through mapping relative asymmetry which involved mathematical transformations on an initial configuration. Further we can sweep through an entire range of bias values based on this scheme and are able to deterministically steer gliders from left to right. The magnitude of transport is proportional to the amount of bias programmed into the gaits. Figure 4.9 presents the translational and angular displacements of the dyad's center of mass (CoM) in the co-moving frame described in Section subsection 4.3.2, across different bias values. The extremal bias values are constrained by the maximum allowable angle before arm-body collisions occur. We rectify the motion of the dyads with this scheme, and make them head deterministically from left to right. The magnitude of the displacement is proportional to the amount of bias programmed into the gait.

4.5 Emergent Non-Commutativity in dyad locomotion.

The spontaneously broken exchange symmetry between the robots forming the dyad pair enables it to break the rotational symmetry in the plane and transport persistently in a given direction. The commanded shape space of the individual robots couple together via periodic collisional interactions and give rise to an emergent shape space in the form of a limit-cycle attractor shown here in coordinates r, ϕ_1, ϕ_2 for 3 consecutive cycles in Figure B.1. This in turn gives rise to the displacement of the individual robots in a periodic

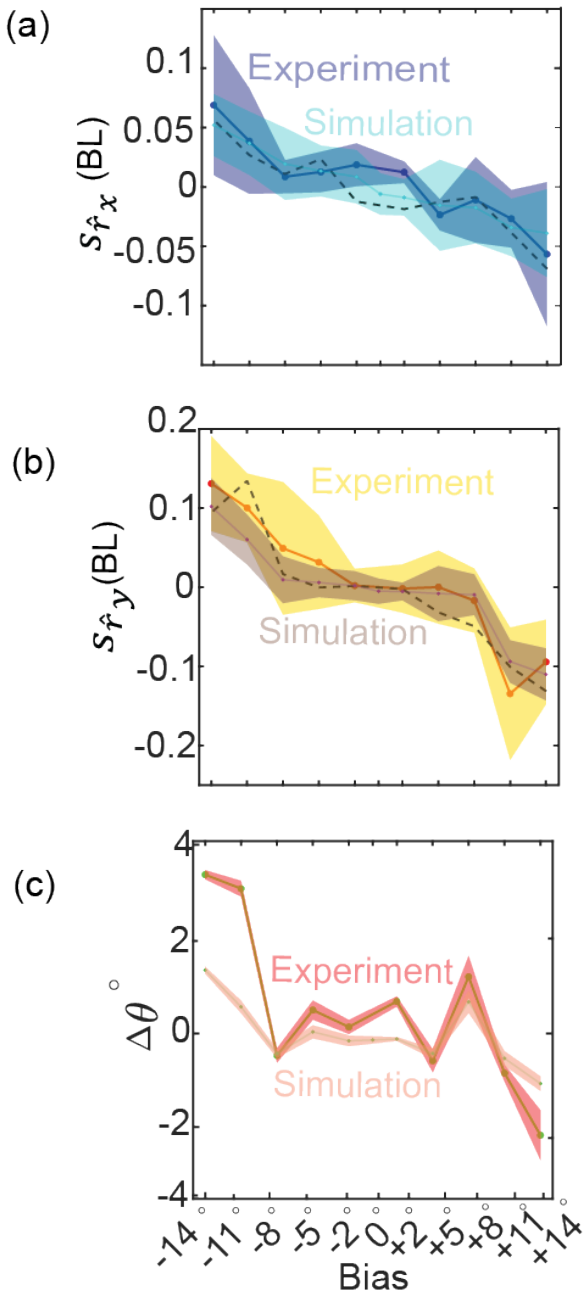

Figure 4.9: Modulating dyad transport by controllably breaking exchange symmetry. (a-c) The translational and angular components of the CoM displacement per cycle measured in the co-moving frame shown in Figure 4.6, depicts that the dyad transport can be tuned to pick a direction to the left or right based on the value of the bias with magnitude of displacement per cycle proportional to the magnitude of the bias.

way per cycle and causes the CoM to move along a fixed heading . This symmetry breaking and impending transport is a direct consequence of the inherent non-reciprocity of the square gait being executed in the CCW direction here. This non-reciprocity shows up as

an emergent non-commutativity in the transport of the robotic dyad due to the non-abelian nature of the $SE(2)$ lie group which is used for describing planar translations and rotations [159].

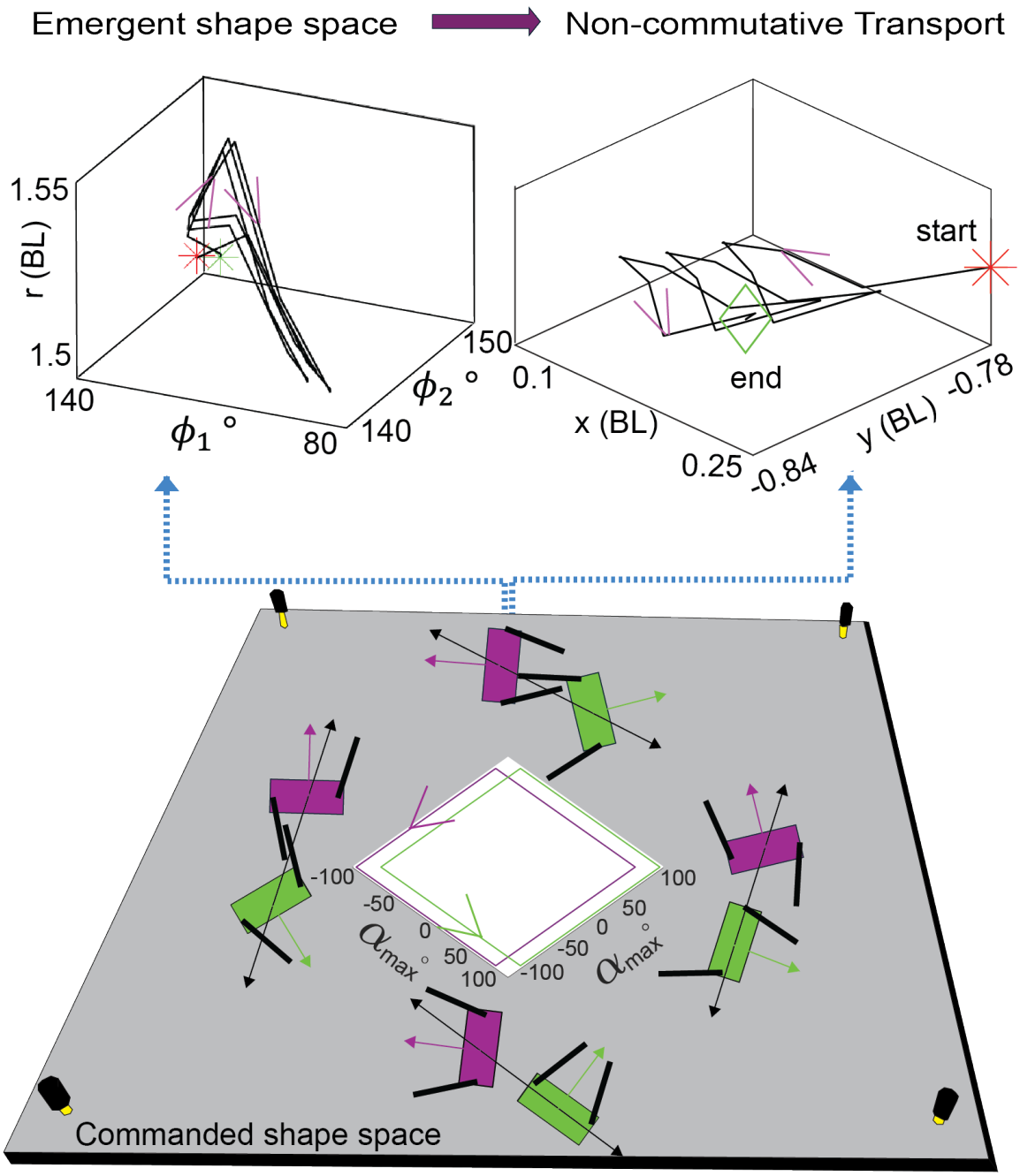

Figure 4.10: The emergent shape space of the dyad, arising from the commanded shape space of individual robots and their collisional interactions, causes a non-commutative transport of the dyad's center of mass (CoM).

To relate cyclic oscillations in the emergent shape space r, ϕ_1, ϕ_2 to transport, we model the dyad as a massless extensible rod linking the robot centers, undergoing planar expansion, contraction, and rotation, while tracking the center-of-mass coordinates (x, y, Θ) over each cycle. The net motion over a cycle can be understood by decomposing it into two half-cycles: during the first, the leader (Green) executes a counterclockwise (CCW) rotation about the nearly stationary follower (Purple); in the second, it reverses with a clockwise (CW) rotation. The follower acts as a pivot throughout, slipping only intermittently every few cycles during arm reconfiguration to catch up with the leader. The details depicting these events are shown in SM. These rotations are coupled to the robots cyclically drawing closer and sliding apart, captured by the shortening and lengthening of the massless extensible rod used to approximate their transport. Operating in the overdamped regime reinforces this approximation, as the absence of inertia suppresses fluctuations in the emergent shape space dynamics, reducing transitions between wings of the attractor and yielding more coherent cyclic behavior localized in one wing. In robotics and controls community, leader-follower models with cyclic pursuit are a common paradigm for analyzing coordinated motion and control in multi-agent systems. These models render themselves amenable to conducting stability and phase plane analyses after properly factoring out the symmetries [160, 161, 162, 163]. In contrast, our system does not impose such dynamics a priori; rather, leader-follower behavior emerges spontaneously as a result of gait-dependent interactions, revealing a richer, more nuanced structure of coordinated motion. The net displacement for the dyad arising from periodic shape changes can be captured by the Lie bracket of the vector fields corresponding to the two half-cycle motions. This commutator quantifies the extent to which the sequence of motions fails to commute—i.e., how performing one followed by the other differs from doing them in reverse. This same principle underlies maneuvers like parallel parking, where non-commutative drive and steering actions produce net motion otherwise inaccessible [18, 164, 78]. We derive the discrete vector fields for effective dyad displacement over the first and second half cycles, by considering

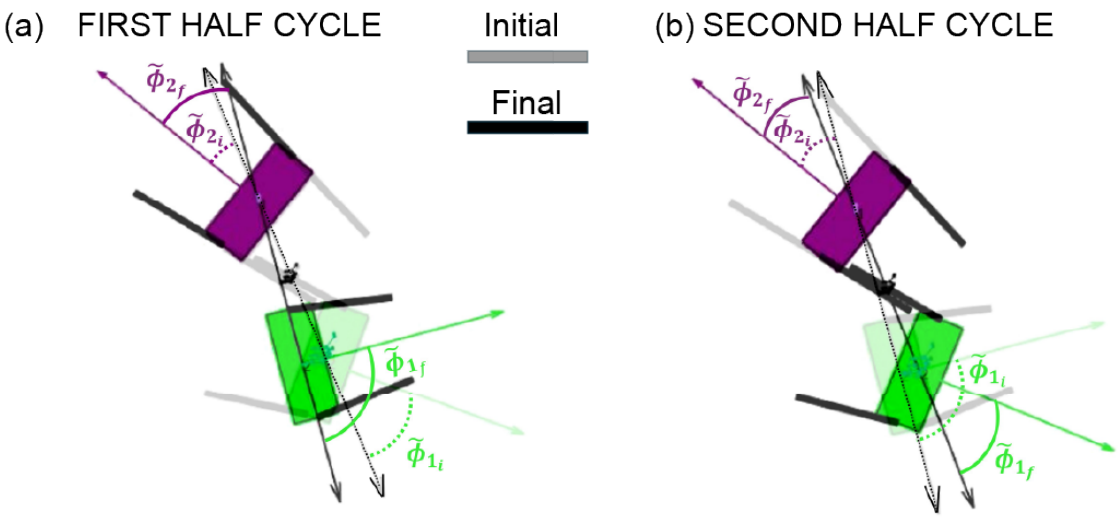

Figure 4.11: The dyad configuration with the individual robots at the beginning and end of the first and second half cycles overlaid on top of each other. Lower transparency indicates the beginning of the half cycle, while darker transparency indicates the end of the half cycle. The angles $\tilde{\phi}_1$ and $\tilde{\phi}_2$ are the supplements of the angles ϕ_1 and ϕ_2 described in Figure 4.2.

the positions of the robots at the beginning and end of these events. The ending position of the robots at the end of the first half cycle serves as the starting position of the robots at the beginning of the second half cycle. These positions are depicted in Figure 4.11.

For the first half cycle this is given by:

$$g_1 = \begin{bmatrix} -\sin(\phi_{1,i}+\theta_{1,i}) & r\cos(\phi_{1,i}+\theta_{1,i}) & r\cos(\phi_{1,i}+\theta_{1,i}) \\ \cos(\phi_{1,i}+\theta_{1,i}) & -r\sin(\phi_{1,i}+\theta_{1,i}) & -r\sin(\phi_{1,i}+\theta_{1,i}) \\ 0 & 1 & 1 \end{bmatrix} \begin{bmatrix} \Delta r \\ \Delta\phi_1 \\ \Delta\theta_1 \end{bmatrix} \tag{4.22}$$

Given that the initial state for second half-cycle corresponds to the final state of the first half-cycle, we write:

$$g_2 = \begin{bmatrix} -\sin(\phi_{1,f}+\theta_{1,f}) & r_f\cos(\phi_{1,f}+\theta_{1,f}) & r_f\cos(\phi_{1,f}+\theta_{1,f}) \\ \cos(\phi_{1,f}+\theta_{1,f}) & -r_f\sin(\phi_{1,f}+\theta_{1,f}) & -r_f\sin(\phi_{1,f}+\theta_{1,f}) \\ 0 & 1 & 1 \end{bmatrix} \begin{bmatrix} \Delta r \\ \Delta\phi_1 \\ \Delta\theta_1 \end{bmatrix} \tag{4.23}$$

Here:

- $\phi_{1,f}$ is the final value of ϕ_1 from the previous half-cycle: $\phi_{1,f} = \phi_{1,i} + \Delta\phi_1$.

- $\theta_{1,f}$ is the final value of θ_1 from the previous half-cycle, where the angular coordinate θ_1 is the leader's absolute orientation with respect to the lab frame and serves as the second angular coordinate in place of ϕ_2, which belonged to the follower, and had the low amplitude oscillation in shape space. This angle serves as a more natural control input to express the effective displacement vectors for the half cycles, the details of which are provided in the SI. $\theta_{1,f} = \theta_{1,i} + \Delta\theta_1$.

- r_f is the final value of r from the previous half-cycle: $r_f = r_i + \Delta r$.

To create a model that takes as input the emergent shape space dynamics (r, ϕ_1, θ_1)—analogous to the drive and steer inputs in vehicle models—and computes the net displacement over a cycle via the Lie bracket of the half-cycle vector fields, we transition to a continuous representation of the vector field g, which maps the influence of shape variables onto the configuration space $q = (x, y, \Theta)$.

$$\vec{g} = \begin{bmatrix} g_x \\ g_y \\ g_\Theta \end{bmatrix} = \begin{bmatrix} -\sin(\phi_1 + \theta_1) & r\cos(\phi_1 + \theta_1) & r\cos(\phi_1 + \theta_1) \\ \cos(\phi_1 + \theta_1) & -r\sin(\phi_1 + \theta_1) & -r\sin(\phi_1 + \theta_1) \\ 0 & 1 & 1 \end{bmatrix} \begin{bmatrix} \dot{r} \\ \dot{\phi}_1 \\ \dot{\theta}_1 \end{bmatrix} \tag{4.24}$$

The time evolution of shape variables in the first half-cycle $t : 0 \to \frac{T}{2}$, and the second half-cycle $t : \frac{T}{2} \to T$ generate the corresponding vector fields. These are parametrized by piecewise continuous equations and described in the SI. In the laboratory frame the configuration evolves as:

$$q_{i+1} = q_i + (g_1 + [g_1, g_2])\,\Delta t \tag{4.25}$$

The Lie bracket acts as a first-order perturbative correction that captures the effective displacement arising from the cyclic evolution of the shape variables. This correction is incorporated through a Lie bracket term, which can be computed for any two vector fields g_1 and g_2 as:

$$[g_1, g_2] = \begin{bmatrix} g_{1y}g_{2\Theta} - g_{2y}g_{1\Theta} \\ g_{1\Theta}g_{2x} - g_{2\Theta}g_{1x} \\ 0 \end{bmatrix} \tag{4.26}$$

We use a simple Euler scheme to forward integrate this difference equation until $t_i = T$ and obtain the trajectory for a cycle $\mathbf{q}(t)$ over $[0, T]$ with the prescribed input shape space and repeat the process for the subsequent cycles using the same base template to obtain the trajectory obtained by the model contrasted with that obtained from the full DEM simulation with the corresponding contribution from the Lie bracket capturing the non-commutative transport along the diagonal direction as shown in Figure B.10.

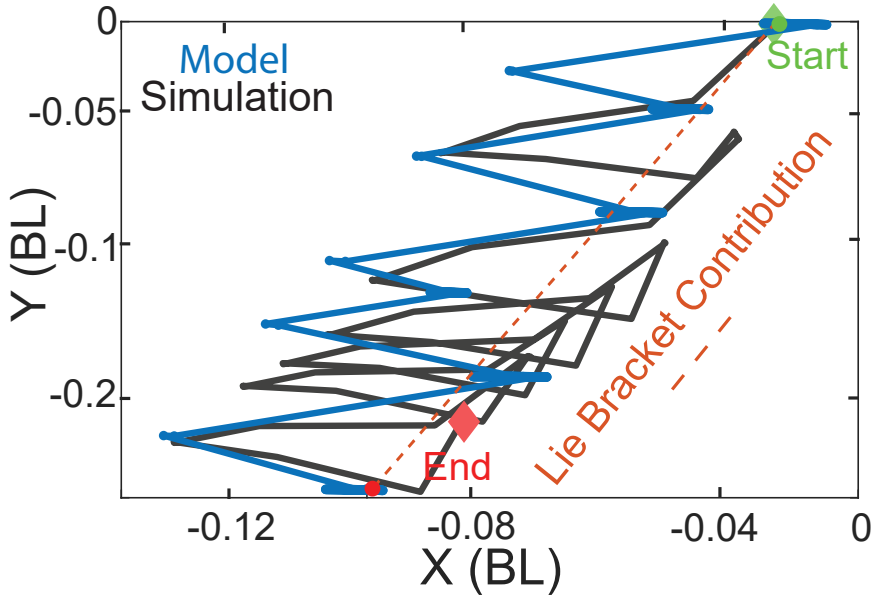

Figure 4.12: Non Commutativity in dyad displacement. The dyad displacement can be approximated by measuring the non-commutativity between half cycle displacements calculated wrt the emergent shape space of these dyads.

4.6 Transition from static bound states to gliders as a function of gait non-reciprocity.

Since the non-reciprocity in the configuration space was encoded in the asymmetry between the movement of the two robot arms, we parametrized it by the difference in their simultaneous opening. Starting with configurations that traced straight-line paths in shape space along the two diagonals of the square gait—where both arms moved simultaneously—we introduced increasing levels of non-reciprocity by varying the difference in simultaneous arm movement, thereby expanding the gaits in area by a fixed opening d shown in Figure 4.13. This parametric variation led to distinct behaviors for the emergent bound states along the two diagonal paths, observed in simulated collectives of compressed robots expanding to a relaxed state, similar to the setting in which the original gliders were discovered. Along the NE-SW diagonal, where robots alternated between U-shaped configurations (i), we observed only the existence of almost anti-symmetric bound states (C1), characterized by sustained periodic contact at deviations from $\phi = 180°$. In contrast, along the NW-SE diagonal, where robots alternated between Z-shaped configurations (ii), we observed both the almost symmetric bound states (C2) deviating from $\phi = 0, 360°$ and the anti-symmetric bound states (C1) [114]. The configurations adopted by the robots along these paths provided a mechanistic explanation for the emergence of self-organized states. Specifically, the steric constraints imposed by U-shaped configurations caused the robots to squeeze against each other, restricting the system to the C1 mode. In contrast, the Z-shaped configurations relaxed these steric constraints, allowing one robot to slide into the free space between the arm and the body, thereby enabling the stabilization of the C2 mode. Both families of gaits ultimately converged to the square gait, which, due to steric constraints discussed in [114], only permitted the C1 mode.

During simulations, we observed that only the bound states emerging at higher levels of gait non-reciprocity exhibited sustained transport. This observation motivated a systematic investigation of the transport properties of the C1 glider—the sterically stable mode

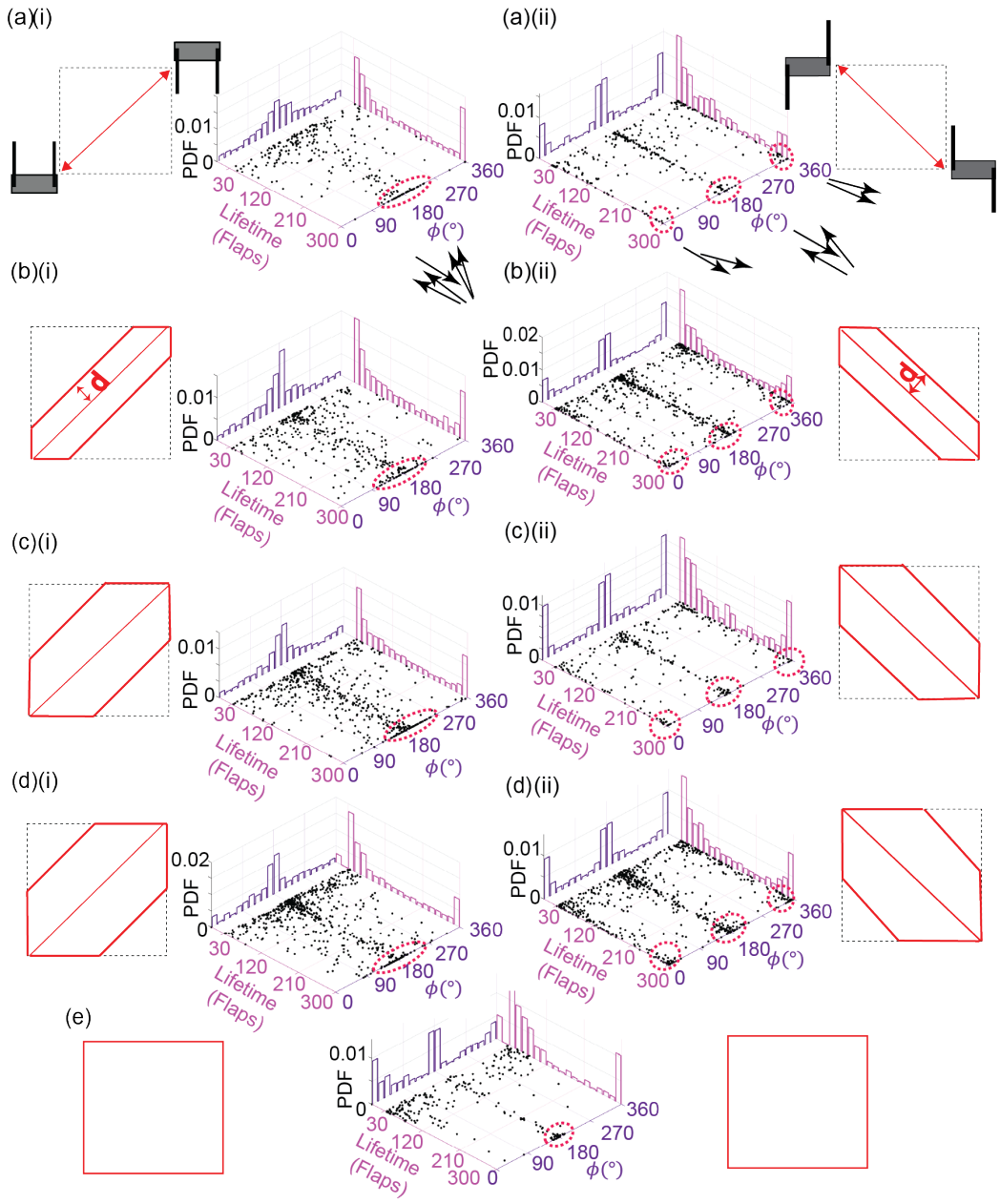

Figure 4.13: Emergent modes for gaits of increasing non-reciprocity (parametrized by area) starting from the two diagonals in the configuration space ending at the square. (a–d) Depict the various gaits that were programmed into the robots starting from the two diagonals of the square and sweeping through gaits of increasing area parametrized by the width d of the hexagonal shapes for intermediate areas, until finally reaching the square (e). The corresponding scatter plot for the lifetime vs. relative angle ϕ along with the respective distributions shown under the gaits reveal that while C1 (anti-parallel) is the only emergent mode for the first (i) family of gaits, both C1 (anti-parallel) and C2 (parallel) modes are stable for the second family of hexagonal gaits (ii), which can be understood from steric constraints.

along both diagonal paths—as a function of gait area. We probed the transition from static bound states to gliding dyads by quantifying their center-of-mass (CoM) displacement in the comoving frame. To characterize this transition, we computed the distributions of CoM displacement per cycle as discussed in Section subsection 4.3.2 and plotted the standard deviation of these distributions for emergent dyads with different gait areas as shown in Figure 4.14. Our results reveal that for small gait areas, the displacement distributions are sharply peaked, resembling delta functions indicative of no transport with the robots only maintaining sustaining periodic contact with each other, whereas for larger gait areas, they broaden into more symmetric shapes indicative of bi-directional (i.e. to left or right) transport as shown in Fig SI (See SM). This qualitative change in behavior appears as a sharp transition in the standard deviation vs. gait area curve, signaling the onset of systematic transport beyond a certain threshold for non-reciprocity. This transition highlights the essential influence of non-reciprocity in maintaining locomotion, distinguishing our robophysical dynamical system from theoretical and numerical models studied thus far [165, 21, 99], where such transitions are more commonly observed .

4.7 Steering Dyads by time reversing the direction of gait traversal

Time-reversal symmetry in this system is defined as the reversal of the gait phase, expressed as $\tau \rightarrow -\tau$, where τ denotes gait time. The direction in which the gait is traversed determines the sequence of arm activation, thereby introducing non-reciprocity in motion. This non-reciprocity imparts a fixed chirality to the dyad configuration, characterized by a repeatable sequence of arm-arm collisions per gait cycle (highlighted in red). The assigned chirality influences both the heading and curvature of the resulting trajectories: dyads of opposite chirality form mirrored configurations and exhibit diverging paths that curve in opposite directions, as illustrated in the CCW and CW ensembles Figure 4.15(a–b).

Building on this relationship, we implemented a minimal feedback control mechanism to dynamically steer the dyads. Specifically, we introduced an *exteroceptive control cue*:

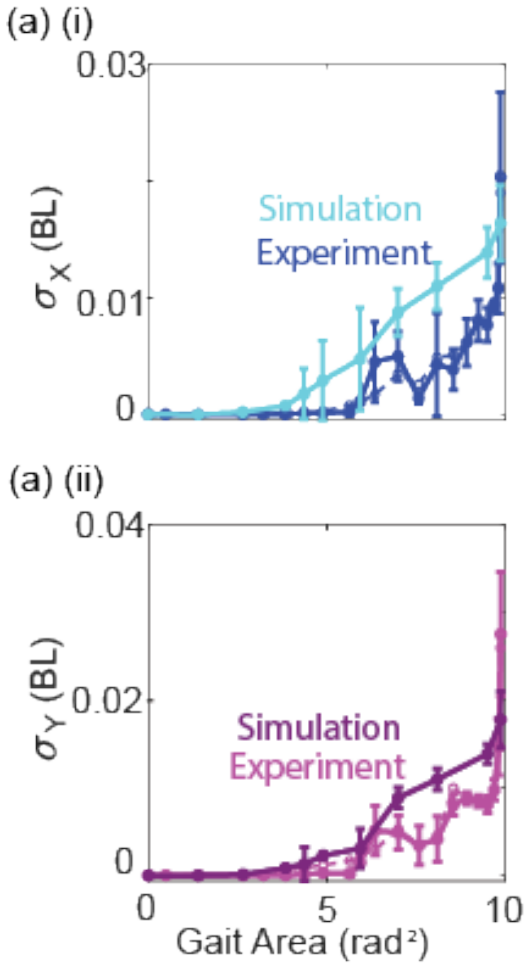

Figure 4.14: Transition from static bound states to C1 type gliders as a function of gait area. a(i-ii) X and Y components of the standard deviation of dyad CoM displacement per period in the co-moving dyad frame as a function of gait area from the Diagonal U to Square path in the configuration space.

an acoustic tone at 1100 Hz, detected via the onboard microphone, triggered a reversal in the direction of gait traversal. This switch effectively flips the chirality of the dyad, thereby reversing both its heading and trajectory curvature in real time.

The effectiveness of this control strategy is shown in Figure 4.15(c), where the center-of-mass (CoM) trajectory of a travelling C1 dyad exhibits a clear point of inflection corresponding to the moment the audio cue was applied. This curvature inversion is quantified in Figure 4.15(d), which plots the instantaneous curvature along the trajectory. This experiment reveals an actionable link between chirality, non-reciprocity, and it's effects on the

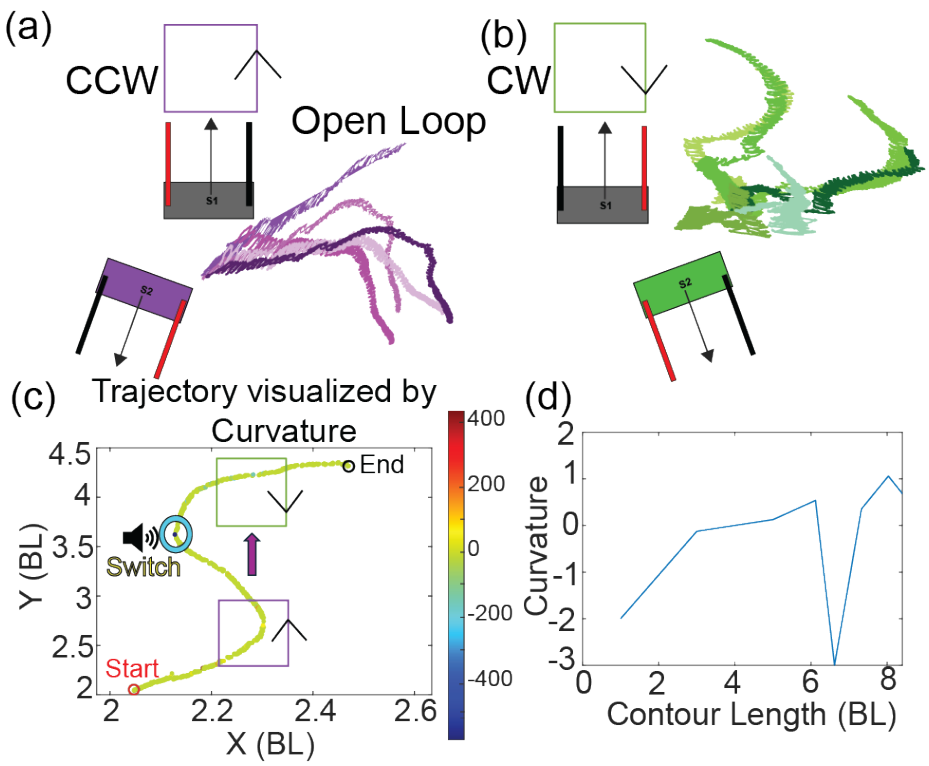

Figure 4.15: Steering the C1 glider by time reversing the gait with audio feedback. (a-b) Ensemble of open loop dyad com trajectories with the square gait executed in CCW v.s. CW direction. The time-irreversibility of the non-reciprocal square gait endows it with a fixed chirality. Dyads of a given chirality are the mirror images of the dyads of the opposite chirality. (c) We can steer a dyad trajectory by changing the gait chirality. We enable a change in gait through an audio signal of a particular frequency detected by the microphone on the robots, which switch the direction of time traversal of the gait from CCW to CW. This change in gait chirality manifests as change in the curvature of the trial as shown in (d).

collective dynamics of self-deforming bodies. By leveraging minimal external feedback, we demonstrate a principle of how these emergent properties can be harnessed and steered in real time—laying the groundwork for precise, task-oriented control strategies in active robotic materials.

4.8 Conclusion

In this work, we have shown how symmetry breaking governs emergent transport in robotic dyads driven by non-reciprocal gaits and interacting via collisional interactions with coulomb

friction. We demonstrate how transport arises through the spontaneous breaking of exchange symmetry, where one robot in the dyad stochastically assumes the role of leader while the other follows. Through simulations and experiments, we uncover how this emergent asymmetry directs motion, and how the trajectory of the dyad reflects the underlying symmetry structure of its configuration space. We rectify and enhance the dyad motion by controllably introducing systematic biases in the gait thus turning this spontaneous symmetry breaking into a controllable mode of transport. Furthermore, we show how the commanded shape space dynamics coupled with overdamped collisional interactions give rise to an emergent non-commutativity in the robot-transport. This behavior can be interpreted as the outcome of coupling two individually self-deforming bodies—each with its own internal gauge structure—through time-ordered collisions. The dyad acts as a composite entity whose effective shape-space dynamics arise from the interplay of two independent gauge potentials—each individually incapable of generating locomotion under isotropic Coulomb friction. Wilczek [166] has suggested that when many deformable bodies will interact, their individual internal gauge structures may couple in such a way that collective behavior arises from space-time gradations of shape. Our robotic dyad serves as a minimal realization of this principle: the impending transport and trajectory curvature arise not from the behavior of either robot alone, but from the gauge-like coupling induced by asymmetric, non-reciprocal interactions during contact which form the steady state attractor in the emergent shape space. Further, the non-reciprocity embedded in the gait manifests as a non-commutativity in the transport of the glider. As these dyads interact with other members of the collective, their geometry and gait-induced chirality enable them to link up with sterically compatible neighbors, assembling into chain-like structures that exhibit long-range orientational order and self-sustained flows. It would be worth charting out the dimensionally reduced attractors representing the space-time gradations of the emergent shape space corresponding to these higher-order self-organized structures and mapping out a rattling landscape [23], to construct a non-equilibrium microstate table; such a represen-

tation would help identify configurations poised near tipping points, where slight manipulations—akin to those demonstrated for the dyads—could extract more complex forms of work from the collective.

We also identify a non-reciprocity–driven transition from static bound states to persistent gliding, akin to phase transitions observed in non-reciprocal field theories and active matter. A natural future direction would be to develop a hydrodynamic description of these shape-changing robotic swarms by coarse-graining the microscopic alignment and transport rules of dyads across the gaits of varying levels of non-reciprocity. Such an approach could help map this system onto analytically tractable models where non-reciprocal phase transitions have been studied [165]. This could, in turn, open the door to performing a linear stability analysis around the observed transition point—an approach that is currently feasible only through numerical exploration. Establishing a coarse-grained, continuum-level theory would provide the analytical framework necessary to identify instabilities, bifurcation structures, and critical behavior associated with the onset of directed motion. Such analysis could help classify the nature of the transition and potentially reveal universal features shared with other non-reciprocal active systems.

Crucially, we leverage the chirality associated with gait traversal direction as a control handle, demonstrating a simple exteroceptive feedback mechanism that reverses trajectory curvature on demand. This provides a robust method for steering these gliders, enabling task-oriented manipulation of emergent transport with a small intervention. Our results position shape changing programmable bodies with non-trivial interactions as a powerful platform for probing symmetry, non-reciprocity, and geometric control in self-organizing robotic systems. These insights strengthen the connections between deformable robotics, non-linear dynamics, and active matter, offering unique strategies to understand and control emergent behaviors in systems where broken symmetries shape the dynamics and can be steered via minimal input.

CHAPTER 5

GAIT-, COLLISION-, AND ADHESION-INDUCED SELF-ORGANIZATION IN DENSE COLLECTIVES OF SMARTICLES

5.1 Summary

The same principles of collisional interactions and gait-template-induced self-organization that govern dynamic binding and transport in dyadic shape-changing robots extend naturally to dense planar collectives. In these systems, robots continuously connect with spatially and temporally available neighbors, forming transient, polymer-like chains that persist across multiple gait cycles before disassembling. The packing density plays a critical role, directly influencing both the average chain length and their lifetimes.

Distinct gait templates give rise to qualitatively different modes of self-organization. Non-reciprocal gaits that trace closed loops in configuration space generate long-range order, producing self-assembled chiral chains with loops that span the entire spatial domain. In contrast, a time-reversible gait that alternates between two U-shaped configurations along the NE–SW diagonal disrupts order, resulting in a fully disordered phase. An alternative time-reversible gait, cycling between Z-shaped configurations along the NW–SE diagonal, induces a self-organized phase of long, nematically aligned chains with a common director.

A constrained robot variant limited to asymmetric, reciprocal deformations also exhibits concavity- and collision-mediated dynamic clustering. Introducing Velcro strips on specific arm faces further enhances adhesion upon contact, significantly amplifying both clustering and transport efficiency.

This chapter presents some results characterizing these diverse self-organizing modes in both simulated and physical collectives of shape-changing robots.

5.2 Pattern formation via gaits in dense collectives of shape changing robots

To investigate the emergence of self-organized patterns in dense robot collectives, we simulated a tightly compressed group of 100 robots at a packing fraction optimized for maximal glider formation, and allowed the system to relax. The resulting dynamics revealed a range of behaviors, dependent on the programmed gait. In addition to the gaits described in section 4.6, we introduced two new figure-eight templates that retain non-reciprocity through asymmetric arm movements. These self-deformation patterns enable robots to align and form loopy structures, giving rise to system-spanning long-range order. Snapshots below (shown for 5 unique gaits) illustrate the relaxation dynamics, with robots participating in self-organization—i.e., in contact with neighbors—highlighted with green lines.

Figure 5.1 illustrates the time evolution of a compressed collective in which all robots execute the time reversible NE–SW diagonal gait, cycling between two U-shaped configurations. Unlike other gaits that allow transient binding through open-arm geometries, these configurations maintain minimal spacing between the arms throughout the gait cycle. This steric hindrance prevents robots from dynamically forming and sustaining inter-robot connections, resulting in a failure to nucleate organized clusters or chains. As a result, the collective remains disordered, lacking any long-range structure in the bulk.

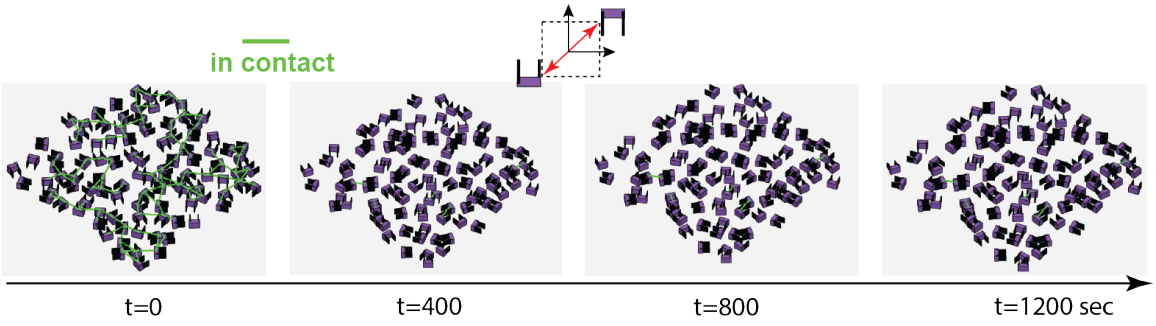

Figure 5.1: Time evolution of compressed robot collectives relaxing while executing the NE–SW diagonal gait, alternating between two U-shaped configurations. This results in a disordered bulk phase.

Figure 5.2 shows the time evolution of a compressed collective of robots executing

the time reversible NW–SE diagonal gait, characterized by a cyclic transition between two Z-shaped configurations. Unlike the U-shaped variants, these Z-configurations preserve open geometries during the gait cycle, leaving space between the robot arms. This spatial allowance enables robots to intercalate between one another, facilitating parallel alignment and sustained interactions. As the collective relaxes, these sterically accessible conformations promote the spontaneous formation of extended, aligned chains of robots. The resulting structures bear a striking resemblance to nematically ordered microtubule filaments, as seen in cytoskeletal self-assembly systems [167]. This alignment-driven phase reflects a robo-physical analog of liquid crystal order, where local interactions—mediated by geometry and gait symmetry—give rise to coherent, system-spanning organization.

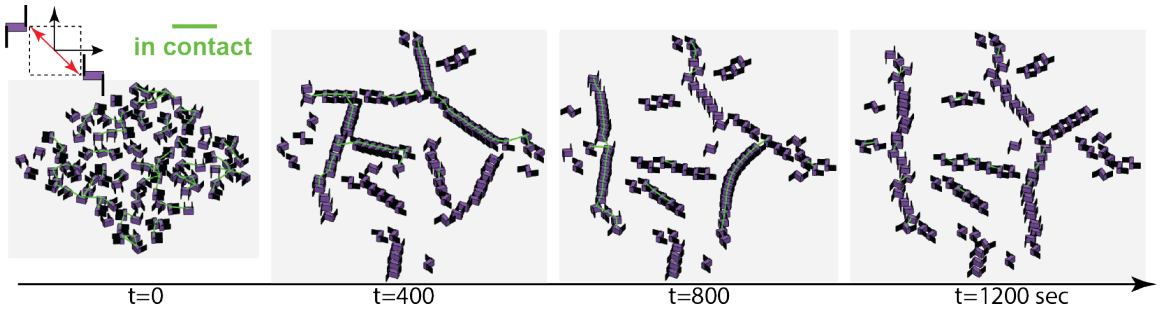

Figure 5.2: Time evolution of compressed robot collectives relaxing while executing the NW–SE diagonal gait, alternating between two Z-shaped configurations. This phase features long, aligned chains reminiscent of nematically ordered microtubule filaments [167].

Figure 5.3 presents the time evolution of a compressed robot collective executing a square gait that cyclically transitions through four discrete, non-reciprocal configurations. This non-reciprocity enables the emergence of two distinct types of gliders—motile dyads exhibiting different internal configurations and lifetimes. Within the bulk of the collective, these gliders dynamically interact, forming intermediate-length chains that are intermittently connected through transient loopy structures. These loop-mediated contacts serve as flexible joints, allowing local reconfiguration and the persistence of a chiral, system-wide order. Meanwhile, gliders at the boundaries often decouple and radiate outward, contributing to an asymmetric relaxation front. The resulting phase is a chiral ordered state with

internal dynamics qualitatively resembling those observed in 2D polymer melts, where transient entanglements and fluctuating loop structures mediate collective organization and mobility [168, 169]. This analogy highlights the role of time-asymmetric self-deformation cycles in driving emergent material-like behavior in active robotic collectives.

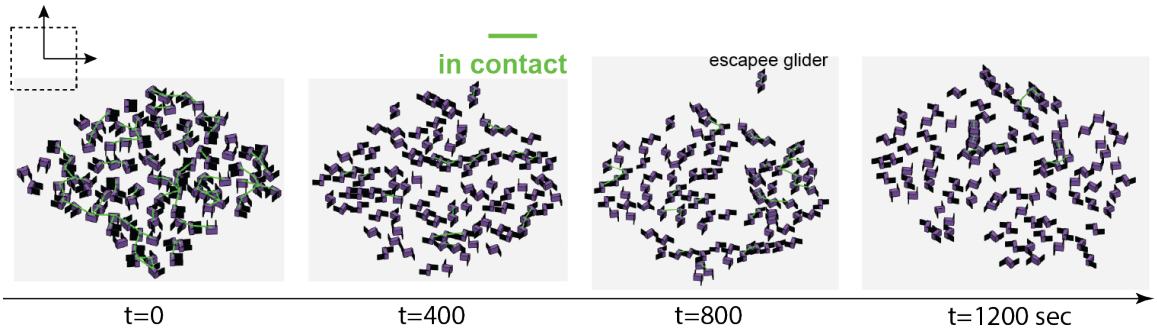

Figure 5.3: Time evolution of compressed robot collectives relaxing while executing a square gait that cyclically alternates between four discrete configurations. The system forms a chiral ordered phase, characterized by short-lived loopy structures formed via dyads and the boundary-driven radiation of gliders.

Figure 5.4 shows the time evolution of compressed robot collectives executing a figure-eight gait, which cycles through diagonally opposed U-shaped configurations. This gait is both non-reciprocal and geometrically permissive: during each cycle, the robots pass through configurations that leave open space between their arms. These transiently accessible geometries enable nearby robots to physically interlock and remain bound for extended periods. As a result, the system supports the formation of long, aligned chains that span significant portions of the domain, while also giving rise to chiral loops mediated by short-lived dyads. The dual presence of bound, extended chains and transient loopy motifs gives rise to a chiral ordered phase that combines both coherence and flexibility. Over time, these structures coalesce into system-spanning long-range order, reflecting an emergent symmetry-breaking organization that parallels ordering transitions in non-equilibrium active matter systems. The interplay of geometric openness, temporal asymmetry, and inter-robot coupling in this gait highlights how internal shape cycles govern phase behavior at the collective scale.

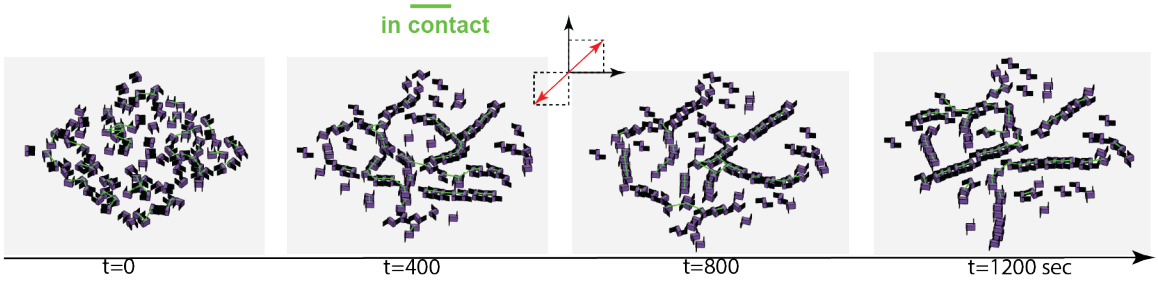

Figure 5.4: Time evolution of compressed robot collectives relaxing while executing a figure-eight gait, cycling between diagonally opposed U-shaped configurations. The system forms a chiral ordered phase characterized by transient loopy motifs and aligned structures that coalesce into long-range order spanning the entire domain.

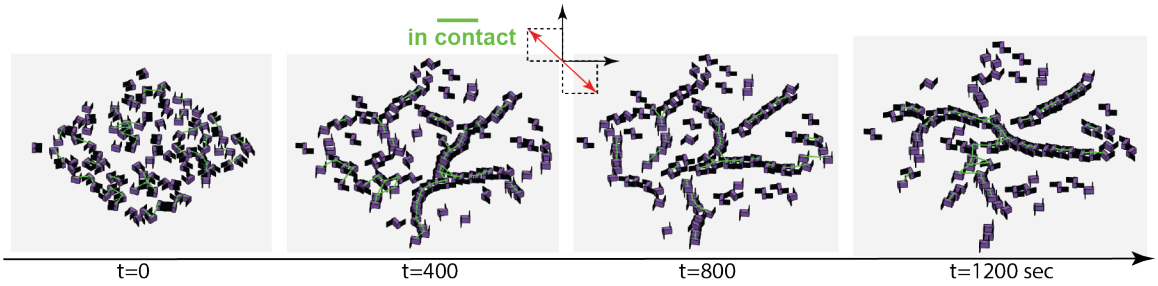

Figure 5.5: Time evolution of compressed robot collectives relaxing while executing a figure-eight gait that cycles between diagonally opposed Z-shaped configurations. The system exhibits a chiral ordered phase, marked by transient loopy structures and the emergence of long-range order spanning the entire domain.

Finally, Figure 5.5 shows the time evolution of a compressed robot collective executing a figure-eight gait that cycles between diagonally opposed Z-shaped configurations. Like its U-shaped counterpart (Figure 5.4), this gait is non-reciprocal and momentarily creates open geometries between the arms, enabling robots to interlock and remain bound for extended durations. The Z-shaped configurations, however, offer enhanced steric compatibility for parallel alignment, promoting the formation of long, chain-like structures interspersed with transient loops. These loopy motifs emerge from short-lived dyads and dynamically link aligned segments, driving the system into a chiral ordered phase with domain-spanning long-range coherence. The result is a robust yet flexible collective architecture shaped by asymmetric actuation and geometry-enabled binding.

5.3 Characterizing self-organization using contact graphs

In our simulations, we can track the full contact history of each robot in the collective, enabling a detailed reconstruction of when and where interactions occur. By focusing on robots that maintain persistent contact with one another over the course of an entire gait cycle, we construct an undirected contact graph that captures the underlying structure of physical connectivity within the system. Each robot is treated as a node, positioned according to its spatial coordinates, and an edge is formed between two nodes if the corresponding robots remained in contact throughout the gait cycle. This method offers a principled way to translate local, short-range physical interactions into a coarse-grained network representation of the system's global organization.

Figure 5.6 shows a representative snapshot of this contact graph taken at Period 11, during the relaxation of a 100-robot collective executing the square gait. The node colors encode degree — the number of other robots a given robot maintained contact with — and serve as a proxy for local density. The ability to monitor this undirected contact graph over time provides valuable insight into the dynamics of self-organization. Specifically, the evolution of the graph's degree distribution reveals changes in local coordination and collective connectivity: a tighter degree distribution may indicate more uniform local packing, while broader distributions suggest heterogeneity in neighborhood size and multifarious levels of self organization. Figure 5.11 shows the corresponding distribution from the contact graph for the same square gait later on in the run.

By examining how the structure of this contact graph changes over time, we can characterize the relaxation behavior of the system as it relaxes toward a steady state. Moreover, because this framework is explicitly tied to persistent physical contact, it reflects the underlying constraints imposed by the gait — different gait cycles induce different patterns of repeated contact and hence different topological evolutions of the graph. This approach thus provides a natural bridge between microscopic actuation dynamics and macroscopic

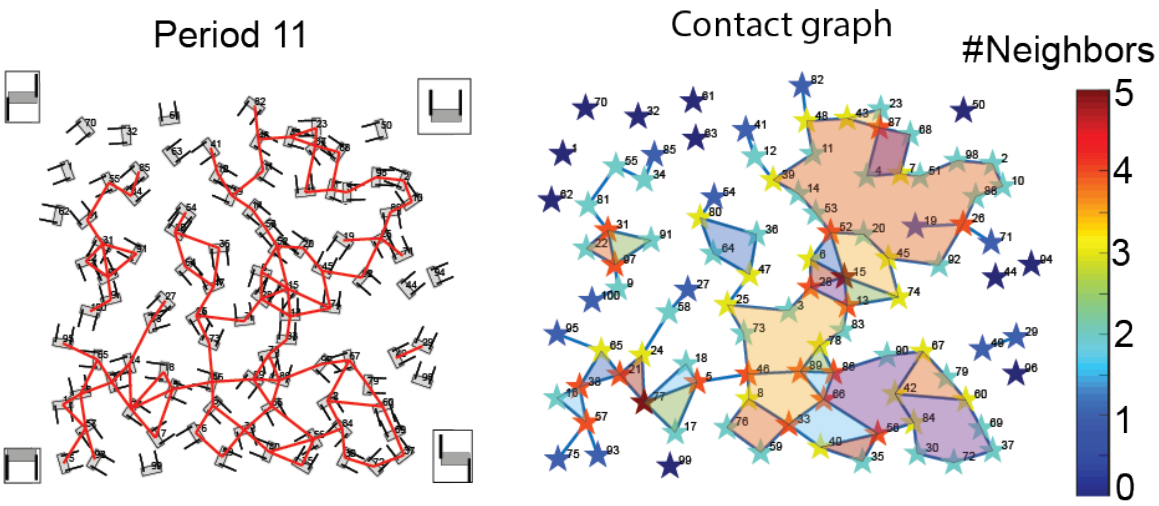

Figure 5.6: Top view of a 100-robot collective executing the square gait at period 11, with its corresponding contact graph constructed by tagging robots that maintained physical contact throughout the gait cycle. The network reveals both tree-like and cyclic connectivity patterns, reflecting the emergent self-organization during relaxation.

emergent behaviors, making it a useful tool for probing gait-dependent self-organization in shape-changing robotic collectives.

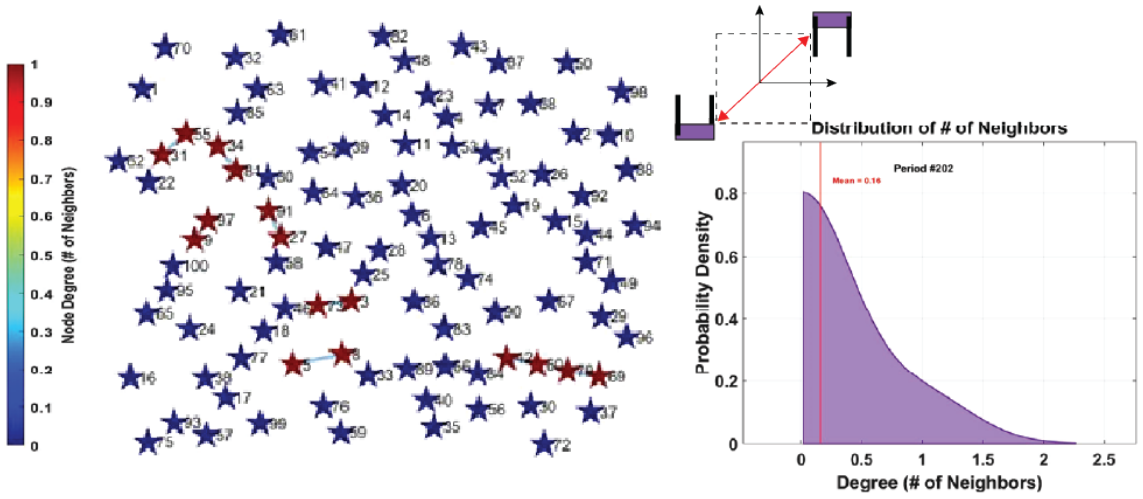

Figure 5.7: Snapshot of the contact graph for the NW-SE diagonal gait collective alongside its degree distribution, quantifying the number of persistent neighbors per robot.

As shown in Figure 5.7 and Figure 5.8, the NW–SE diagonal gait results in a sparsely connected and dynamically disordered collective. The reciprocal alternation between two U-shaped configurations leaves no room between the arms for the collisions responsible

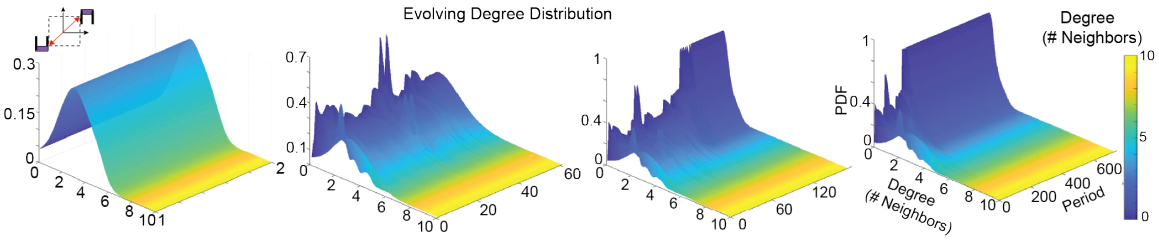

Figure 5.8: The time evolution of the degree distribution for the collective executing the NW-SE diagonal gait converges to a stationary distribution with 0 neighbors depicting the disordered phase in the bulk.

for dynamic binding, thereby disrupting the formation of persistent contacts. This steric limitation inhibits dynamic self-organization in the bulk, driving the degree distribution toward zero and leading to a disordered phase dominated by isolated robots.

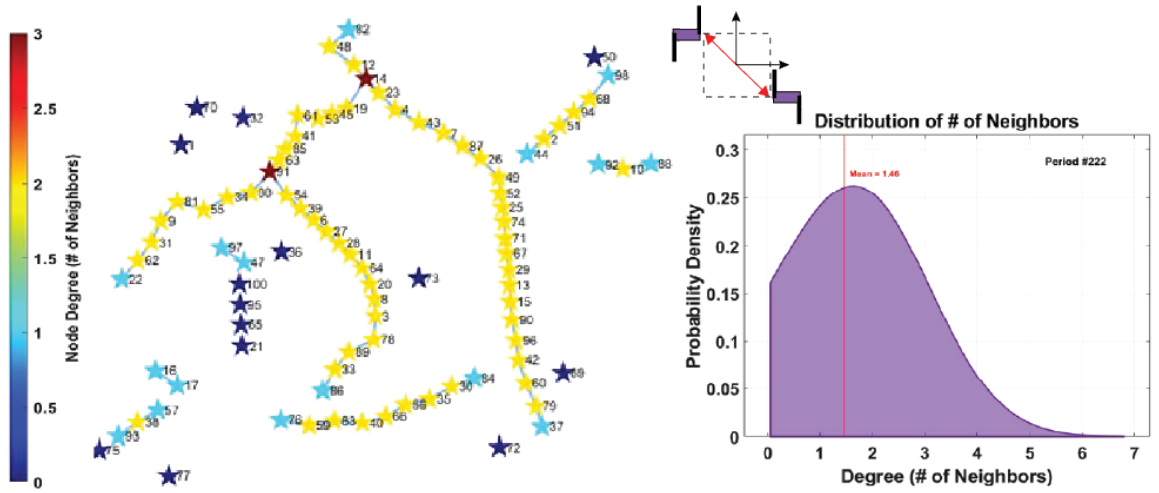

Figure 5.9: Snapshot of the contact graph for the NE-SW diagonal gait collective alongside its degree distribution, quantifying the number of persistent neighbors per robot.

Figure 5.9 and Figure 5.10 characterize the spatial and temporal contact network structure of the NE–SW diagonal gait. Figure 5.9 shows a representative snapshot of the contact graph and corresponding degree distribution, highlighting a peak around degree 2. This reflects a bulk topology dominated by robots maintaining persistent contact with neighbors ahead and behind—forming chain-like configurations. Figure 5.10 captures the time-evolving degree distribution for this gait, showing the persistence of this peak at degree 2 across periods, with occasional transient spikes at higher degrees. These brief excursions

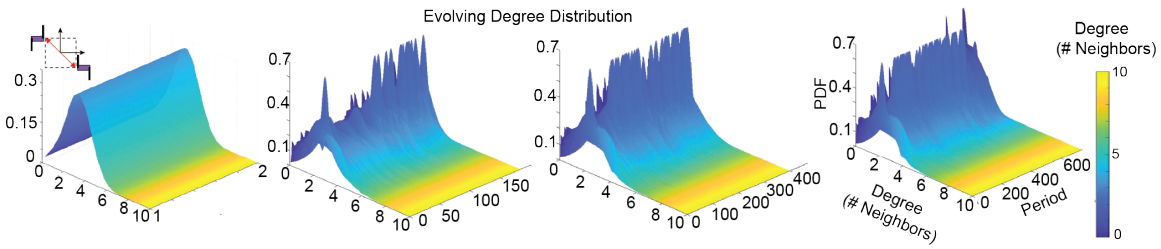

Figure 5.10: The time-evolving degree distribution for the NE–SW diagonal gait exhibits a persistent peak at degree 2, indicative of chain-like bulk structures where robots connect to neighbors ahead and behind, with occasional transient peaks at other degrees indicative of branching behaviors.

correspond to branching events or short-lived clusters that momentarily reorganize linear chains by engulfing new members. In contrast to the NW–SE gait, the NE–SW gait facilitates dynamic binding due to the open space available between the body and alternating arms in the Z configuration, enabling self-organized alignment through robots sliding past each other.

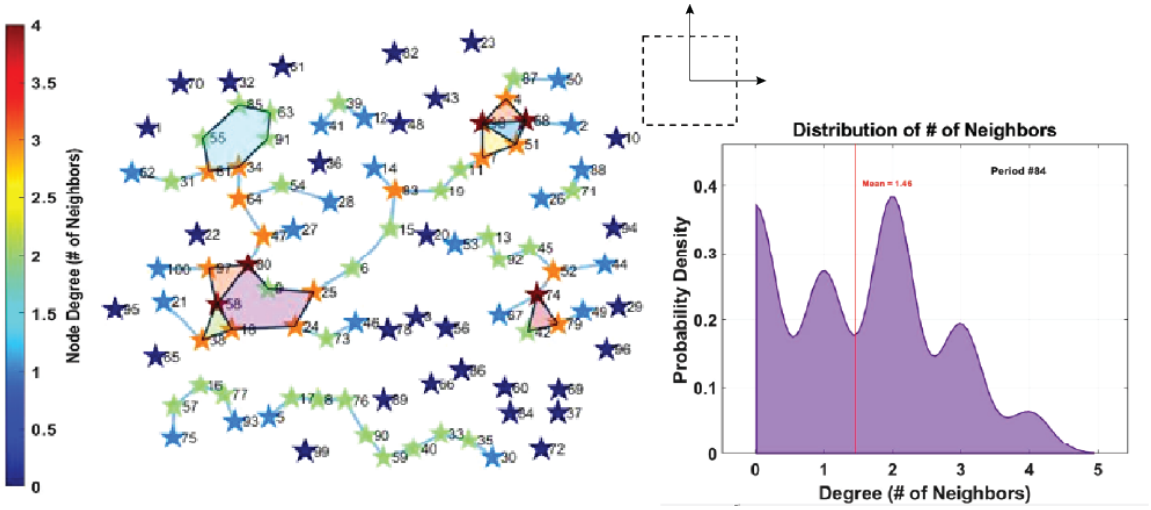

Figure 5.11: Snapshot of the contact graph for the square gait being executed with CCW handedness collective alongside its degree distribution, quantifying the number of persistent neighbors per robot.

Figure 5.11 and Figure 5.12 provide insight into the spatial organization and temporal evolution of contact structures in the collective executing the square gait with counterclockwise handedness. As shown in Figure 5.11, the contact graph snapshot reveals a highly heterogeneous structure, with robots exhibiting a broad range of degrees. The correspond-

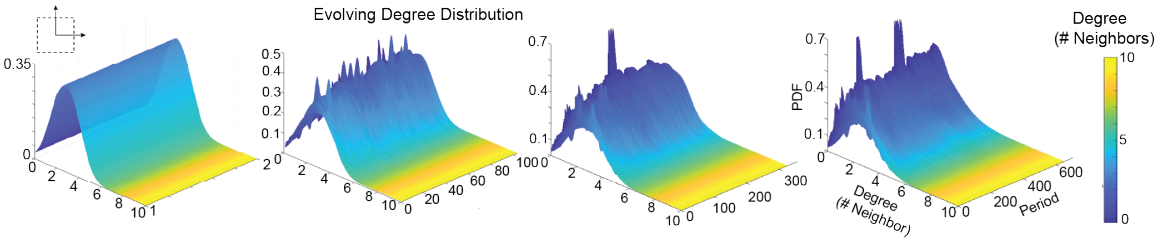

Figure 5.12: The degree distribution over time for the square gait displays multiple peaks between degrees 1 and 5, with intermittent sharp spikes at degree 2—reflecting a bulk composed of short chains, closed loops, and gliders radiating from the boundaries.

ing degree distribution displays multiple peaks, particularly around degrees 1, 2, and 4, indicating the coexistence of different local arrangements. Figure 5.12 captures the time evolution of this distribution, revealing persistent variability and intermittent sharp spikes at degree 2. These spikes are indicative of chain-like motifs, while broader peaks reflect the presence of short cycles and glider structures radiating outward from the bulk. In contrast to the diagonal gaits, the square gait promotes a diverse mix of interactions, supporting transient local order without settling into a steady state for a long period of time.

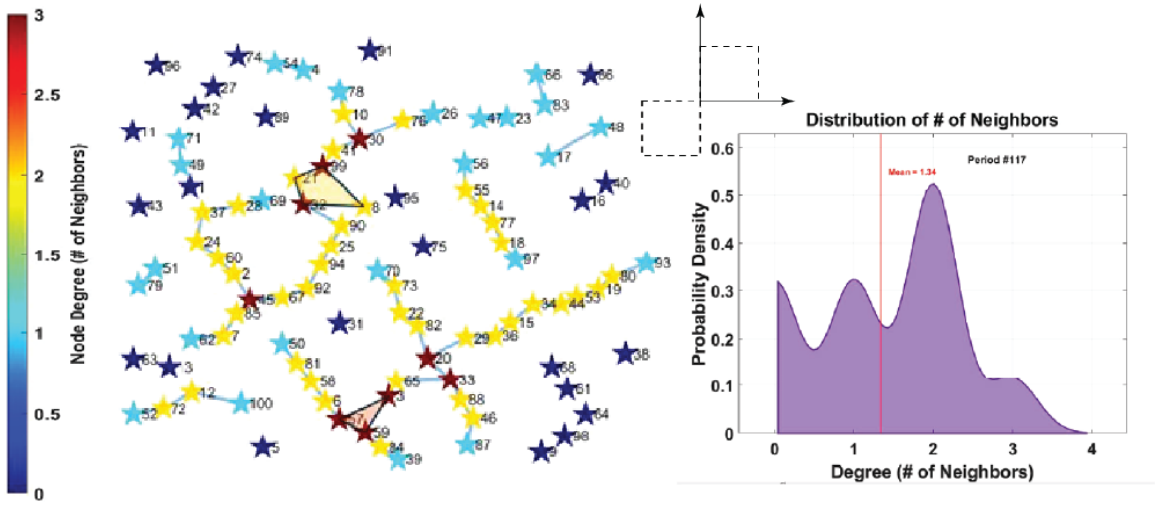

Figure 5.13: Snapshot of the contact graph for the figure of eight gait 1 being executed with CCW handedness collective alongside its degree distribution, quantifying the number of persistent neighbors per robot.

Figure 5.13 through Figure 5.16 present the spatial and temporal contact dynamics for the two figure-eight gait templates executed with counterclockwise handedness. Fig-

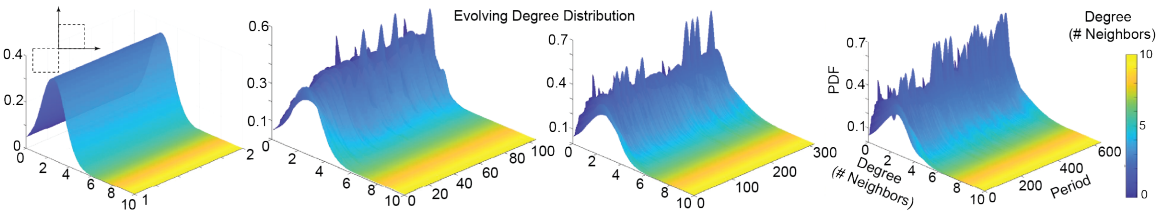

Figure 5.14: The evolving degree distribution for the symmetric figure-eight gait along the two diagonal U configurations shows persistent peaks at degrees 1 and 2, with sporadic spikes at higher degrees—reflecting a bulk of long chains interspersed with cycles and leaf nodes.

ure 5.13 and Figure 5.14 correspond to the diagonal U configuration, where the contact graph reveals extended chains with embedded cycles and terminal leaf nodes. The associated degree distribution exhibits persistent peaks at degrees 1 and 2, with intermittent spikes at higher degrees—reflecting a bulk composed of long chains interspersed with branching structures. Figure 5.15 and Figure 5.16 depict the Z configuration variant, which gives rise to qualitatively similar features. The time-evolving degree distribution reveals comparable peaks and temporal fluctuations, suggesting that both configurations support dynamic self-organization through chain formation and localized network motifs.

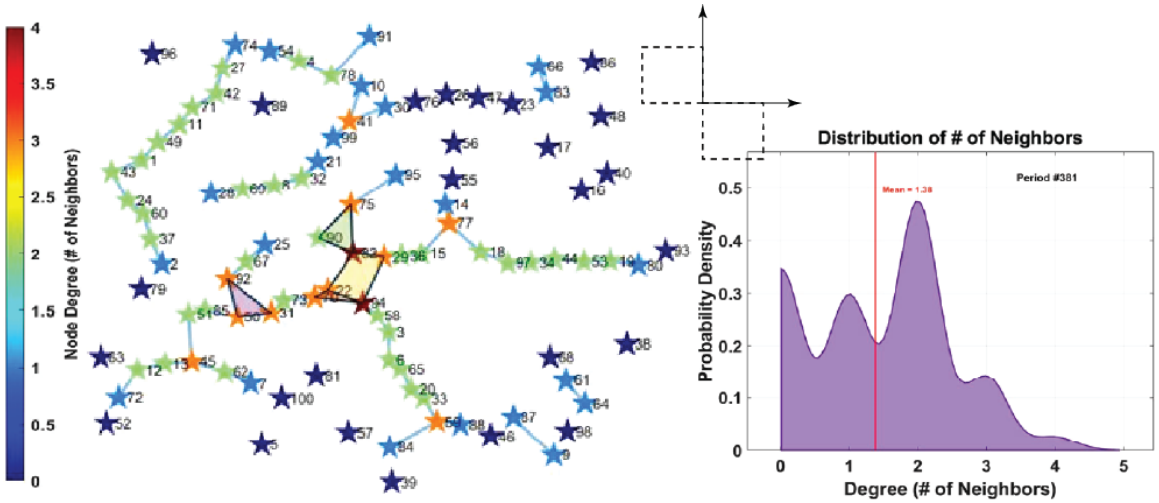

Figure 5.15: Snapshot of the contact graph for the figure of eight gait 2 being executed with CCW handedness collective alongside its degree distribution, quantifying the number of persistent neighbors per robot.

Figure 5.17 consolidates the relationship between gait symmetry and the emergence of

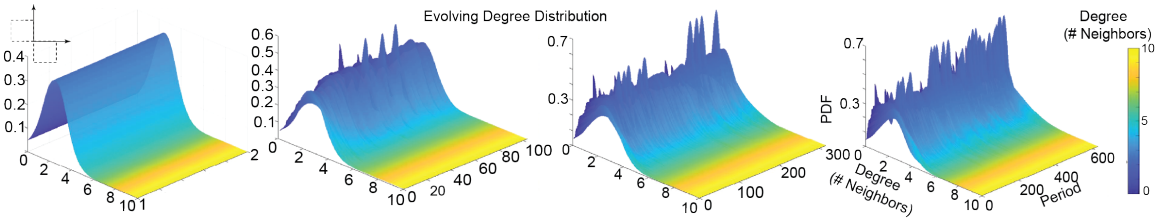

Figure 5.16: The time-evolving degree distribution for the symmetric figure-eight gait along the two diagonal Z configurations reveals a bulk structure qualitatively similar to that of the diagonal U configuration variant.

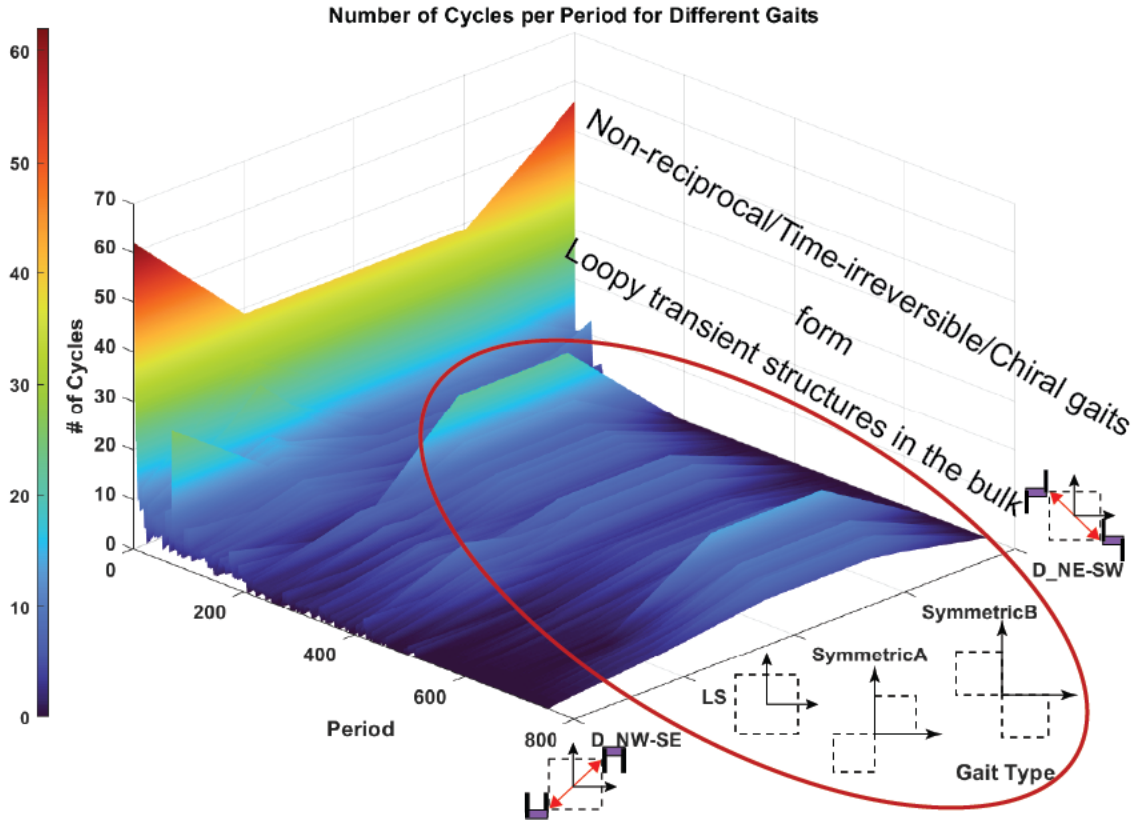

Figure 5.17: Tracking the time evolution of cycle count in the bulk across different gaits reveals that the emergence of loopy structures is predominantly induced by non-reciprocal actuation.

structural motifs in the bulk by tracking the time evolution of cycle count across different gaits. A clear trend emerges: non-reciprocal, time-irreversible gaits—such as the square and figure-eight variants—consistently induce higher cycle counts over time, indicative of the formation of transient loopy structures within the collective. In contrast, symmetric and reciprocal gaits stabilize with fewer or no cycles, corresponding to chain-like or disordered

bulk configurations. These findings suggest that non-reciprocity in actuation manifests as closed loopy structures in the macro scale, thereby enriching the topological complexity of the emergent contact network and thus the bulk.

5.4 Cloud relaxation experiments conducted on collectives featuring a modified robot morphology and actuation scheme

Our collaborators at Cornell designed a new generation of smart active matter modules that enable robust 3D entanglement and are optimized for large-scale fabrication and deployment by a broad spectrum of scientific users. A recent study by [170] demonstrates the broad functional capabilities and simple sensing abilities of this platform. This design emphasizes the advantages of entangled architectures over conventional rigid or lattice-based assemblies commonly found in active matter and modular robotics. Key features include a compact and lightweight form factor, affordability, user-friendly operation, and a low barrier to adoption across disciplines. Smarticle 2.0 features an optimized aspect ratio (length-to-width between 0.4 and 0.75), critical for achieving robust 3D entanglement [170]. Each module transitions between "I" and "U" shapes using a non-backdrivable crank-slider mechanism powered by a dual-threaded worm gear, which converts rotary to linear motion through opposing gear racks. While this architecture is essential for defining the module's structure, weight, and cost *it constrains actuation to be reciprocal, allowing for only one asymmetric gait pattern*. Modules integrate multimodal sensing and communication—optical, acoustic, and mechanical—and are powered by a 180mAh 3.7V LiPo battery, enabling up to 200 actuation cycles. Cost per module (in a batch of 15) includes $22.10 for the PCB, $25.53 for components, $14.99 for the motor, and $6.49 for the battery, with negligible cost for 3D-printed parts.

When experimental collectives of these smarticles were allowed to relax from a compressed initial configuration—similar to those described in Section section 5.2—we continued to observe transient chain-like structures with branching (tree) and cyclic motifs. How-

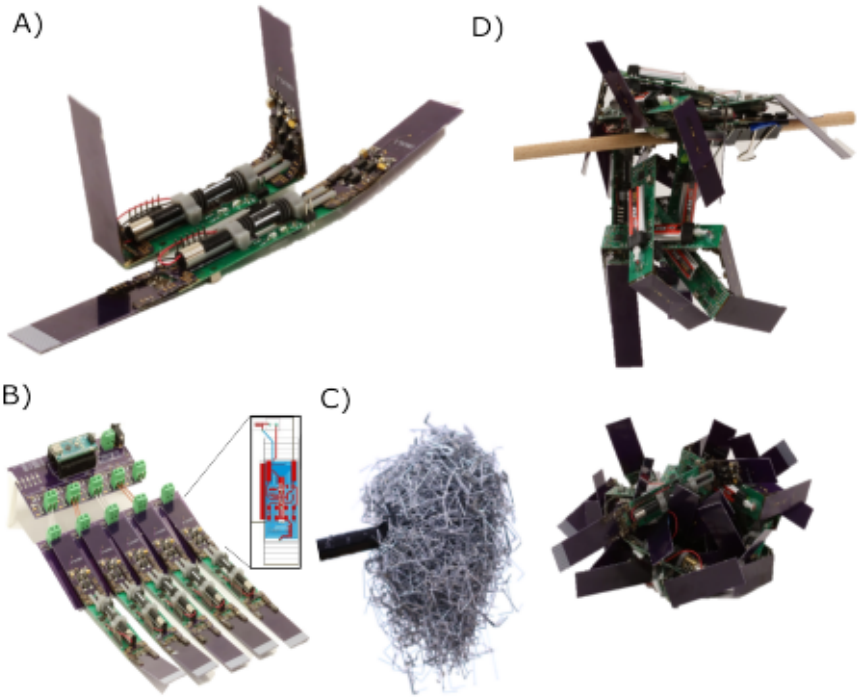

Figure 5.18: Smarticle 2.0 modules transitioning between I and U shaped configurations and entangling to form a cohesive structure like staple piles, adapted from [170].

ever, due to the uniform vertical height of all three links, individual robots were also capable of limited self-transport. Additionally, the crank-slider actuation scheme introduced a slight asymmetry in mass distribution, imparting directional drift in certain configurations. These sources of stochasticity were sufficient to destabilize chains, which typically disintegrated rapidly.

To mitigate this, a simple yet effective mechanical solution was introduced: alternating M and F sides of Velcro tape affixed to robot surfaces. This modification significantly improved the formation of mechanically interlocked structures, enabling robots to adhere in diverse configurations. Notably, these Velcro-induced clumps also exhibited enhanced collective transport compared to unmodified robots.

The following subsections provide an analysis of the transport properties and chaining behavior observed in these experiments. We also present preliminary efforts to simulate the behavior of Velcro-equipped three-link robots. Notably, the spontaneous adhesion ob-

served experimentally proved difficult to replicate in silico; an approximate approach was implemented by introducing weld-joint constraints between adhering faces based on empirical observations. Early results from a micro-state enumeration of chain configurations up to N=5 robots are discussed in the final subsection of this thesis.

5.4.1 Transport properties of collectives with and without Velcro

To promote selective adhesion and mechanically induced clustering within the collective, we affixed M and F Velcro strips to alternating arms of the robots. This asymmetric patterning ensured that adhesion would occur preferentially between complementary surfaces, thereby reducing spurious sticking and favoring structured interactions. The result was the emergence of small clusters of robots that remained mechanically linked for extended periods. These clusters exhibited coherent transport, effectively acting as composite motile units. Figure 5.19 contrasts representative snapshots from two experimental trials—one without and one with Velcro strips—clearly illustrating the formation and locomotion of a physically adhered clumps in the Velcro-enabled case.

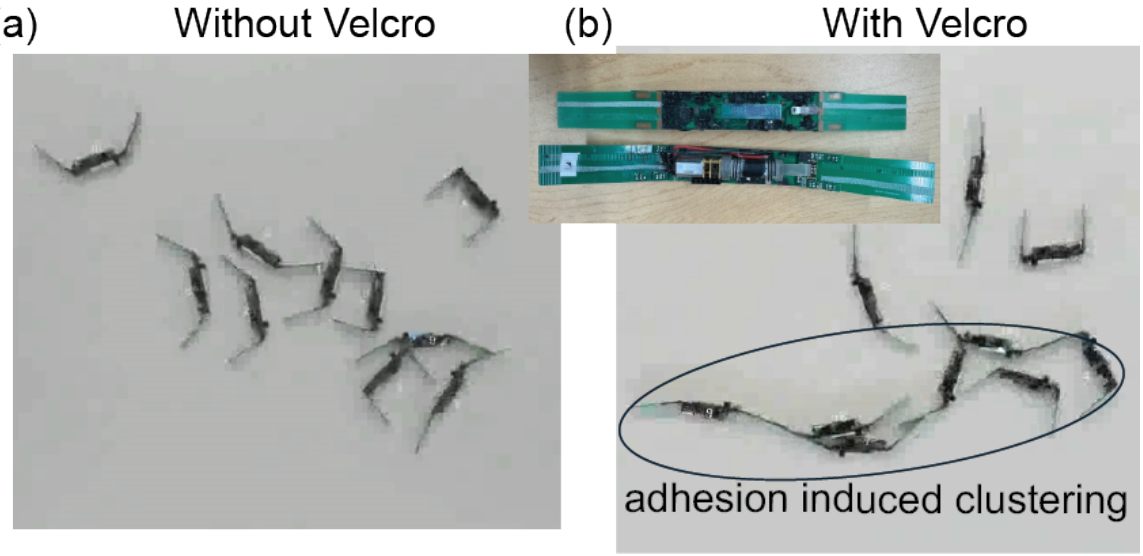

Figure 5.19: Snapshots from smarticle collective relaxation experiments without and with Velcro strips mounted on the arms. Velcro based adhesion promotes local clumping of robots.

These physically adhered clusters also exhibit enhanced transport dynamics, arising from multiple sources of asymmetry in both their topology and actuation. The physical configuration of the clumps introduces geometric asymmetries that bias their direction of motion, while the coordinated actuation of bonded robots amplifies net displacement over time. Figure 5.20 presents the ensemble of trajectories from multiple trials in the absence of Velcro, highlighting a broader spatial spread and reduced coherence. The corresponding mean squared displacement (MSD) versus delay time curves extracted from these trajectories further quantify the differences in transport efficiency, revealing slower and more diffusive dynamics in the non-adhering case.

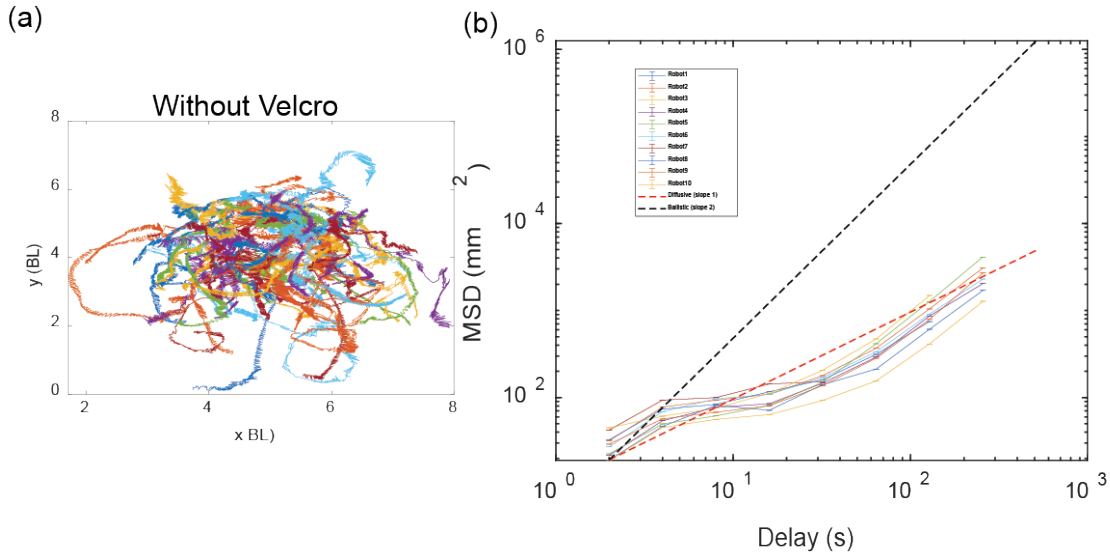

Figure 5.20: Trajectories (a) of individual robots from the collective over multiple trials. MSD v.s. delay (b) for the robot trajectories from the ensemble.

Figure 5.21 shows the corresponding spread of trajectories and mean squared displacement (MSD) versus delay time plots for the Velcro-enabled ensemble. In contrast to the non-adhering case, the robots in this configuration exhibit pronounced directional drift and increased net displacement. The enhanced transport is a direct consequence of Velcro-induced adhesion, which facilitates persistent physical coupling and coordinated motion among robots. The MSD curves reveal that, on average, the robots in the Velcro ensemble move in a super-diffusive regime, indicating sustained directed transport driven by collec-

tive asymmetry and mechanical entanglement.

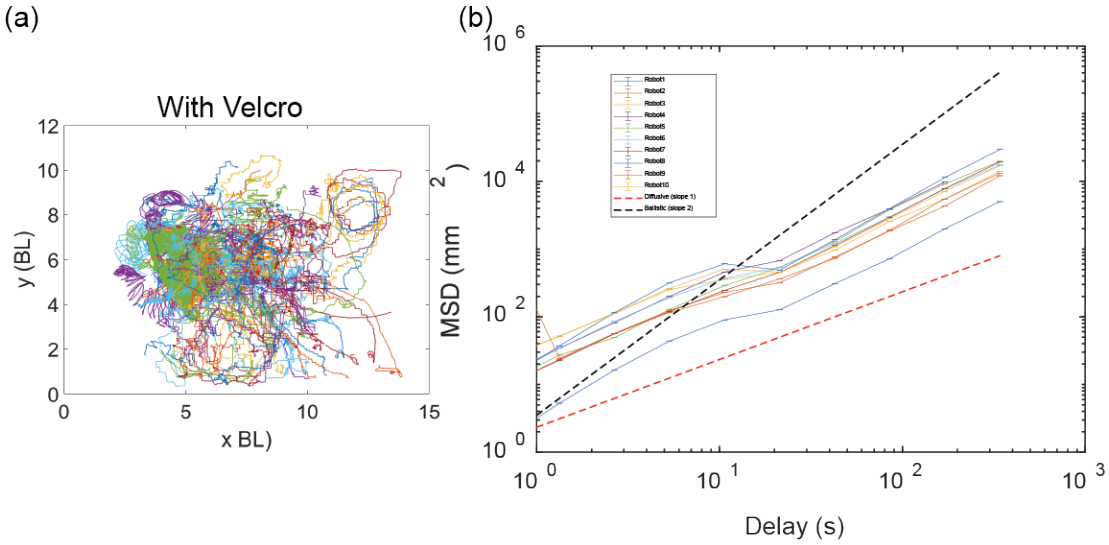

Figure 5.21: Trajectories (a) of individual robots from the collective over multiple trials. MSD v.s. delay (b) for the robot trajectories from the ensemble.

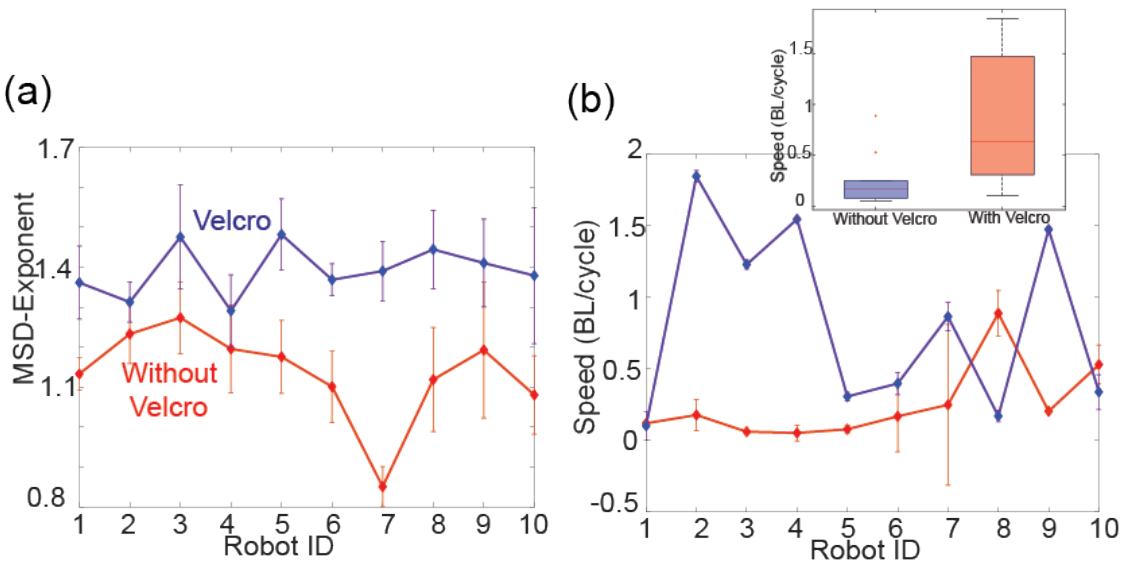

Figure 5.22: MSD exponents (a) for individual robots extracted from the slope of the MSD vs delay curve and speed (b) extracted from the intercept for collectives with and without velcro.

Figure 5.22 summarizes the transport properties of the two ensembles—without and with Velcro—providing a direct comparison of their mobility characteristics. For each robot, the MSD exponent and drift speed are extracted from the slope and intercept, re-

spectively, of the log-log plot of MSD versus delay time. The ensemble equipped with Velcro strips exhibits consistently higher MSD exponents, indicating a transition from super-diffusive to near-ballistic motion, alongside elevated drift speeds. These findings highlight the role of Velcro-induced adhesion in enhancing directional persistence and enabling more effective collective transport.

5.4.2 Analysis of Chaining Events in Velcro-Adhering Robot Collectives

Unlike the simulations experimental data didn't bear any clear signature of contact mediated interactions and hence we couldn't employ the methodology described in the previous section to analyze these experiments. To identify chaining events within a dense collective of robots interacting through stochastic collisions and intermittent Velcro adhesion, we developed a robust computational pipeline centered on velocity correlations, directional alignment, and inter-robot proximity. The pipeline enables the extraction of time-resolved binding events and chain configurations by filtering correlated motion based on mechanical and behavioral constraints.

1. Velocity Correlation-Based Filtering

We first enumerate all distinct robot pairs (R_i, R_j) such that $i \neq j$, for $i, j \in \{1, 2, \ldots, n\}$. A dynamic speed threshold is computed based on the average of the minimum speeds over time:

$$\text{speed\_threshold} = \frac{1}{n} \sum_{i=1}^{n} \min\left(\text{speed}_i(t)\right) \tag{5.1}$$

A binary mask is then applied to identify robots that exceed this threshold:

$$\text{mask}(t, R) = \begin{cases} 1 & \text{if speed}(t, R) > \text{speed\_threshold} \\ 0 & \text{otherwise} \end{cases} \tag{5.2}$$

Next, the velocity correlation between pairs of robots is calculated using the dot product of their unit velocity vectors:

$$\text{vel\_correlation}(t, i, j) = \hat{v}_{x,i}(t)\hat{v}_{x,j}(t) + \hat{v}_{y,i}(t)\hat{v}_{y,j}(t) \tag{5.3}$$

This is then filtered by applying the mask:

$$\text{vel\_correlation}(t, i, j) = \text{vel\_correlation}(t, i, j) \cdot \text{mask}(t, i) \cdot \text{mask}(t, j) \tag{5.4}$$

We retain only positive correlations:

$$\text{vel\_correlation}(t, i, j) = \begin{cases} \text{vel\_correlation}(t, i, j) & \text{if vel\_correlation}(t, i, j) > 0 \\ 0 & \text{otherwise} \end{cases} \tag{5.5}$$

Finally, we smooth the velocity correlation signal in time:

$$\text{smoothed\_vel\_correlation}(t, i, j) = \frac{1}{n} \sum_{n=t-k/2}^{t+k/2} \text{vel\_correlation}(n, i, j) \tag{5.6}$$

2. Directional Filtering via Pairwise Angular Alignment

We compute the instantaneous angle between the direction vectors:

$$\theta_{i,j}(t) = \tan^{-1}\left(\frac{\|\hat{v}_i(t) \times \hat{v}_j(t)\|}{\hat{v}_i(t) \cdot \hat{v}_j(t)}\right) \tag{5.7}$$

The time-averaged alignment is:

$$\bar{\theta}_{i,j} = \frac{1}{T} \sum_{t \in T} \theta_{i,j}(t) \tag{5.8}$$

To reduce redundancy, we only consider upper triangular pairs:

$$\text{mask\_pairwise\_angles} = \begin{cases} \bar{\theta}_{i,j} & \text{if } i < j \\ \text{NaN} & \text{otherwise} \end{cases} \tag{5.9}$$

We then compute a directional alignment score:

$$\cos \bar{\theta}_{i,j} \tag{5.10}$$

3. Chaining Event Definition

A binding or chaining event between robots i and j is defined at time t if:

$$\begin{aligned} \text{binding\_event}(t,i,j) = \; & \big(\text{smoothed\_vel\_correlation}(t,i,j) > \text{Factor} \cdot \cos \bar{\theta}_{i,j}\big) \\ & \wedge \left(\text{distance}_{i,j}(t) \leq \text{Threshold}\right) \end{aligned} \tag{5.11}$$

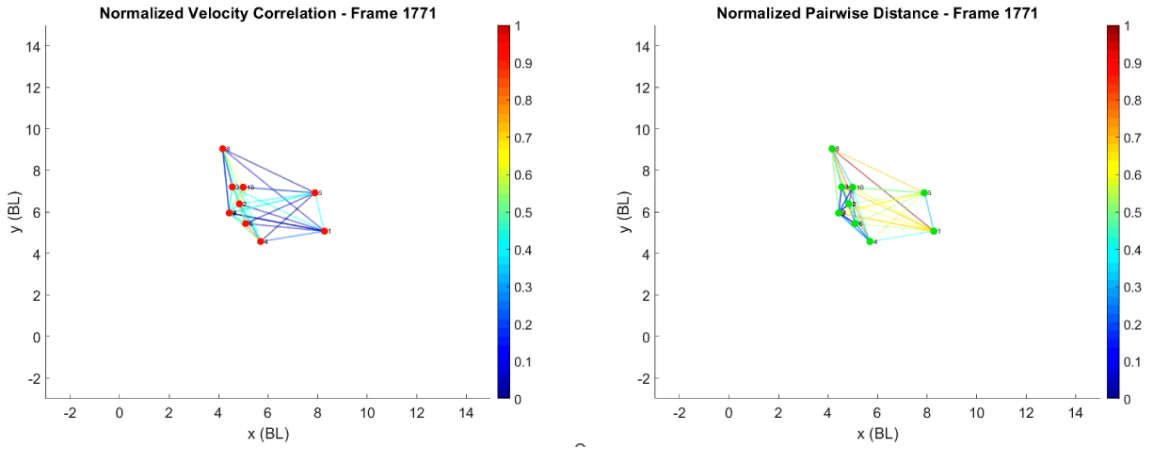

Figure 5.23: Simultaneously filtering graphs based on velocity correlation and pairwise distance.

4. Post-processing

A time-evolving interaction graph is constructed from the binding event map, where each edge represents a detected bond between a pair of robots. The degree distribution of this

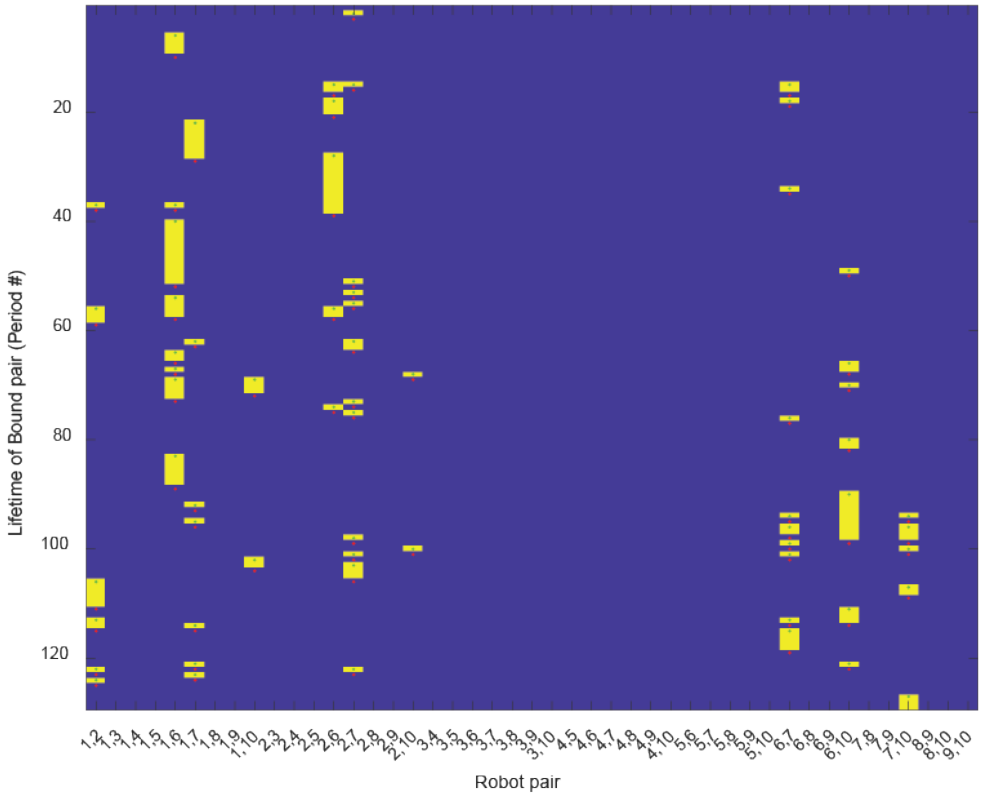

Figure 5.24: Binding Map for correlated robot pairs in a trial without Velcro.

graph (not shown here) serves as a quantitative measure of chain structure and connectivity. Figure 5.23 shows a representative time snapshot of this graph from a Velcro-enabled trial, with edge weights encoding both the velocity correlation and pairwise distance. By jointly analyzing these two metrics, we distinguish immediate physical neighbors from more distal members of extended chains.

In addition to structural analysis, the binary binding map enables extraction of bonding intervals, allowing us to compute the lifetimes of pairwise bonds over time. Figure 5.24 and Figure 5.25 present these binding maps for two representative trials—without and with Velcro adhesion, respectively. The presence of Velcro significantly promotes sustained clustering, as evidenced by the extended yellow bars shared among robots in the Velcro trial. These longer-lived bonds are further quantified in Figure 5.26, where the heavy-tailed distribution observed for the Velcro case indicates enhanced temporal stability and

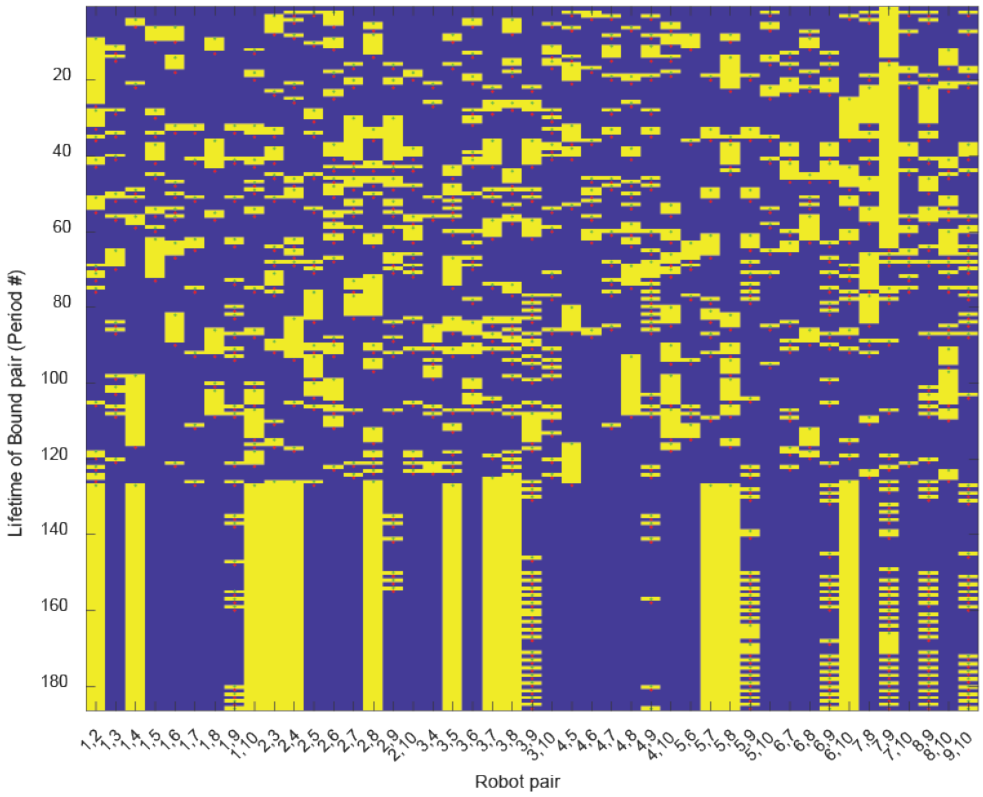

Figure 5.25: Binding Map for correlated robot pairs in a trial with Velcro.

persistent long-range order within the collective.

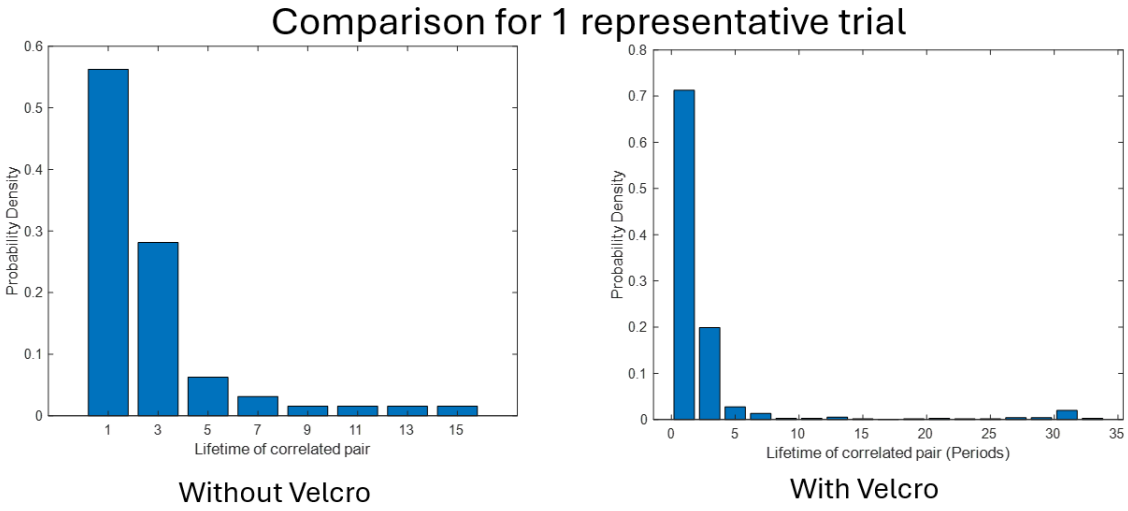

Figure 5.26: Comparison between lifetimes of correlated pairs for Velcro versus without Velcro collectives for that particular trial.

5.4.3 Mapping out micro-state table for clumped robots

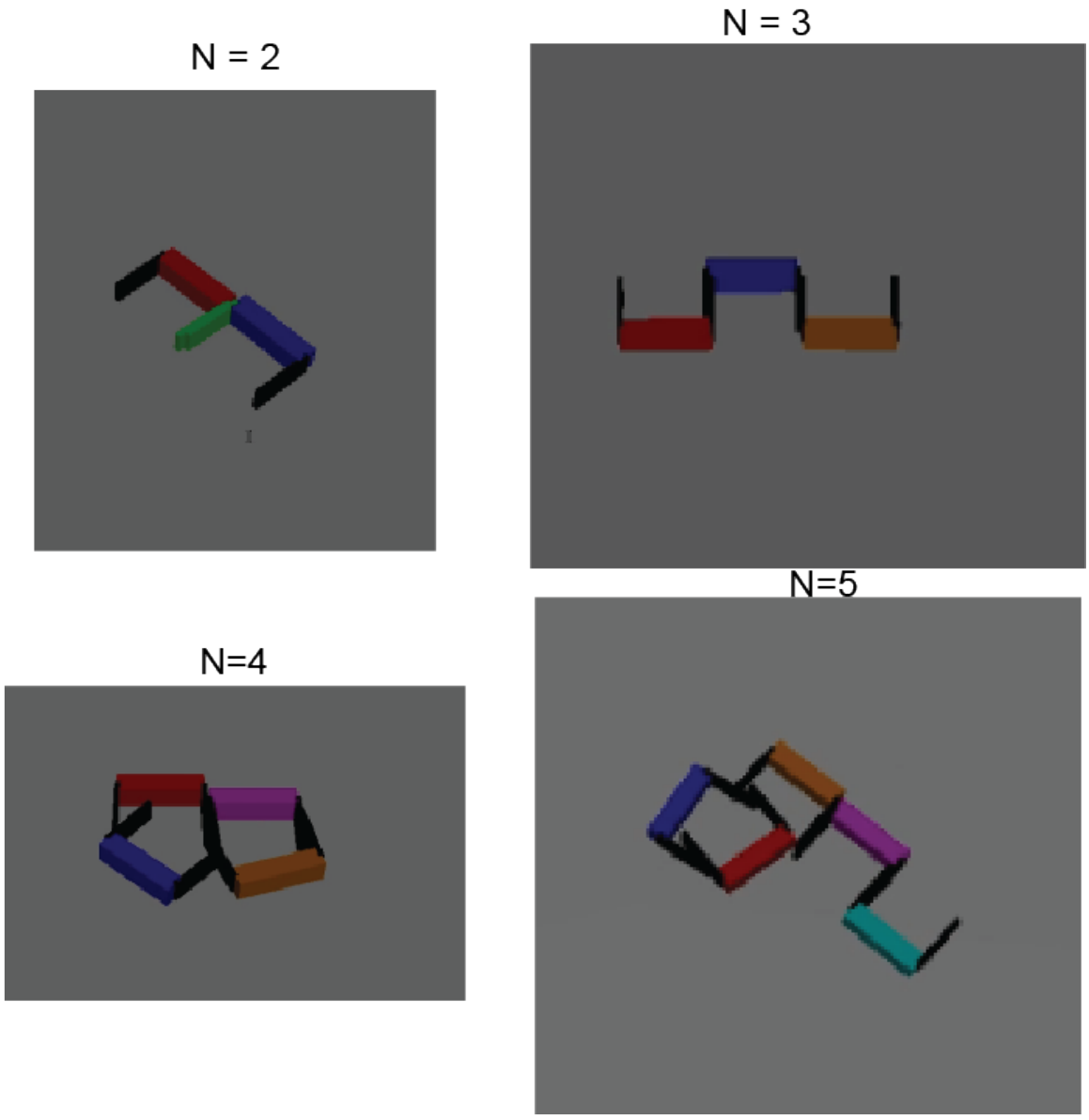

Figure 5.27: Configurations of adhered robots were systematically constructed by enforcing weld constraints between arms, enabling controlled micro-state enumeration for clusters up to N=5. (selected configurations for each N shown here)

Replicating the experimentally observed spontaneous adhesion in simulation proved non-trivial due to the configuration-dependent and stochastic nature of Velcro-induced binding. As an approximate solution, weld-joint constraints were introduced in MuJoCo between specific arm faces of robots, guided by empirical observations. This allowed for

the systematic construction of adhered configurations through a combinatorial specification of weld placements.

A microstate enumeration was carried out for robot clusters up to $N = 5$, generating a diverse set of physically connected configurations. Figure 5.27 shows representative snapshots of welded assemblies for different robot counts. Some configurations emerge as symmetric counterparts of others, resulting in redundancy in their transport behavior.

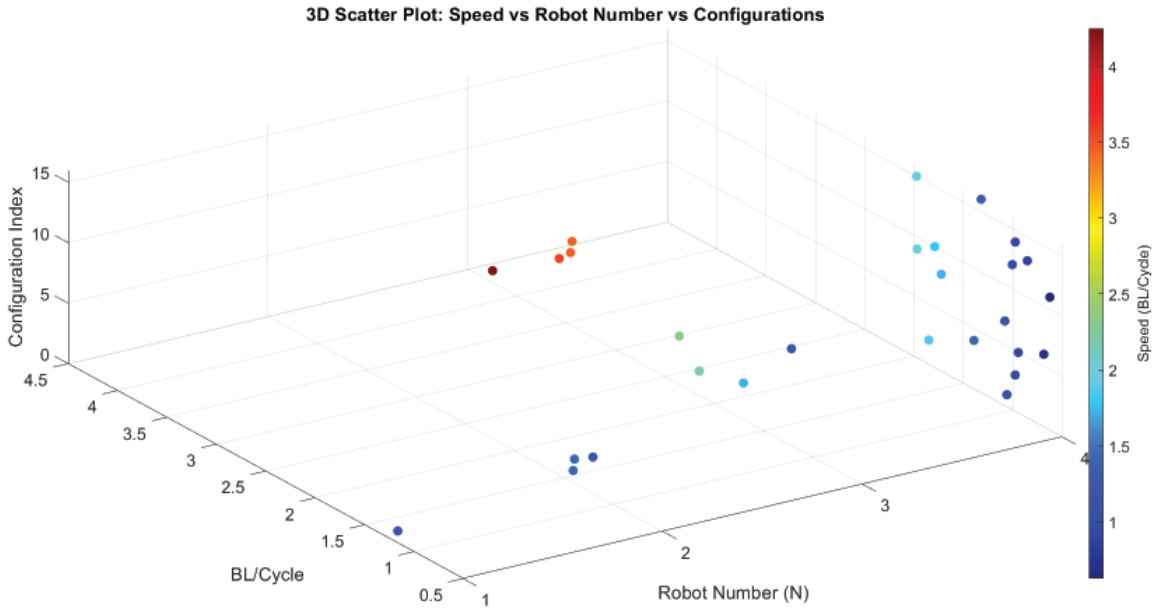

Figure 5.28: Classification of all configurations for each N was performed based on their center-of-mass speed to identify distinct transport behaviors.

To assess transport performance, each configuration was simulated and classified based on its center-of-mass speed. Figure 5.28 presents an initial phase diagram mapping the transport properties across the enumerated microstates.

5.5 Conclusion

This chapter highlighted the preliminary phenomenology observed when simulated dense unconfined collectives of robots actuated via different gaits were allowed to relax. We observed a range of different self-organized patterns which appeared and melted away. A graph based analysis allowed us to characterize these different phases. Lastly, we studied

a slightly modified experimental realization of these robots which were capable of only asymmetric reciprocal actuation. Affixing Velcro strips on the arms enhanced local clumping of robots and transport of the collectives. A correlation based analysis scheme was developed to extract similar statistics from the experiments as the simulations. Lastly, an approximation of the Velcro based adhesion mechanism seen in experiments was replicated in Mujoco where a pre-defined weld-joint constraint between selected arm faces acted as a proxy for the adhesion.

CHAPTER 6
CONCLUSION

This dissertation has explored how macroscopic, shape-changing robotic particles—rooted in the principles of granular matter—can give rise to emergent collective behaviors through internal actuation, environmental interactions, and minimal feedback. Inspired by the dynamics of granular materials but extending beyond their traditionally passive convex geometry, the robotic systems investigated here introduce internal degrees of freedom and concave morphologies, offering new mechanisms for self-organization in athermal, dissipative systems.

In **Chapter 2**, we examined a constrained, pinned ensemble of three shape-changing robots and uncovered a striking phenomenon: the spontaneous emergence of low-rattling, repeatable motion patterns. These low-noise states arose not from explicit programming but from the subtle interplay between internally driven actuation and constraints imposed by the environment. The findings illuminated how regions of dynamic stability can emerge amidst an otherwise chaotic phase space, echoing behavior found in other complex, high-dimensional systems.

The focus in **Chapter 3** shifted to the minimal interaction unit—a dyad of robots. Here, we uncovered a rich mechanism of *collisional binding*. Despite the repulsive nature of individual contacts, specific timing and orientation of these collisions led to the spontaneous formation of *long-lived mobile gliders*. These gliders exhibited asymmetric yet stable configurations that persisted over hundreds of gait cycles. Crucially, shape-induced concavity and tactile sensing enabled dynamic coordination, providing a decentralized route to structural stability.

In **Chapter 4**, we delved deeper into the transport properties of these bound gliders. By analyzing how symmetry-breaking in the internal gaits leads to net translation, we

demonstrated how *non-reciprocal actuation* can break time-reversal symmetry and generate directed motion. These gliders locomote through non-commutative interactions in configuration space, and changes in gait area revealed clear transitions between static and mobile states. Interestingly, the emergence of chirality under asymmetric actuation opened up a simple strategy for *steering* through *gait inversion* alone, requiring minimal feedback.

Finally, **Chapter 5** extended these principles to the many-body regime. Dense collectives of these robots, interacting through collisions and shape change, self-organized into extended morphologies such as *chains* and *loops*. The same concavity-enabled interactions that stabilized dyads were found to support long-range order in these larger assemblies. Moreover, by introducing a passive adhesion mechanism into the robot design, we further demonstrated that *mechanically reinforced contact*, even in the absence of any sensory feedback, could promote robust clustering and chaining. Gait templates once again played a central role in dictating the emergent spatial patterns.

Taken together, these results offer a blueprint for how **active, shape-changing, and collisionally interacting robots** can be harnessed to generate programmable collective behaviors. From minimal gliders to extended self-assembled structures, this work shows that decentralized, emergent coordination is achievable through the right blend of *geometry, actuation, and frictional interaction*. These insights not only enrich our understanding of robotic granular matter but also lay the groundwork for future efforts in scalable swarm robotics, adaptive materials, and the physics of non-equilibrium systems.

Appendices

APPENDIX A

COLLISIONAL BINDING AND TRANSPORT OF SHAPE-CHANGING ROBOT PAIRS

Robot Construction details The details for constructing the robots studied open loop with their corresponding CAD files and Arduino codes are provided in [171]. The parts for constructing scaled robots with force sensors are listed in Table Table A.1. The CAD file for the scaled robots is available at [172].

Table A.1: Parts List for scaled up Smarticles

Item	**Purchase Link**
LiPo Batteries	Amazon
FSR squares	DigiKey
Open RB 150 Boards	Robotis
XL 320 Servos	Robotis

Simulation details and calibration against experimental tracks.

The simulations of the smarticles were conducted using Project Chrono (referred to as Chrono), a multiphysics dynamics engine designed for rigid body dynamics and contact modeling. Chrono is an open-source software package [173], whose simulations have been extensively validated against experimental results and other numerical solvers [174]. The simulations in this study utilized Chrono version 8.0.

To model the rigid body dynamics of multibody systems, Chrono employs a multibody physics solver that incorporates kinematic constraints. The software adopts a Cartesian representation for the generalized position q and velocity $\dot{q}$ of rigid bodies, where q denotes the position of each body's center of mass in an absolute coordinate system. The governing

equations for multibody dynamics, in the absence of friction, are given by:

$$g(q,t) = 0, \tag{A.1}$$

$$M(q)\dot{v} = f(t,q,v) + G(q,t)\lambda. \tag{A.2}$$

The first equation defines the kinematic constraints between bodies, such as the revolute joints used in this study, which are captured by the constraint function $g(q,t)$. The second equation describes the system dynamics, where M represents the mass matrix, f includes internal forces (e.g., Coriolis forces, joint torques), and $G(q,t)\lambda$ denotes the constraint reaction forces.

Table A.2: Simulation parameters used in Chrono.

Parameter	Symbol	Value
Body length	W	54 mm
Body width	D	22 mm
Body height	H	30 mm
Body mass	m	35 g
Arm length	L	50 mm
Arm width	t	3 mm
Arm height	h	27 mm
Control P gain	K_P	0.15 N m/rad
Torque saturation	T_s	3.5* 1e-2 N m
Joint amplitude	α_{max}	90°
Joint angular frequency	ω	2.5*π rad/s
Static friction coefficient	μ_s	0.42
Kinetic friction coefficient	μ_k	0.37

Contact Modeling and Solver

In addition to external forces, bodies also experience contact forces, which dynamically appear or disappear based on their interactions. The contact resolution in this implementation is based on the discrete element method using a complementarity approach (DEM-C). Unlike penalty-based DEM methods (DEM-P), which model contact through elastic defor-

mation and small overlaps, the complementarity approach enforces non-penetration constraints through an optimization problem at each time step [174, 175]. This method ensures that either a finite gap or a nonzero contact force exists between bodies. Experimentally validated simulations benchmark DEM-P and DEM-C, highlighting their predictive accuracy and distinct strengths in modeling dry granular dynamics [176]. Further details on the mathematical formulation and solution strategy for this approach are provided in [174] and [175].

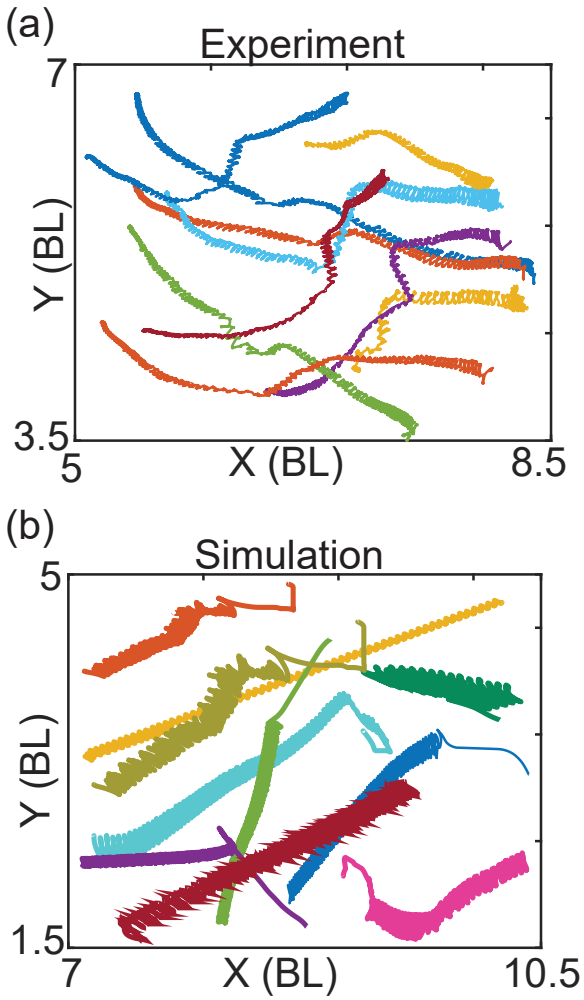

Figure A.1: Comparison between experimental (a) and simulation (b) glider COM tracks.

The time integration scheme employed in our simulations is the linear implicit Euler method, with a fixed step size of 0.0001 s. At each time step, a solver computes the

unknown accelerations and reaction forces. The default solver used is the Projected Successive Over-Relaxation (PSOR) method, an iterative approach that incorporates relaxation and immediate variable updates akin to successive over-relaxation (SOR) methods.

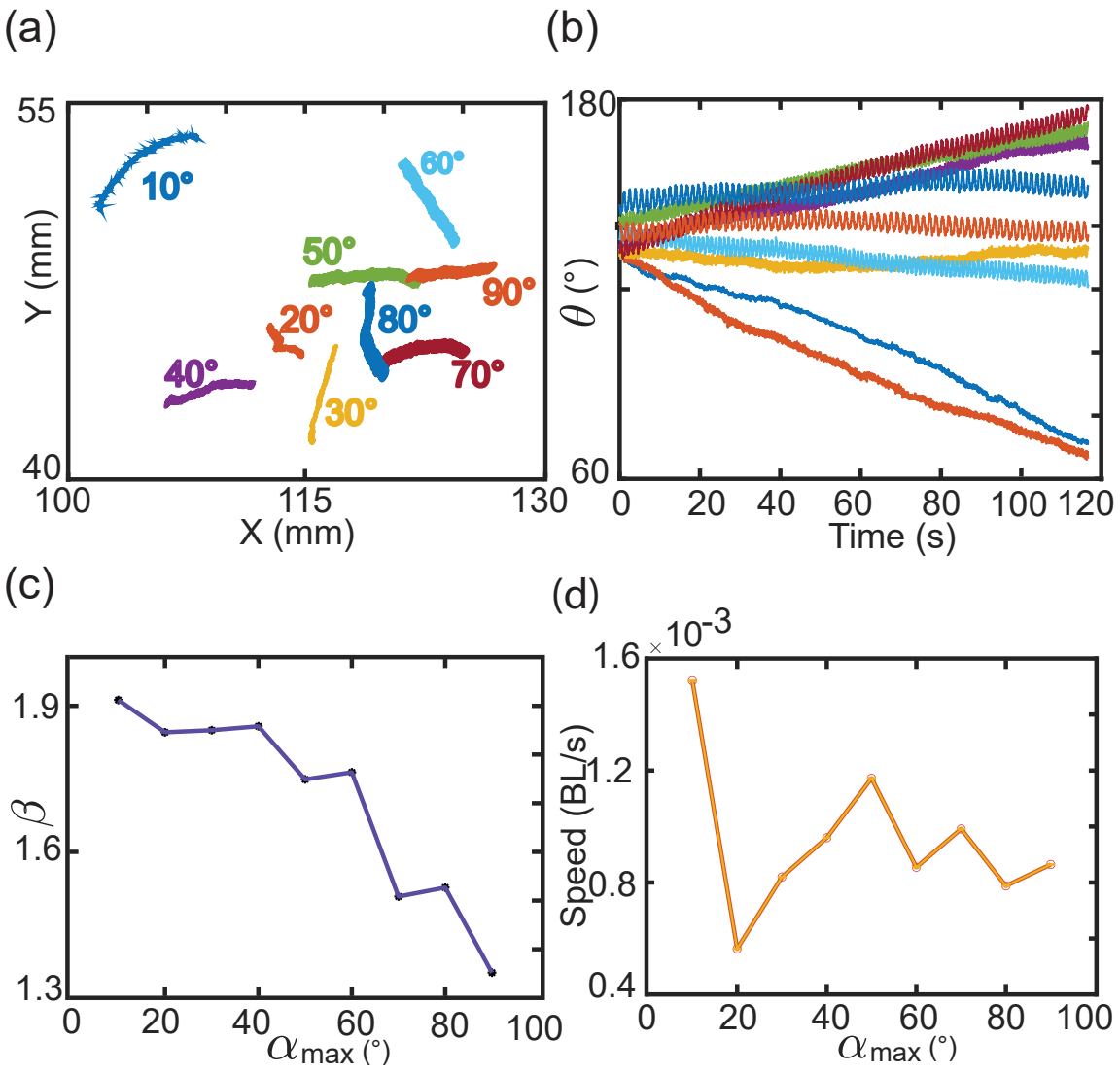

Figure A.2: (a) Tracks of the body center of the smarticle for different gait amplitudes, over 75 gait periods. (b) Time series for the angular coordinate of the smarticle. (c) β_{single} (MSD exponent) of a single smarticle vs. arm amplitude. (d) Speed of the body center vs. arm amplitude.

Simulation Parameters

For the purpose of creating our simulation, we created virtual smarticles with the same dimensions, mass, and material properties as our real robots. The key parameters used in the simulations are summarized in Table A.2. Once we initialized the smarticles with the prescribed gait, all collision detection and handling were managed by the physics engine, operating under the equations described above. A time step of $1e-4$ was sufficient for the solver to stably resolve collisions and generate the trajectories for individual robots. The full simulation code written in C++ is available at Ref. [172].

Figure A.1 shows the glider center of mass tracks for 10 different runs of the experiment and simulation started from arbitrary initial conditions which would ensure a stable glider. Experimental tracks curve more which can be attributed to the various sources of noise in the real world bringing about directional modulation in the headings of the robots. In our simulations we didn't add any external noise (over the accumulated numerical error), since we wanted to understand the phenomena in a cleaner setting. The tracks in the simulation have a much lower direction modulation consequently, which also shows up as tighter peaks in the PDF's of the relative coordinates shown in Figure 3.3 (c).

Single smarticle locomotion vs. amplitude.

The anomalous transport of the bound pairs that were formed at lower arm amplitudes was attributed mostly due to the enhanced drift of a single smarticle at lower amplitudes. We wanted to characterize the behavior of a single robot as a function of the amplitude. Figure A.2 (a-b) show the body center tracks and angular drift of a single robot for different gait amplitudes. The motion of a single smarticle is super-diffusive at higher and intermediate amplitudes and approaches the ballistic regime for lower values of the amplitude and it causes an increased drift speed, as shown in Figure A.2(c-d).

We suspected that this anomaly was due to the inertial effects from the overlap in the motions of the 2 arms, since the gait was executed at maximal motor speed for all arm amplitudes and we adjusted the dwelling time at the corners of the square to ensure the time

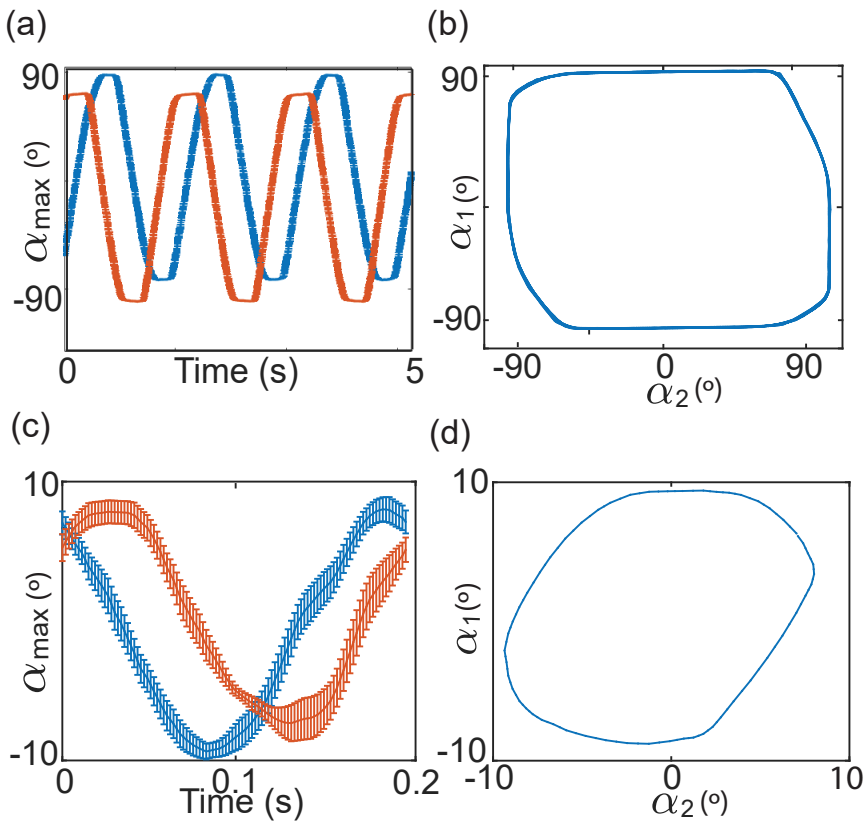

Figure A.3: Time-series of arm angles α_1, α_2 over 3 gait periods for 90° (a) and a single period for 10° (c) degree arm amplitudes (α_{max}) . Blue and orange curves represent arms 1 and 2 respectively. Gait represented in arm-angle configuration space (α_1, α_2), averaged over 10 periods, for 90° (b) and 10° (d) arm amplitudes.

period scaled commensurately with arm amplitude. At lower amplitudes, the value of this delay was so small that the other arm would start moving before the first arm completed its motion. This overlap in the motion of the two arms caused a drift in the center of the middle link. Figure A.3(a,c) shows the experimentally tracked arm angles of a single smarticle for 90 and 10 degrees, and when plotted in the shape configuration space Figure A.3(b,d), it becomes clear that in the lower amplitude regime the arms do not finish the prescribed range of motion.

Non-reciprocal binding affinity in glider formation.

Figure 3.6in the main manuscript shows the selectivity in initial configurations that ended up forming a glider vs. those that ended up being repelled. The scan was done by fix-

ing one robot and scanning the space around the reference in a constant radius $r = 1.3BL$ polar grid . Figure A.4 (a-d) shows a pictorial representation of the scan for all the four different initial gait phases p. The arrows represent the heading of the normal vector of the smarticle being scanned at that position in space. The black arrows represent the initial configurations that were attracted and the grey arrows represent the initial configurations which were repelled, with the white space representing physically inadmissible configurations similar to the pink, blue and black sectors in Figure 3.6.

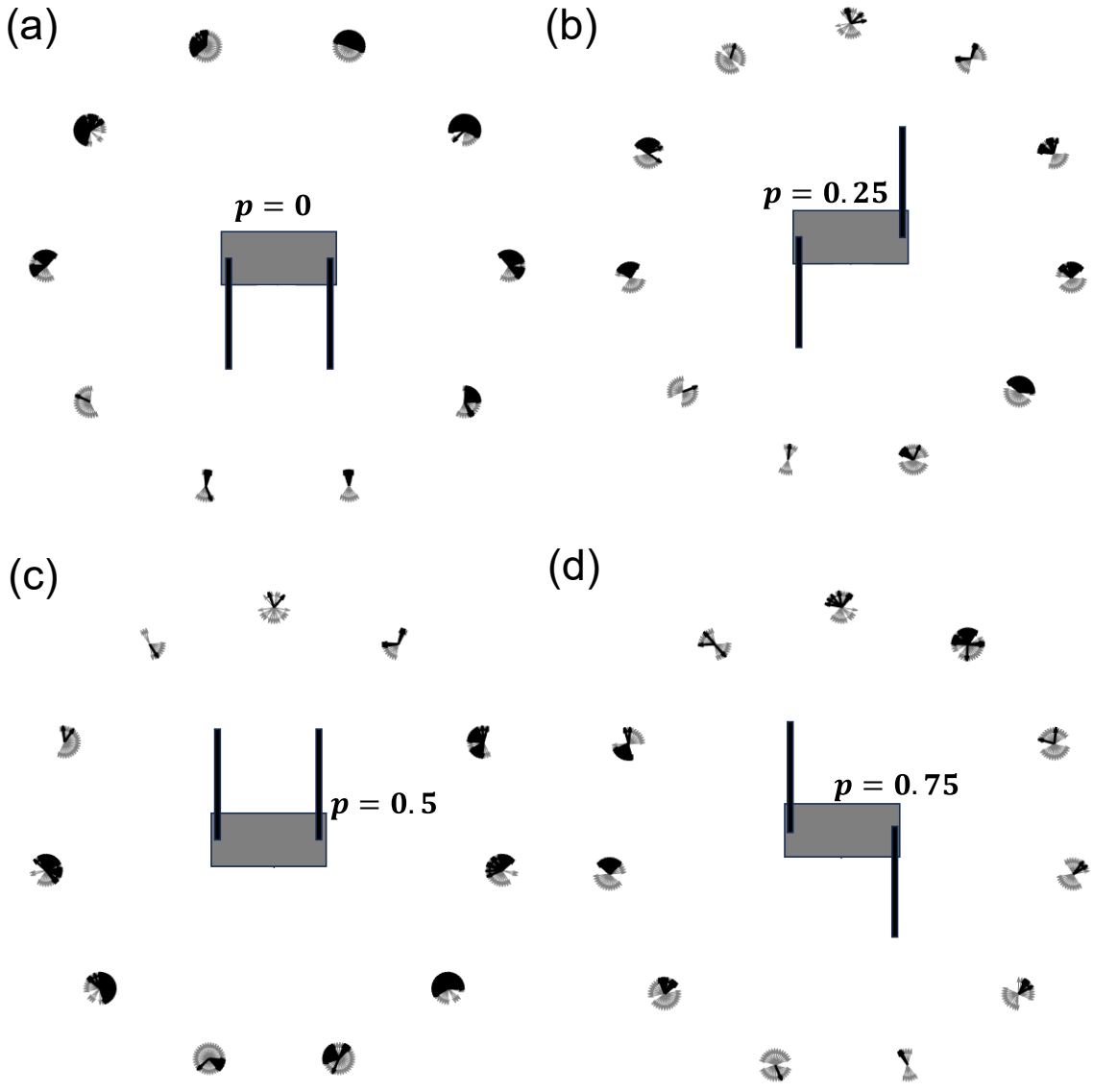

Figure A.4: Selectivity of initial configurations into regions of attraction vs. repulsion for a constant radius polar scan for different values of the initial gait phase p as shown in (a-d).

Upon second glance it becomes evident that the affinity of relative configurations to form bound pairs follows a non-reciprocal selection rule. The results indicate that the formation of a bound pair between two smarticles is governed by a non-reciprocal binding affinity based on their polar angle θ and relative headings ϕ. Initial configurations within an interaction range in 1st and 4th quadrants with respect to θ, are likely to form pairs bound shown by (pink sectors and black arrows) when robots point in approximately opposite directions, while those where robots point in approximately the same directions are likely to be repelled (blue sectors and grey arrows) or be physically inadmissible (black sectors or white space). In contrast, configurations in the 2nd and 3rd are generally repelled or physically inadmissible (black), as illustrated in Figure 3.6 (i-ii) and Figure A.4. The selection to the C2 configuration is strongly dependent upon the initial phase of the robots, as it required some initial arm opening for the robots to engulf each other and we don't observe a significant number of C2's for $p = 0$ and $p = 0.5$. Further the attracted configurations also have a (near perfect) reflection symmetry for a phase difference of half a cycle as seen in Figure A.4. Recently its been reported how non-reciprocal interactions between agents in spin models via preferential cone of vision and aligning torques gives rise to long range order in the collective [126, 127]. Collectives of shape changing robots also exhibit long range order mediated by gliders, which link up with other robots in the vicinity to form polymer chain like structures with a finite lifetime.

Figure A.5 (a) generalizes this scan for random positions and orientations of the scanned particle at a constant initial phase. We sweep the space around the reference smarticle extensively up-to $r = 6.5BL$ with randomly placed and oriented smarticles. The black arrows again represent configurations which were attracted and the grey arrows represent the configurations which were repelled. Figure A.5 (b) is an attempt to depict the *non reciprocal binding affinity* with a cartoon. The robots are simplified as spins positioned at their center of mass and oriented along the body normal vector. (i) shows the initial configurations which were attracted and repelled revealing the dominant preference for initial

configurations starting off with a dominant anti-alignment. (ii) depicts how the steady state ϕ values of the bound states maintain a slight deviation from either 180 ° and 0 ° similar to the chiral phases observed in several non-reciprocally interacting systems [21] and belong to the C1 and C2 glider conformation respectively.

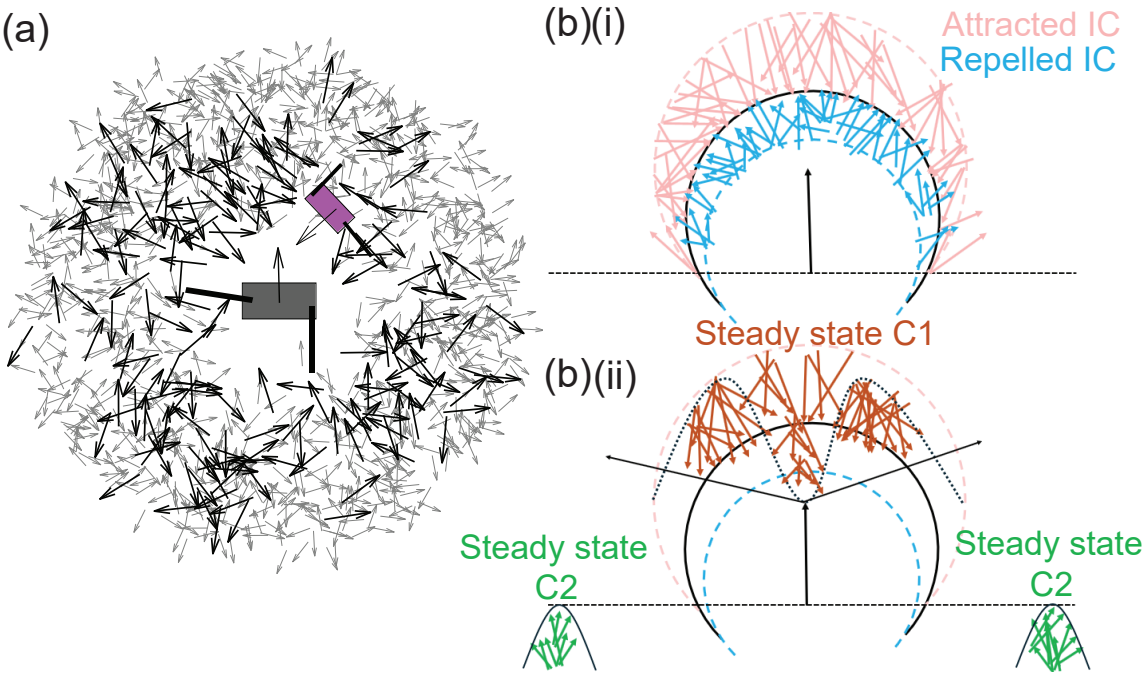

Figure A.5: Simplification of the binding interaction for a general phase (a) Initial configuration scan showing attracted and repelled glider configurations for a general position scan. Grey arrows represent repelled configurations, while black arrows represent attracted configurations. (b) (i) Cartoon showing attracted and repelled initial configurations wrt a reference smarticle. Only the configurations that started off with ϕ in the the 1st and 4th quadrants formed C2 gliders, as the selectivity to C2 also requires an additional constraint of the robots starting off with some opening between their arms. (b) (ii) A cartoon summarizing the attraction to the selected glider configurations based on the non-reciprocal selection of ϕ.

Impact sensor calibration and control algorithm.

We calibrated the force sensors by measuring the force pad readings during a squeeze event, a characteristic interaction in C2 gliders. One robot was held in a fixed 'U' shape typical of the C2 configuration, while the other moved its arms sequentially. Throughout this process, we continuously recorded sensor data. During the squeeze, the first arm made initial contact with the stationary robot and was then held passive, while the second arm,

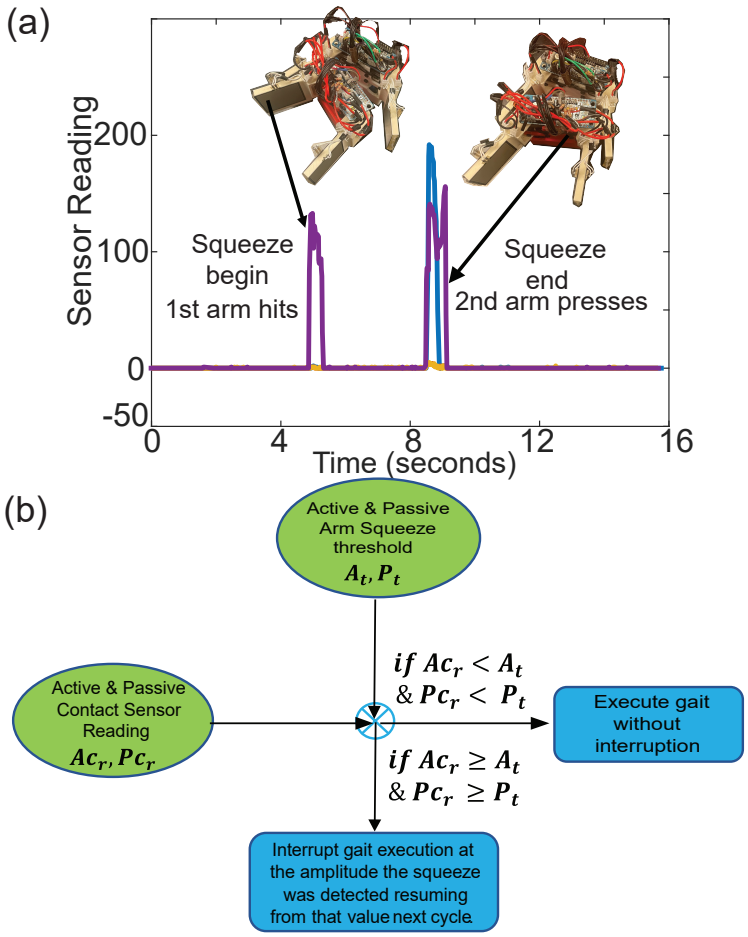

Figure A.6: (a) To get a measure of the values registered by the sensors during the squeeze event in a $C2$ glider we put the robots in similar relative configurations, and plotted the reading registered by the force sensor as the arms of the engulfing smarticle pressed against the other one. (b) Based on these values we were able to specify a sensor threshold for both the active (blue sensor curve in a) and passive (purple sensor curve in a) arms and compared it against the real-time sensor readings to adjust the gait amplitude upon detecting the squeeze.

acting as the active component, delivered an impact after a quarter cycle. The spikes in Figure A.6 (a) correspond to the impulse magnitudes recorded by the sensors on the arm faces during these two collisions. These readings established a threshold for implementing a feedback control strategy. Using this threshold with a defined tolerance, we compared real-time sensor readings to detect high-force interactions. If the instantaneous force exceeded the threshold, the robot adjusted its gait amplitude (shape concavity) accordingly. Figure A.6 (b) illustrates this control algorithm.

Dynamics and transport of open loop and feedback stabilized C2.

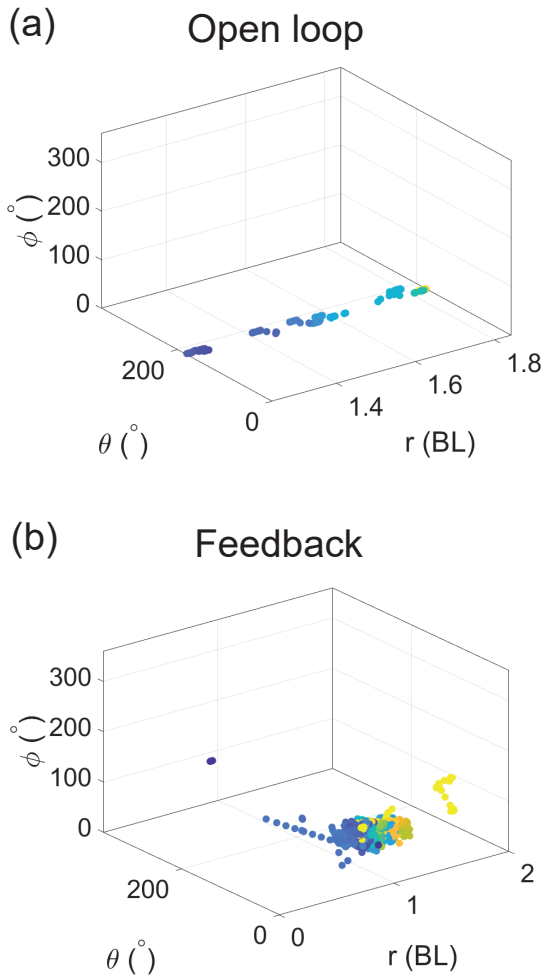

Figure A.7: (a) Configuration space of an open-loop C2 glider trajectory, color-coded by time. (b) Configuration space of a feedback-stabilized C2 glider. Tactile sensing disrupts the stable equilibrium (separated state) by inducing transient fluctuations in coordinates through timed concavity modulation.

The dynamics of open-loop and feedback-stabilized C2 gliders differ fundamentally in how stability and transport emerge. In the open-loop case, the system tends toward a stable equilibrium—where the gliders naturally separate—resulting in short-lived bound states. However, the feedback control strategy destabilizes this equilibrium by systematically introducing noise through impact-driven amplitude modulation. This controlled perturbation keeps the coordinates transiently fluctuating, preventing the gliders from settling into the

separated state Figure A.7. As a result, feedback stabilization extends the glider lifetime, as seen in the distribution of C2 lifetimes for different arm amplitudes. While both open-loop C2 gliders at $\alpha_{\max} = 85°$ and feedback-controlled gliders exhibit near-ballistic transport at long times, the latter persist significantly longer, enabling sustained transport over greater distances (Figure A.8, [177]).

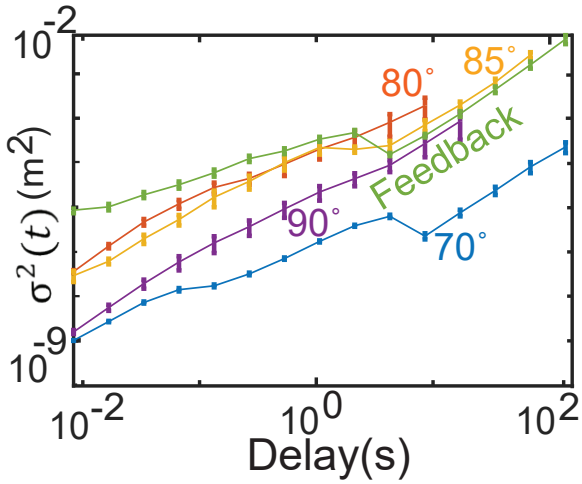

Figure A.8: Msd vs delay for C2 gliders of different gait amplitudes vs. the feedback stabilized glider.

APPENDIX B
SYMMETRY BREAKING TRANSPORT IN GLIDING DYADS FORMED BY COLLISIONS

Emergent Non-commutativity in dyad transport

We want to express the dyad's center of mass coordinates, (x, y, Θ), as a function of the emergent shape space arising from periodic collisional interactions between the robots executing their commanded gaits (Figure B.1). This shape space is parameterized by $|r|$, the separation between the robots, and ϕ_1 and ϕ_2, the tip angles accounting for exchange symmetry between the robots.

To construct the model, we analyze a trial with rectified persistent motion where the exchange symmetry was intentionally broken by introducing a bias ($\pm 8^\circ$) between the two robots, as detailed in the section section 4.4 . The net displacement of the dyad's center of mass is tracked by monitoring changes in the length and orientation of the vector pointing from robot 2 (Leader-Green) to robot 1 (Follower-Purple), as illustrated in Figure B.2 and Figure B.3. We visualize this vector in Figure B.4 as a massless extensible rod undergoing expansion, contraction, and rotation in the plane. The net displacement over a cycle is broken down into individual half-cycles (Figure B.8). In the first half-cycle, the leader undergoes a counterclockwise (CCW) rotation about the follower, while the second half-cycle results in a clockwise (CW) rotation. The follower remains nearly stationary throughout the cycle acting as a pivot point and incurs intermittent slipping every few cycles during the arm hooking to catch up with the leader.

The overall displacement resulting from this sequence of periodic shape changes can be computed using the commutator of the vector fields generated by the first and second half-cycle motions. The Lie bracket—a mathematical operation that computes the commu-

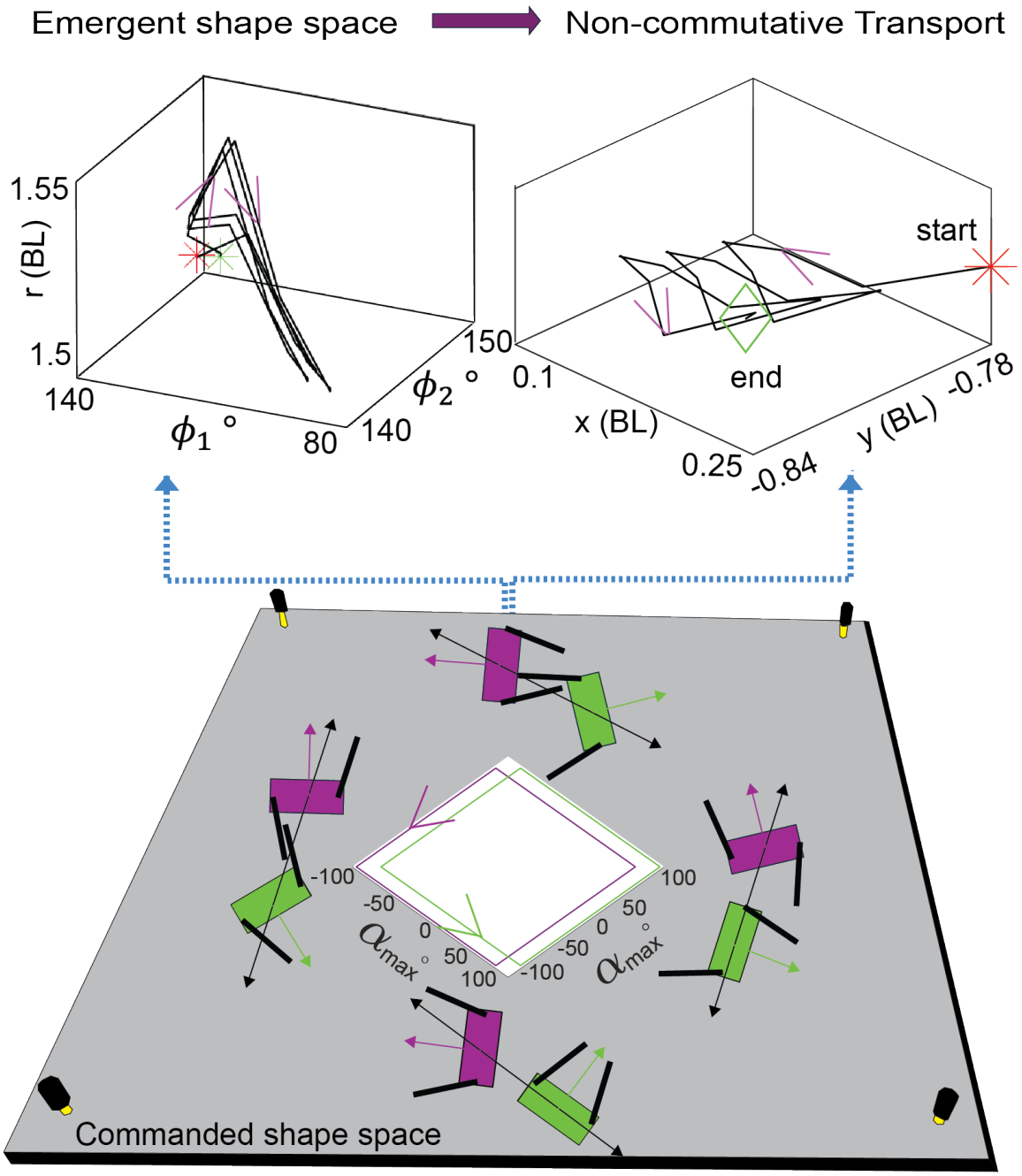

Figure B.1: The emergent shape space of the dyad, arising from the commanded shape space of individual robots and their collisional interactions, causes a non-commutative transport of the dyad's center of mass (CoM). This breaks rotational symmetry in the plane due to broken exchange symmetry within the dynamically bound entity resulting from the non-reciprocal square gait. The commanded shape space of the robots gives rise to an emergent shape space due to the persistent collisional interaction between the robots in the form of an attractor shown here in coordinates $|r|, \phi_1, \phi_2$, which gives rise to the displacement of the com. This symmetry breaking and impending transport is a direct consequence of the inherent non-reciprocity (time irreversibility) of the square gait being executed in the CCW direction here.

tator of two vector fields—quantifies how the sequence of one motion followed by another differs from the reverse sequence. This principle appears in parallel parking, where the order of steering actions matters, and the Lie bracket captures this non-commutative behavior [178, 179, 180, 181, 18].

For example, the Lie bracket of a ”forward movement” vector field with a ”steering left” vector field mathematically represents the net effect of moving forward while turning the wheel left, a critical maneuver in parallel parking. By combining multiple Lie brackets of different movements, one can design complex sequences of steering and acceleration actions to achieve precise parking positions. The dyad system differs from the parallel parking models in [178, 179], where forward motion and rotational steering are decoupled, and the vehicle moves forward at a constant steering angle. In contrast, the dyad's massless extensible rod undergoes coupled rotation and elongation/contraction in the plane, introducing greater complexity to the system.

B.1 First Half Cycle

We start by visualizing the overlaid robot positions at the beginning and end of the first cycle as shown in Figure B.2, shown along with the supplements of the exchange symmetry factored angles ϕ_1 and ϕ_2 described in Chapter 4.

Given Information

From the overlaid robot configurations, we can visualize the dyad configurations with the relevant coordinates used in the derivation in Figure B.3 with the respective robot bodies. The configuration can be simplified further visualizing just the vector pointing from robot 2 to robot 1 in Figure B.4. The displacement vector $\vec{S}$ during the first and second half cycles is given by $\vec{r}_{21_f} - \vec{r}_{21_i}$.

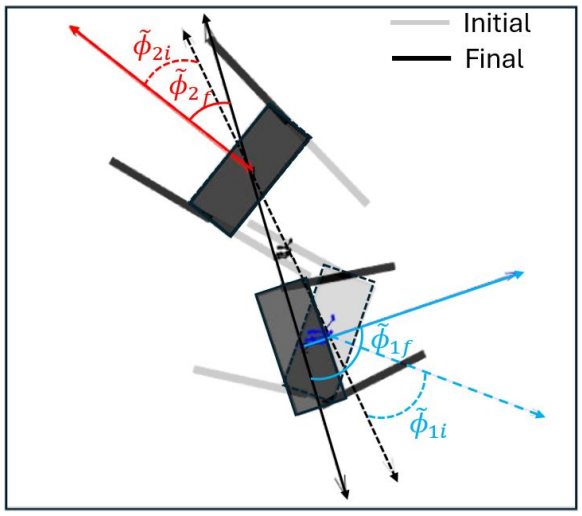

Figure B.2: Dyad Configuration with the two robots at the beginning and end of the first half cycle overlaid on top of each other. The dyad configuration with the individual robots at the beginning and end of the first half cycle is overlaid on top of each other. The lighter shade with the dashed line indicates the beginning of the half cycle, while the darker shade with the solid lines indicates the end of the half cycle. The angles $\tilde{\phi}_{1i,f}$ and $\tilde{\phi}_{2i,f}$ are the supplements of the angles ϕ_1 and ϕ_2 described in the main text to account for the exchange symmetry between the robots. The blue and red arrows being the normal vectors to the two robots respectively.

$$\vec{S} = \vec{r}_{21f} - \vec{r}_{21i}$$

Let:

- r be the initial length of the rod and Δr be the change in the length during this half cycle.
- Similarly, the angles at the end and beginning of the half cycle are given by, $\phi_{1,f} = \phi_{1,i} + \Delta\phi_1$, $\theta_{1,f} = \theta_{1,i} + \Delta\theta_1$.

The angle made by the $\vec{r}_{21}$ with the lab-frame $\hat{x}$ at the beginning and end of the half cycle is denoted by $\Theta_{1i,f}$.

$$\Theta_{1f} = \theta_{1f} + \phi_{1f} - 270 \qquad \Theta_{1i} = \theta_{1i} + \phi_{1i} - 270$$

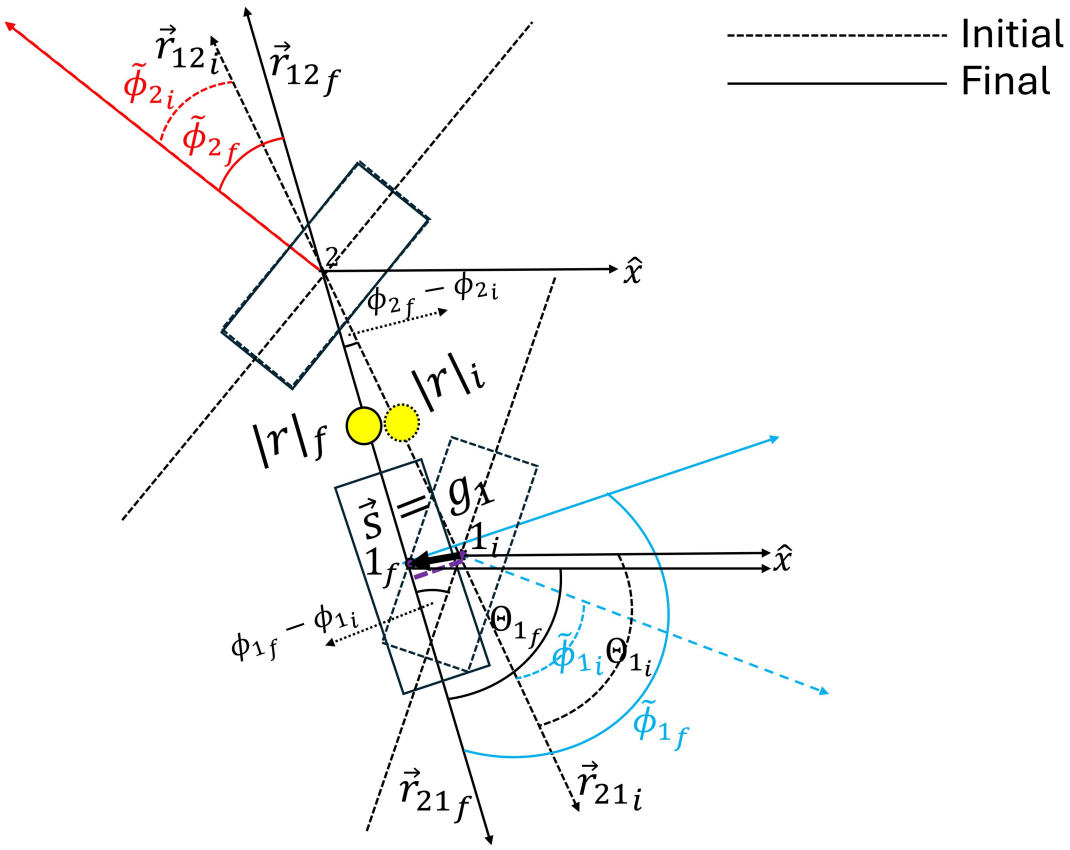

Figure B.3: Dyad Configuration highlighting all the relevant angles used in the derivation. The robot body configuration at the beginning (dashed) and end (solid) of the first half-cycle is overlaid, with a cartoon depicting all the angles used in the derivation. The angles $\tilde{\phi}_{1i,f}$ and $\tilde{\phi}_{2i,f}$ are the same as those in Fig. Figure B.2. The angles $\theta_{1,i}$ and $\theta_{1,f}$ are the angles made by Robot 1 with the x-axis of the Lab Frame, and $\Theta_{1,i}$ and $\Theta_{1,f}$ are the angles made by the vector pointing from Robot 2 to Robot 1 with the same. The net displacement of the center of Robot 1 during this half-cycle is given by $\vec{s} = g_1$.

The net angular displacement of the vector pointing from robot 2 to robot 1 at the end of this half cycle:

$$\Delta\Theta_1 = \Delta\theta_1 + \Delta\phi_1$$

The angles $\theta_{1i,f}$ and $\phi_{1i,f}$ are related by angular constraint of the form,

$$\Delta\theta_{2i} - \Delta\theta_{1i} = \Delta\phi_{1i} + \Delta\phi_{2i} \qquad \Delta\theta_{2f} - \Delta\theta_{1f} = \Delta\phi_{1f} + \Delta\phi_{2f}$$

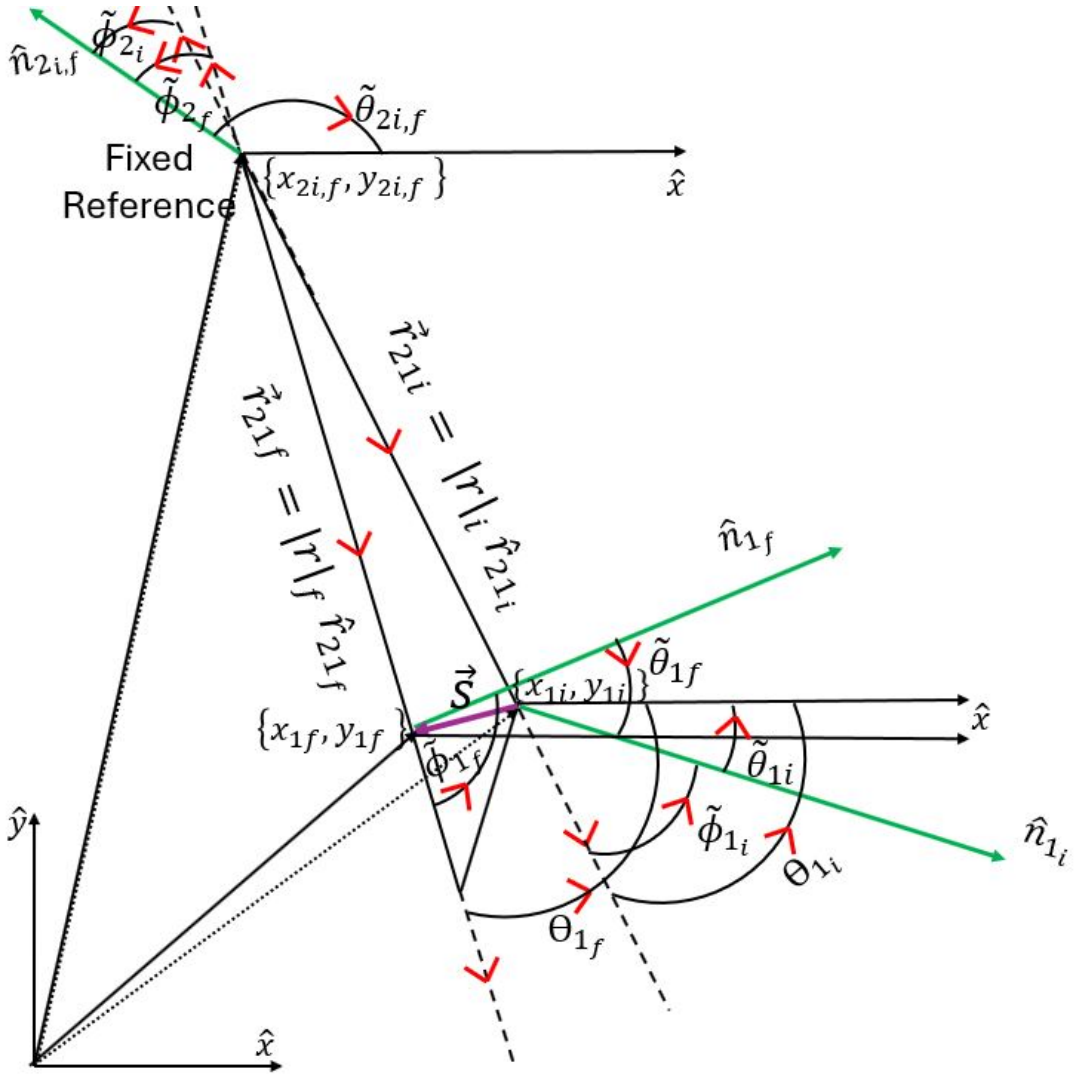

Figure B.4: Dyad displacement at the end of first half cycle. The vector pointing from Robot 2 to Robot 1 at the beginning and end of the first half cycle, with all the angles used in the derivation defined previously in Fig. Figure B.3.

which gives us,

$$\Delta\theta_2 - \Delta\theta_1 = \Delta\phi_1 + \Delta\phi_2$$

Expanding $\vec{S}$ in the lab frame.

$$\vec{S} = \{|r_{21_i}| \sin(\phi_{1,i} + \theta_{1,i}) - |r_{21_f}| \sin(\phi_{1,f} + \theta_{1,f})\}\hat{x} + \{|r_{21_f}| \cos(\phi_{1,f} + \theta_{1,f}) - |r_{21_i}| \cos(\phi_{1,i} + \theta_{1,i})\}\hat{y}$$

$$\vec{S} = \{r \sin(\phi_{1,i} + \theta_{1,i}) - (r + \Delta r) \sin(\phi_{1,i} + \theta_{1,i} + \Delta\theta_1 + \Delta\phi_1)\}\hat{x} + \{(r + \Delta r) \cos(\phi_{1,i} + \theta_{1,i} + \Delta\theta_1 + \Delta\phi_1) - r \cos(\phi_{1,i} + \theta_{1,i})\}\hat{y}$$

Expanding for small increments $\Delta\phi_1$ and $\Delta\theta_1$ and excluding $O(\Delta^2)$ terms.

For the x-component:

Using small-angle approximations:

$$\cos(\Delta\phi_1 + \Delta\theta_1) \approx 1, \quad \sin(\Delta\phi_1 + \Delta\theta_1) \approx \Delta\phi_1 + \Delta\theta_1,$$

$$g_{1,x} \approx -\Delta r \sin(\phi_{1,i} + \theta_{1,i}) + r \cos(\phi_{1,i} + \theta_{1,i})(\Delta\phi_1 + \Delta\theta_1).$$

For the y-component:

Using the same small-angle approximations:

$$g_{1,y} \approx \Delta r \cos(\phi_{1,i} + \theta_{1,i}) - r \sin(\phi_{1,i} + \theta_{1,i})(\Delta\phi_1 + \Delta\theta_1).$$

$$\vec{S} = \{-\Delta r \sin(\phi_{1,i} + \theta_{1,i}) + r \cos(\phi_{1,i} + \theta_{1,i})(\Delta\theta_1 + \Delta\phi_1)\}\hat{x} + \{\Delta r \cos(\phi_{1,i} + \theta_{1,i}) - r \sin(\phi_{1,i} + \theta_{1,i})(\Delta\theta_1 + \Delta\phi_1)\}\hat{y}$$

The displacement vector field g_1 as a function of Δr, $\Delta\phi_1$, and $\Delta\theta_1$ is:

$$g_1 = \begin{bmatrix} -\Delta r \sin(\phi_{1,i} + \theta_{1,i}) + r\cos(\phi_{1,i} + \theta_{1,i})(\Delta\phi_1 + \Delta\theta_1) \\ \Delta r \cos(\phi_{1,i} + \theta_{1,i}) - r\sin(\phi_{1,i} + \theta_{1,i})(\Delta\phi_1 + \Delta\theta_1) \\ \Delta\theta_1 + \Delta\phi_1 \end{bmatrix}$$

Matrix Representation

Combining these, the displacement $\vec{S} = g_1$ for the first half cycle in matrix form is:

$$g_1 = \begin{bmatrix} -\sin(\phi_{1,i} + \theta_{1,i}) & r\cos(\phi_{1,i} + \theta_{1,i}) & r\cos(\phi_{1,i} + \theta_{1,i}) \\ \cos(\phi_{1,i} + \theta_{1,i}) & -r\sin(\phi_{1,i} + \theta_{1,i}) & -r\sin(\phi_{1,i} + \theta_{1,i}) \\ 0 & 1 & 1 \end{bmatrix} \begin{bmatrix} \Delta r \\ \Delta\phi_1 \\ \Delta\theta_1 \end{bmatrix}$$

This matrix form captures the combined effect of changes in the rod's length (Δr), orientation ($\Delta\phi_1$), and global rotation ($\Delta\theta_1$) of the robot 1 on the state of the system, which is $x, y, \Delta\Theta$.

B.2 Second Half Cycle Robots

Similarly the overlayed the robot positions at the beginning and end of the second cycle as shown in Figure B.5. Likewise, we can visualize the dyad configurations with the respective robot bodies and relevant coordinates in this cycle Figure B.6 and the vector pointing from robot 1 to robot 1 as in Figure B.7.

Expression for g_2: Displacement in the Second Half-Cycle

The displacement vector g_2 for the second half-cycle is analogous to g_1 but uses the final values of the first half-cycle as its initial values. The displacements for the two cycles are shown in Figure B.8.

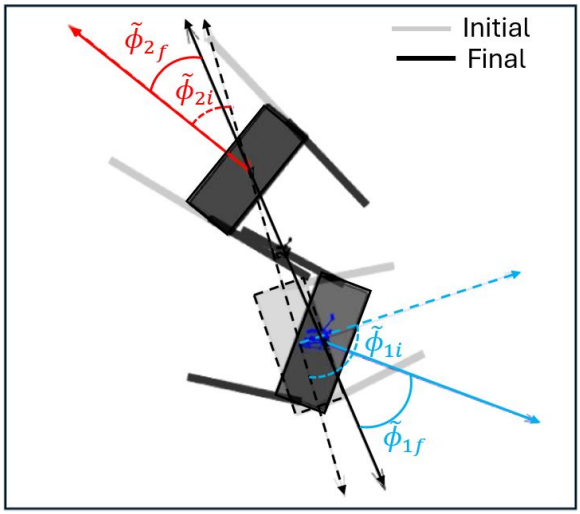

Figure B.5: Dyad Configuration with the two robots at the beginning and end of the second half cycle overlayed on top of each other. The dyad configuration with the individual robots at the beginning and end of the second half cycle is overlaid on top of each other.

Matrix Representation of g_2

Given that the initial state for g_2 corresponds to the final state of the previous half-cycle, we write:

$$g_2 = \begin{bmatrix} -\sin(\phi_{1,f} + \theta_{1,f}) & r_f \cos(\phi_{1,f} + \theta_{1,f}) & r_f \cos(\phi_{1,f} + \theta_{1,f}) \\ \cos(\phi_{1,f} + \theta_{1,f}) & -r_f \sin(\phi_{1,f} + \theta_{1,f}) & -r_f \sin(\phi_{1,f} + \theta_{1,f}) \\ 0 & 1 & 1 \end{bmatrix} \begin{bmatrix} \Delta r \\ \Delta\phi_1 \\ \Delta\theta_1 \end{bmatrix}$$

Here:

- $\phi_{1,f}$ is the final value of ϕ_1 from the previous half-cycle: $\phi_{1,f} = \phi_{1,i} + \Delta\phi_1$.
- $\theta_{1,f}$ is the final value of θ_1 from the previous half-cycle: $\theta_{1,f} = \theta_{1,i} + \Delta\theta_1$.
- r_f is the final value of r from the previous half-cycle: $r_f = r_i + \Delta r$.

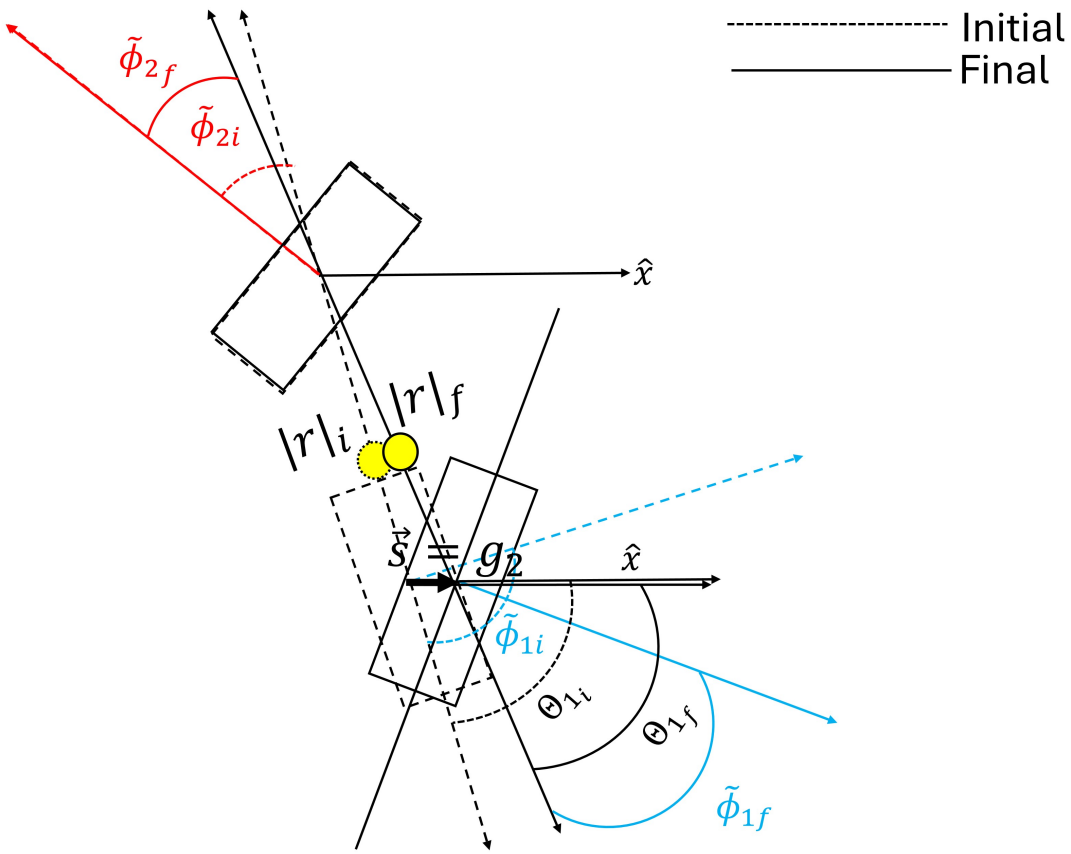

Figure B.6: Dyad Configuration with the two robots at the beginning and end of the second half cycle overlayed on top of each other. The configuration at the beginning and end of the first half-cycle is overlaid, with a cartoon depicting all the angles used in the derivation. $\theta_{1,i}$ and $\theta_{1,f}$ are the angles made by Robot 1 with the x-axis of the Lab Frame, and $\Theta_{1,i}$ and $\Theta_{1,f}$ are the angles made by the vector pointing from Robot 2 to Robot 1 with the same. The net displacement of the center of Robot 1 during this half cycle given by $\vec{s} = g_2$.

Vector Fields: Discrete vs Continuous

Discrete Version

In the discrete formulation, we derived the vector fields g_1 and g_2 from the net change in the configuration space (x, y, Θ) due to the net changes in the shape variables (r, ϕ_1, θ_1) in the half cycle ignoring the path taken by the dyads during the intermediate collision. The shape variables act as control parameters that evolve over time, leading to discrete updates in the configuration coordinates.

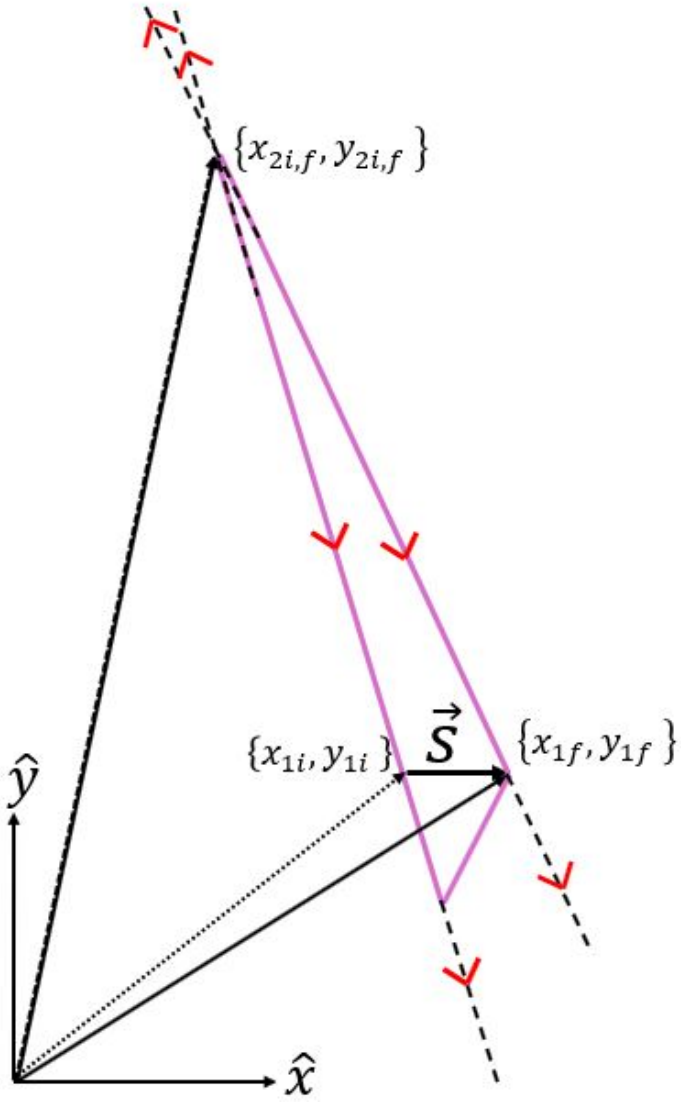

Figure B.7: Dyad displacement at the end of second half cycle. The vector pointing from Robot 2 to Robot 1 at the beginning and end of the second half cycle, with all the angles used in the derivation defined previously with the net displacement of the center of Robot 1 during this half cycle is given by $\vec{s} = g_2$.

- The configuration space update is given by:

$$\Delta x = -\Delta r \sin(\phi_{1,i} + \theta_{1,i}) + r\cos(\phi_{1,i} + \theta_{1,i})(\Delta\phi_1 + \Delta\theta_1),$$

$$\Delta y = \Delta r \cos(\phi_{1,i} + \theta_{1,i}) - r\sin(\phi_{1,i} + \theta_{1,i})(\Delta\phi_1 + \Delta\theta_1),$$

$$\Delta\Theta = \Delta\phi_1 + \Delta\theta_1,$$

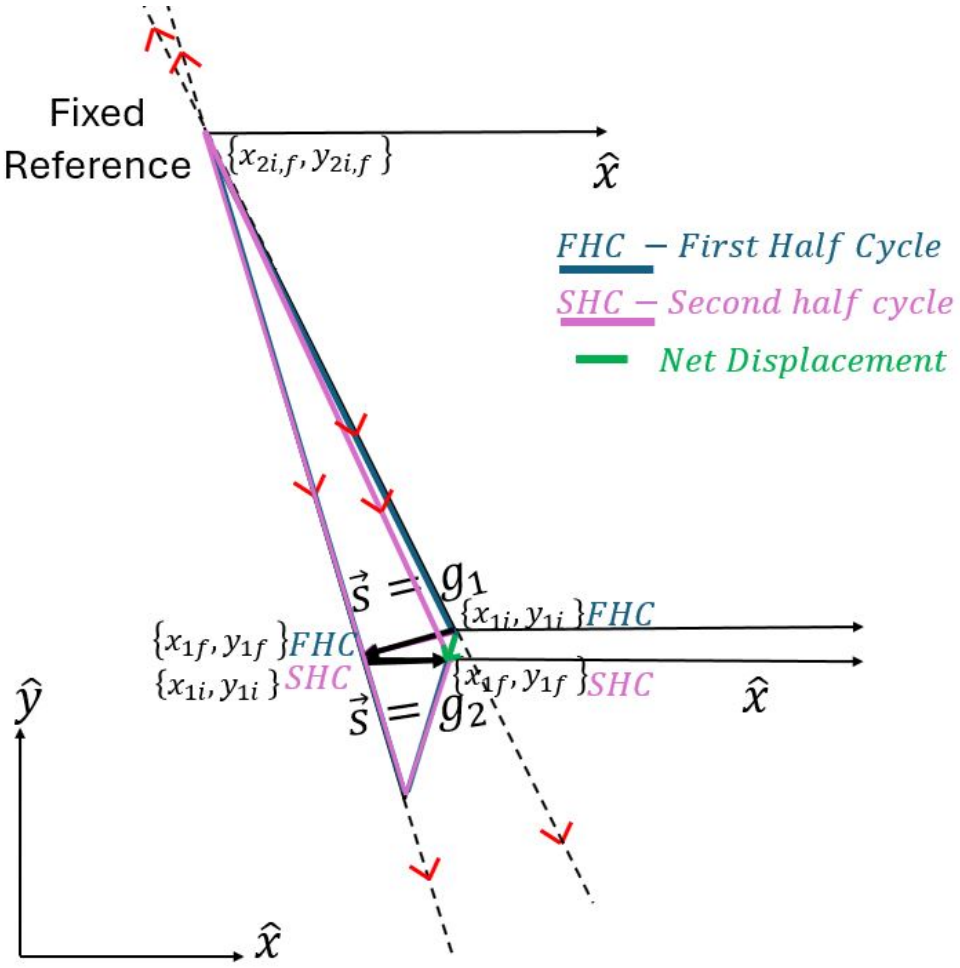

Figure B.8: Dyad Displacements for the first and second half cycles.The vector pointing from Robot 2 to Robot 1 at the beginning and end of the second half cycle with the effective displacements of the robot 1 body center being $\vec{s} = g_1$ and $\vec{s} = g_2$ for the individual half cycles. The net displacement over the cycle is shown in green.

Continuous Version

However in the dyads the motion of the robots during the collision is continuous and smooth and the configuration space coordinates (x, y, Θ) evolve as a function of the continuous evolution of the shape variables (r, ϕ_1, θ_1). The infinitesimal contributions from the changes in the shape variables $(\dot{r}, \dot{\phi}_1, \dot{\theta}_1)$ determine the vector fields.

- The continuous evolution can be expressed as:

$$\begin{aligned}
\frac{dx}{dt} &= -\dot{r}\sin(\phi_1+\theta_1) + r\cos(\phi_1+\theta_1)(\dot{\phi}_1+\dot{\theta}_1),\\
\frac{dy}{dt} &= \dot{r}\cos(\phi_1+\theta_1) - r\sin(\phi_1+\theta_1)(\dot{\phi}_1+\dot{\theta}_1),\\
\frac{d\Theta}{dt} &= \dot{\phi}_1+\dot{\theta}_1.
\end{aligned}$$

- The infinitesimal contributions from $\dot{r}$, $\dot{\phi}_1$, and $\dot{\theta}_1$ are mapped into configuration space through the vector fields.

To model the system's dynamics more accurately, we transition to the continuous versions of the vector field g, representing the contributions of the shape variables (r, ϕ_1, θ_1) to the configuration space variables (x, y, Θ).

$$\vec{g} = \begin{bmatrix} g_x \\ g_y \\ g_\Theta \end{bmatrix} = \begin{bmatrix} -\sin(\phi_1+\theta_1) & r\cos(\phi_1+\theta_1) & r\cos(\phi_1+\theta_1) \\ \cos(\phi_1+\theta_1) & -r\sin(\phi_1+\theta_1) & -r\sin(\phi_1+\theta_1) \\ 0 & 1 & 1 \end{bmatrix} \begin{bmatrix} \dot{r} \\ \dot{\phi}_1 \\ \dot{\theta}_1 \end{bmatrix}$$

The time evolution of the shape variables that serve as input to generate the configuration space from

$$t = 0 \quad ; \quad t = \frac{T}{2}$$

designated by the suffix FHC (first half cycle), generate the vector field g_1 and the time evolution of the variables from

$$t = \frac{T}{2} \quad ; \quad t = T$$

designated by the suffix SHC (second half cycle), generate the vector field g_2.

The piecewise continuous equation for the template shape profile $\bar{r}(t), \bar{\phi_1}(t), \bar{\theta_1}(t)$ as shown in Figure B.9, is split into the FHC and SHC with $T/2 = 8$ seconds. For the First half cycle between $t = (0, T/2)$ the piecewise continuous equations are given by:

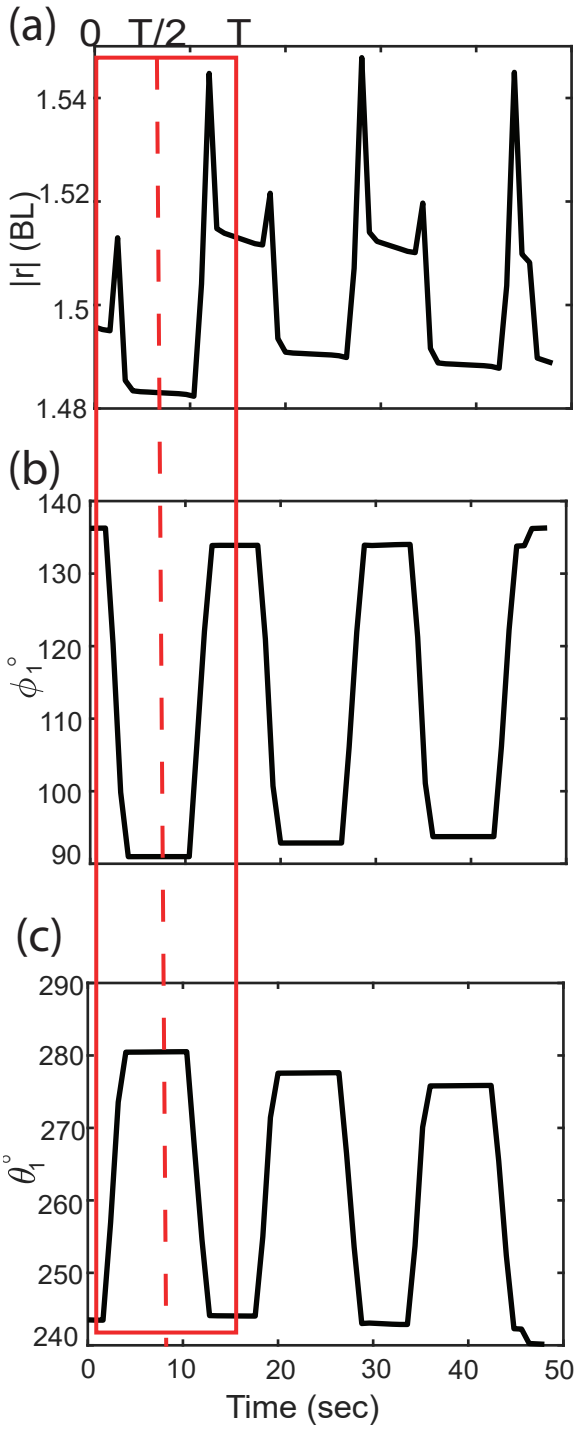

Figure B.9: Emergent shape space for the dyad for 3 consecutive periods.The emergent shape variables $|r|, \phi_1, \theta_1$ used in the model plotted for 3 consecutive period with the base template for each period being shown in red from $t = 0 - T$. We provide this piece-wise continuous template as an input for the corresponding half cycle for forward integrating the state update equation.

$\bar{r}_{\text{FHC}}(t)$:

$$\bar{r}_{\text{FHC}}(t) = \begin{cases} 1.495, & \text{if } 0 \leq t < 1.6 \\ 1.495 + \frac{1.512-1.495}{2.4-1.6}(t-1.6), & \text{if } 1.6 \leq t < 2.4 \\ 1.512 - \frac{1.512-1.48}{4-2.4}(t-2.4), & \text{if } 2.4 \leq t < 4 \\ 1.48, & \text{if } 4 \leq t < 8 \end{cases}$$

$\bar{\phi}_{1,\text{FHC}}(t)$:

$$\bar{\phi}_{1,\text{FHC}}(t) = \begin{cases} 136^\circ, & \text{if } 0 \leq t < 1.6 \\ 136^\circ + \frac{91^\circ-136^\circ}{4.0-1.6}(t-1.6), & \text{if } 1.6 \leq t < 4 \\ 91^\circ, & \text{if } 4 \leq t < 8 \end{cases}$$

$\bar{\theta}_{1,\text{FHC}}(t)$:

$$\bar{\theta}_{1,\text{FHC}}(t) = \begin{cases} 244^\circ, & \text{if } 0 \leq t < 1.6 \\ 244^\circ + \frac{281^\circ-244^\circ}{4.0-1.6}(t-1.6), & \text{if } 1.6 \leq t < 4 \\ 281^\circ, & \text{if } 4 \leq t < 8 \end{cases}$$

Similarly for the second half cycle between $t = (T/2, T)$, the piecewise-continuous equations are given by:

$\bar{r}_{\text{SHC}}(t)$:

$$\bar{r}_{\text{SHC}}(t) = \begin{cases} 1.48, & \text{if } 8 \leq t < 10.4 \\ 1.48 + \frac{1.544-1.48}{12-10.4}(t-10.4), & \text{if } 10.4 \leq t < 12 \\ 1.544 - \frac{1.544-1.514}{12.8-12}(t-12), & \text{if } 12 \leq t < 12.8 \\ 1.514, & \text{if } 12.8 \leq t < 16 \end{cases}$$

$\bar{\phi}_{1,\text{SHC}}(t)$:

$$\bar{\phi}_{1,\text{SHC}}(t) = \begin{cases} 91^\circ, & \text{if } 8 \leq t < 10.4 \\ 91^\circ + \frac{134^\circ - 91^\circ}{12.8 - 10.4}(t - 10.4), & \text{if } 10.4 \leq t < 12.8 \\ 134^\circ, & \text{if } 12.8 \leq t < 16 \end{cases}$$

$\bar{\theta}_{1,\text{SHC}}(t)$:

$$\bar{\theta}_{1,\text{SHC}}(t) = \begin{cases} 281^\circ, & \text{if } 8 \leq t < 10.4 \\ 281^\circ + \frac{244^\circ - 281^\circ}{12.8 - 10.4}(t - 10.4), & \text{if } 10.4 \leq t < 12.8 \\ 281^\circ, & \text{if } 12.8 \leq t < 16 \end{cases}$$

The Lie bracket $[g_1, g_2]$ is defined to account for the noncommutative effects between the vector fields for the first and second half cycles:

$$[g_1, g_2] = \frac{\partial g_2}{\partial q} g_1 - \frac{\partial g_1}{\partial q} g_2,$$

where $q = (x, y, \Theta)$ represents the configuration variables.

Trajectory integration scheme with noise and repetition

Configuration Space

The configuration space is represented as:

$$q = [x, y, \Theta]$$

where x, y are the planar coordinates and Θ is the orientation angle.

Shape Variables with Noise

The shape variables are defined as:

$$r, \phi_1, \theta_1$$

with their base profiles over time given by:

$$\bar{r}(t), \quad \bar{\phi}_1(t), \quad \bar{\theta}_1(t)$$

Noise is added to these base profiles for each cycle as:

$$r_i(t) = \bar{r}(t) + \eta_r, \quad \phi_{1,i}(t) = \bar{\phi}_1(t) + \eta_{\phi_1}, \quad \theta_{1,i}(t) = \bar{\theta}_1(t) + \eta_{\theta_1}$$

where:

$$\eta_r \sim \mathcal{N}(0, \sigma_r^2), \quad \eta_{\phi_1} \sim \mathcal{N}(0, \sigma_{\phi_1}^2), \quad \eta_{\theta_1} \sim \mathcal{N}(0, \sigma_{\theta_1}^2)$$

and $\sigma_r, \sigma_{\phi_1}, \sigma_{\theta_1}$ are the respective noise amplitudes.

Repetition of Cycles

The base profiles $\bar{r}(t), \bar{\phi}_1(t), \bar{\theta}_1(t)$ are defined for a cycle of duration T_{cycle}. The simulation repeats this cycle*num_cycles, ensuring that the initial conditions for the next cycle are the same as the end point for the previous cycle:

$$r_{\text{FHCfinal}} = r_{\text{SHCinitial}}, \quad \phi_{\text{1FHCfinal}} = \phi_{\text{1SHCinitial}}, \quad \theta_{\text{1FHCfinal}} = \theta_{\text{1SHCinitial}}$$

.

The Lie bracket between two vector fields g_1 and g_2 can be computed as:

$$[g_1, g_2] = \begin{bmatrix} g_{1y}g_{2\Theta} - g_{2y}g_{1\Theta} \\ g_{1\Theta}g_{2x} - g_{2\Theta}g_{1x} \\ 0 \end{bmatrix}$$

Integration Scheme

In the laboratory frame the configuration evolves as:

$$q_{i+1} = q_i + (g_1 + [g_1, g_2])\Delta t$$

The noise induces a drift in the template profile of shape variables $\bar{r}(t), \bar{\phi}_1(t), \bar{\theta}_1(t)$ and we account for it indirectly by adding noise at the beginning and ending points of the cycle instead of explicitly adding it to the state variables $q = [x, y, \Theta]$ hence we use a simple Euler scheme to forward integrate this difference equation until $t_i = T$ and obtain the trajectory for a cycle $\mathbf{q}(t)$ over $[0, T]$, with the process being repeated for the subsequent cycles as shown in Figure B.10.

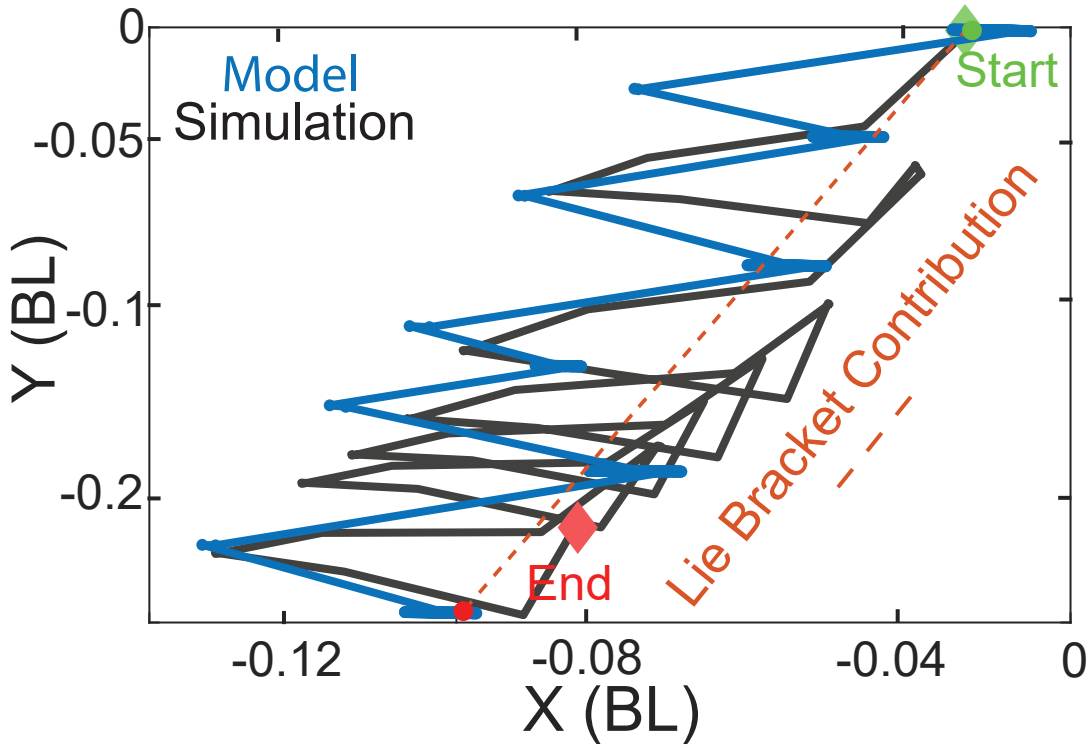

Figure B.10: Non Commutative Displacement. Forward integrating the model using the scheme described above for 5 cycles versus displacement from DEM simulation.

Transition from static bound states to gliders as a function of gait non-reciprocity.

We present the distributions of the three angular coordinates in the co-moving dyad frame, as defined in the main text, to illustrate the bifurcation in transport behavior as a function of increasing gait non-reciprocity. These results correspond to a family of gaits along the NE–SW diagonal in shape space, where the robots alternate between the two U configurations. These family of shape space trajectories exclusively produces the C1-type glider, which is the focus of our study. As the non-reciprocity parameter d—which defines the area enclosed by the gait—increases, the initially sharply peaked distributions broaden into more symmetric profiles, indicating a transition from static bound states to mobile, directionally transporting dyads.

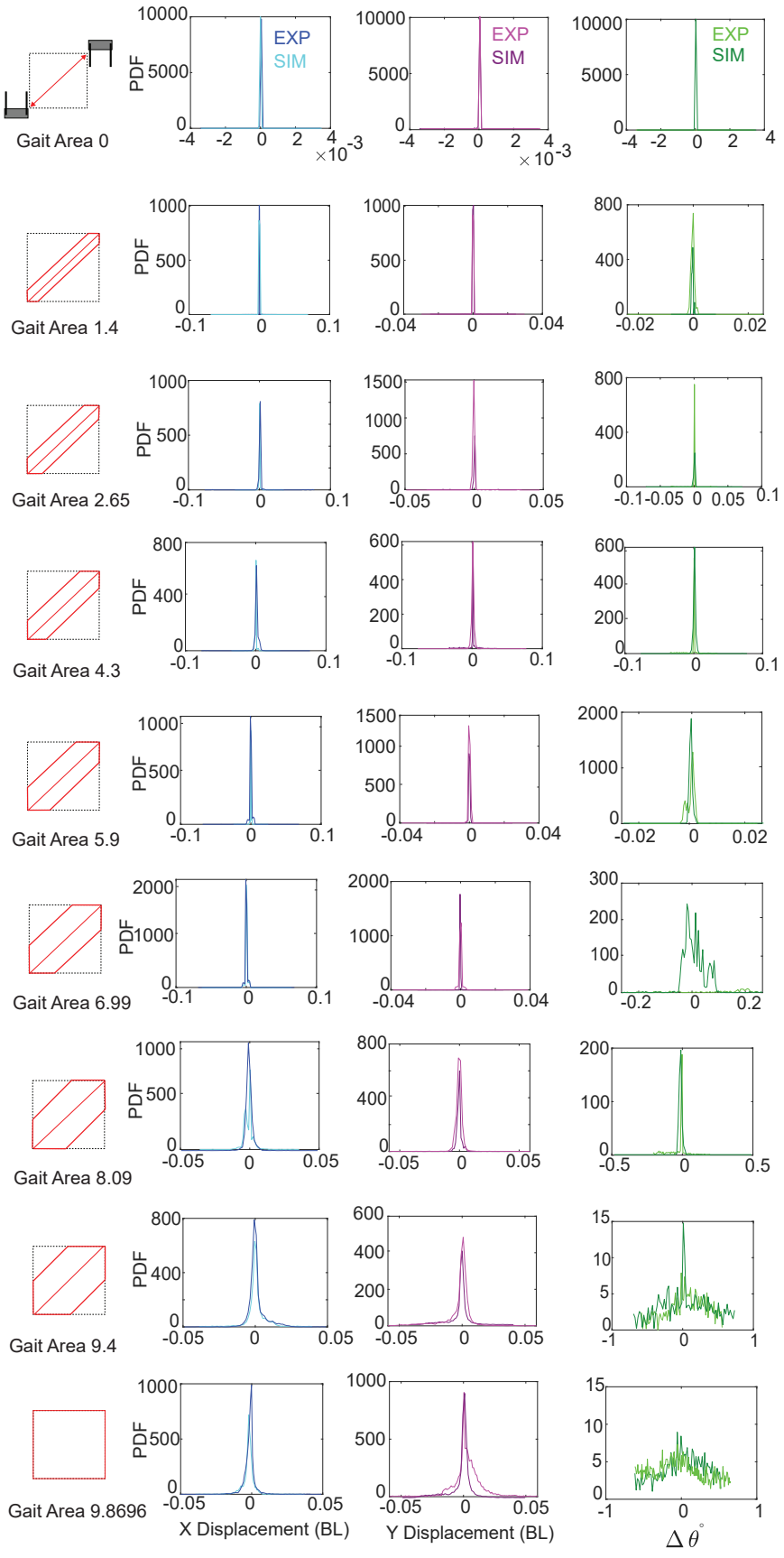

Figure B.11: The distributions for the com displacement components $s_{\hat{r}_x}$, $s_{\hat{r}_y}$, and the angular displacement $\Delta\theta$ in the comoving dyad frame for increasing gait areas.

REFERENCES

[1] J. S. Olafsen and J. S. Urbach, "Clustering, order, and collapse in a driven granular monolayer," *Physical Review Letters*, vol. 81, no. 20, p. 4369, 1998.

[2] I. S. Aranson and L. S. Tsimring, "Patterns and collective behavior in granular media: Theoretical concepts," *Reviews of Modern Physics*, vol. 78, no. 2, pp. 641–692, 2006.

[3] R. P. Behringer and B. Chakraborty, "The physics of jamming for granular materials," *Reports on Progress in Physics*, vol. 82, no. 1, p. 012 601, 2018.

[4] J. Deseigne, O. Dauchot, and H. Chaté, "Collective motion of vibrated polar disks," *Physical Review Letters*, vol. 105, no. 9, p. 098 001, 2010.

[5] A. Kudrolli, G. Lumay, D. Volfson, and L. S. Tsimring, "Swarming and swirling in self-propelled polar granular rods," *Physical Review Letters*, vol. 100, no. 5, p. 058 001, 2008.

[6] S. Ramaswamy, "The mechanics and statistics of active matter," *Annual Review of Condensed Matter Physics*, vol. 1, no. 1, pp. 323–345, 2010.

[7] N. Kumar, H. Soni, S. Ramaswamy, and A. K. Sood, "Flocking at a distance in active granular matter," *Nature Communications*, vol. 5, no. 1, p. 4688, 2014.

[8] M. E. Cates and J. Tailleur, "Motility-induced phase separation," *Annual Review of Condensed Matter Physics*, vol. 6, no. 1, pp. 219–244, 2015.

[9] E. Lauga, "Life around scallop theorem," *Soft Matter*, vol. 7, no. 7, pp. 3060–3065, 2011.

[10] D. I. Goldman, "Colloquium: Biophysical principles of undulatory self-propulsion in granular media," *Reviews of Modern Physics*, vol. 86, no. 3, p. 943, 2014.

[11] W. Savoie, A. Pazouki, D. Negrut, and D. I. Goldman, "Smarticles: Design and construction of smart particles to aid discovery of principles of smart, active granular matter," in *The First International Symposium on Swarm Behavior and Bio-Inspired Robotics*, 2015.

[12] P. E. Schiebel, J. M. Rieser, A. M. Hubbard, L. Chen, D. Z. Rocklin, and D. I. Goldman, "Mechanical diffraction reveals the role of passive dynamics in a slithering snake," *Proceedings of the National Academy of Sciences*, vol. 116, no. 11, pp. 4798–4803, 2019.

[13] X. Zhang, N. Naughton, T. Parthasarathy, and M. Gazzola, "Friction modulation in limbless, three-dimensional gaits and heterogeneous terrains," *Nature Communications*, vol. 12, no. 1, p. 6076, 2021.

[14] Y. Ozkan-Aydin, D. I. Goldman, and M. S. Bhamla, "Collective dynamics in entangled worm and robot blobs," *Proceedings of the National Academy of Sciences*, vol. 118, no. 6, e2010542118, 2021.

[15] E. M. Purcell, "Life at low reynolds number," *American Journal of Physics*, vol. 45, no. 1, pp. 3–11, 1977.

[16] A. Shapere and F. Wilczek, "Self-propulsion at low reynolds number," *Physical Review Letters*, vol. 58, no. 20, p. 2051, 1987.

[17] R. L. Hatton, Y. Ding, H. Choset, and D. I. Goldman, "Geometric visualization of self-propulsion in a complex medium," *Physical Review Letters*, vol. 110, no. 7, p. 078 101, 2013.

[18] R. L. Hatton and H. Choset, "Nonconservativity and noncommutativity in locomotion: Geometric mechanics in minimum-perturbation coordinates," *The European Physical Journal Special Topics*, vol. 224, no. 17, pp. 3141–3174, 2015.

[19] E. Gutman and Y. Or, "Symmetries and gaits for purcell's three-link microswimmer model," *IEEE Transactions on Robotics*, vol. 32, no. 1, pp. 53–69, 2015.

[20] A. Dinelli, J. O'Byrne, A. Curatolo, Y. Zhao, P. Sollich, and J. Tailleur, "Non-reciprocity across scales in active mixtures," *Nature Communications*, vol. 14, no. 1, p. 7035, 2023.

[21] M. Fruchart, R. Hanai, P. B. Littlewood, and V. Vitelli, "Non-reciprocal phase transitions," *Nature*, vol. 592, no. 7854, pp. 363–369, 2021.

[22] W. Savoie *et al.*, "Phototactic supersmarticles," *Artificial Life and Robotics*, vol. 23, pp. 459–468, 2018.

[23] P. Chvykov *et al.*, "Low rattling: A predictive principle for self-organization in active collectives," *Science*, vol. 371, no. 6524, pp. 90–95, 2021.

[24] M. L. Manning, "Essay: Collections of deformable particles present exciting challenges for soft matter and biological physics," *Physical Review Letters*, vol. 130, no. 13, p. 130 002, 2023.

[25] B. VanSaders and V. Vitelli, "Informational active matter," *arXiv preprint*, 2023. eprint: arXiv:2302.07402.

[26] C. Chin, R. Grimm, P. Julienne, and E. Tiesinga, "Feshbach resonances in ultracold gases," *Reviews of Modern Physics*, vol. 82, no. 2, pp. 1225–1286, 2010.

[27] I. Bloch, J. Dalibard, and W. Zwerger, "Many-body physics with ultracold gases," *Reviews of Modern Physics*, vol. 80, no. 3, pp. 885–964, 2008.

[28] E. W. Kolb and M. S. Turner, *The Early Universe* (Frontiers in Physics). Redwood City, CA: Addison-Wesley, 1990.

[29] T. Zhou and L. P. Kadanoff, "Inelastic collapse of 3 particles," *Physical Review E*, vol. 54, no. 1, p. 623, 1996.

[30] S. J. Cornell, M. R. Swift, and A. J. Bray, "Inelastic collapse of a randomly forced particle," *Physical Review Letters*, vol. 81, no. 6, p. 1142, 1998.

[31] C. J. Joachain, *Quantum Collision Theory*. North-Holland, 1983.

[32] J. M. Deutsch, "Quantum statistical mechanics in a closed system," *Physical Review A*, vol. 43, no. 4, pp. 2046–2049, 1991.

[33] W. H. Zurek, "Decoherence, einselection, and the quantum origins of the classical," *Reviews of Modern Physics*, vol. 75, no. 3, pp. 715–775, 2003.

[34] P. Philippe and D. Bideau, "Compaction dynamics of a granular medium under vertical tapping," *Europhysics Letters*, vol. 60, no. 5, pp. 677–683, 2002.

[35] J. M. Ottino, "Mixing, chaotic advection, and turbulence," *Annual Review of Fluid Mechanics*, vol. 22, no. 1, pp. 207–254, 1990.

[36] T. Shinbrot, A. Alexander, and F. J. Muzzio, "Spontaneous chaotic granular mixing," *Nature*, vol. 397, no. 6721, pp. 675–678, 1999.

[37] G. Metcalfe, T. Shinbrot, J. J. McCarthy, and J. M. Ottino, "Avalanche mixing of granular solids," *Nature*, vol. 374, no. 6517, pp. 39–41, 1995.

[38] S. McNamara and W. R. Young, "Inelastic collapse in two dimensions," *Physical Review E*, vol. 50, no. 1, R28, 1994.

[39] M. G. Clerc *et al.*, "Liquid-solid-like transition in quasi-one-dimensional driven granular media," *Nature Physics*, vol. 4, no. 4, pp. 249–254, 2008.

[40] A. J. Kabla and T. J. Senden, "Dilatancy in slow granular flows," *Physical Review Letters*, vol. 102, no. 22, p. 228 301, 2009.

[41] A. Fall, A. Lemaitre, F. Bertrand, D. Bonn, and G. Ovarlez, "Shear thickening and migration in granular suspensions," *Physical Review Letters*, vol. 105, no. 26, p. 268 303, 2010.

[42] A. J. Liu and S. R. Nagel, "Nonlinear dynamics: Jamming is not just cool any more," *Nature*, vol. 396, no. 6706, pp. 21–22, 1998.

[43] C. S. O'Hern, L. E. Silbert, A. J. Liu, and S. R. Nagel, "Jamming at zero temperature and zero applied stress: The epitome of disorder," *Physical Review E*, vol. 68, no. 1, p. 011 306, 2003.

[44] A. Abed Zadeh *et al.*, "Enlightening force chains: A review of photoelasticimetry in granular matter," *Granular Matter*, vol. 21, 2019.

[45] J. R. Howse, R. A. L. Jones, A. J. Ryan, T. Gough, R. Vafabakhsh, and R. Golestanian, "Self-motile colloidal particles: From directed propulsion to random walk," *Physical Review Letters*, vol. 99, no. 4, p. 048 102, 2007.

[46] M. C. Marchetti *et al.*, "Hydrodynamics of soft active matter," *Reviews of Modern Physics*, vol. 85, no. 3, pp. 1143–1189, 2013.

[47] M. Ballerini *et al.*, "Interaction ruling animal collective behavior depends on topological rather than metric distance: Evidence from a field study," *Proceedings of the National Academy of Sciences*, vol. 105, no. 4, pp. 1232–1237, 2008.

[48] A. Cavagna and I. Giardina, "Bird flocks as condensed matter," *Annual Review of Condensed Matter Physics*, vol. 5, no. 1, pp. 183–207, 2014.

[49] F. Ginelli, F. Peruani, M.-H. Pillot, H. Chaté, G. Theraulaz, and R. Bon, "Intermittent collective dynamics emerge from conflicting imperatives in sheep herds," *Proceedings of the National Academy of Sciences*, vol. 112, no. 41, pp. 12 729–12 734, 2015.

[50] H. Levine and D. I. Goldman, "Physics of smart active matter: Integrating active matter and control to gain insights into living systems," *Soft Matter*, vol. 19, no. 23, pp. 4204–4207, 2023.

[51] J. Palacci, S. Sacanna, A. P. Steinberg, D. J. Pine, and P. M. Chaikin, "Living crystals of light-activated colloidal surfers," *Science*, vol. 339, no. 6122, pp. 936–940, 2013.

[52] R. Soto and R. Golestanian, "Self-assembly of catalytically active colloidal molecules: Tailoring activity through surface chemistry," *Physical Review Letters*, vol. 112, no. 6, p. 068 301, 2014.

[53] R. Soto and R. Golestanian, "Self-assembly of active colloidal molecules with dynamic function," *Physical Review E*, vol. 91, no. 5, p. 052 304, 2015.

[54] I. Theurkauff, C. Cottin-Bizonne, J. Palacci, C. Ybert, and L. Bocquet, "Dynamic clustering in active colloidal suspensions with chemical signaling," *Physical Review Letters*, vol. 108, no. 26, p. 268 303, 2012.

[55] S. Li *et al.*, "Programming active cohesive granular matter with mechanically induced phase changes," *Science Advances*, vol. 7, no. 17, eabe8494, 2021.

[56] A. Deblais *et al.*, "Boundaries control collective dynamics of inertial self-propelled robots," *Physical Review Letters*, vol. 120, no. 18, p. 188 002, 2018.

[57] J.-F. Boudet *et al.*, "From collections of independent, mindless robots to flexible, mobile, and directional superstructures," *Science Robotics*, vol. 6, no. 56, eabd0272, 2021.

[58] M. J. Bowick, N. Fakhri, M. C. Marchetti, and S. Ramaswamy, "Symmetry, thermodynamics, and topology in active matter," *Physical Review X*, vol. 12, no. 1, p. 010 501, 2022.

[59] V. Narayan, S. Ramaswamy, and N. Menon, "Long-lived giant number fluctuations in a swarming granular nematic," *Science*, vol. 317, no. 5834, pp. 105–108, 2007.

[60] V. Schaller, C. Weber, C. Semmrich, E. Frey, and A. R. Bausch, "Polar patterns of driven filaments," *Nature*, vol. 467, no. 7311, pp. 73–77, 2010.

[61] Y. Sumino *et al.*, "Large-scale vortex lattice emerging from collectively moving microtubules," *Nature*, vol. 483, no. 7390, pp. 448–452, 2012.

[62] P. Sartori *et al.*, "Wall accumulation of bacteria with different motility patterns," *Physical Review E*, vol. 97, no. 2, p. 022 610, 2018.

[63] C. Li, A. O. Pullin, D. W. Haldane, H. K. Lam, R. S. Fearing, and R. S. Full, "Terradynamically streamlined shapes in animals and robots enhance traversibility through densely cluttered terrain," *Bioinspiration and Biomimetics*, vol. 10, no. 4, p. 046 003, 2015.

[64] V. P. Patil *et al.*, "Ultrafast reversible self-assembly of living tangled matter," *Science*, vol. 380, no. 6643, pp. 392–398, 2023.

[65] A. Deblais *et al.*, "Worm blobs as entangled living polymers: From topological active matter to flexible soft robot collectives," *Soft Matter*, vol. 19, no. 37, pp. 7057–7069, 2023.

[66] N. Weiner, Y. Bhosale, M. Gazzola, and H. King, "Mechanics of randomly packed filaments—the "bird nest" as meta-material," *Journal of Applied Physics*, vol. 127, no. 5, 2020.

[67] N. Gravish and D. I. Goldman, "Entangled granular media," in *Fluids, Colloids and Soft Materials: An Introduction to Soft Matter Physics*, P. Palffy-Muhoray and A. J. Hurd, Eds., Hoboken, NJ: Wiley, 2016, pp. 341–354.

[68] T. C. Day *et al.*, "Morphological entanglement in living systems," *Physical Review X*, vol. 14, no. 1, p. 011 008, 2024.

[69] Y. Jung, T. Plumb-Reyes, H.-Y. G. Lin, and L. Mahadevan, "Entanglement transition in random rod packings," *Proceedings of the National Academy of Sciences*, vol. 122, no. 8, e2401868122, 2025.

[70] E. Lauga and T. Powers, "The hydrodynamics of swimming micro-organisms," *Reports on Progress in Physics*, vol. 72, no. 9, p. 096 601, 2009.

[71] E. Lauga and D. Bartolo, "No many-scallop theorem: Collective locomotion of reciprocal swimmers," *Physical Review E*, vol. 78, no. 3, p. 030 901, 2008.

[72] H. Marvi *et al.*, "Sidewinding with minimal slip: Snake and robot ascent of sandy slopes," *Science*, vol. 346, no. 6206, pp. 224–229, 2014.

[73] G. L. Wagner and E. Lauga, "Crawling scallop: Friction-based locomotion with one degree of freedom," *Journal of Theoretical Biology*, vol. 324, pp. 42–51, 2013.

[74] D. L. Hu, J. Nirody, T. Scott, and M. J. Shelley, "The mechanics of slithering locomotion," *Proceedings of the National Academy of Sciences*, vol. 106, no. 25, pp. 10 081–10 085, 2009.

[75] R. L. Hatton, Y. Ding, H. Choset, and D. I. Goldman, "Geometric visualization of self-propulsion in a complex medium," *Physical Review Letters*, vol. 110, no. 7, p. 078 101, 2013.

[76] J. M. Rieser *et al.*, "Dynamics of scattering in undulatory active collisions," *Physical Review E*, vol. 99, no. 2, p. 022 606, 2019.

[77] T. Wang *et al.*, "Mechanical intelligence simplifies control in terrestrial limbless locomotion," *Science Robotics*, vol. 8, no. 85, eadi2243, 2023.

[78] B. Chong *et al.*, "Gait design for limbless obstacle aided locomotion using geometric mechanics," arXiv preprint arXiv:2302.06561, 2023.

[79] D. R. Brumley, M. Polin, T. J. Pedley, and R. E. Goldstein, "Hydrodynamic synchronization and metachronal waves on the surface of the colonial alga volvox carteri," *Physical Review Letters*, vol. 109, no. 26, p. 268 102, 2012.

[80] W. Gilpin, M. S. Bull, and M. Prakash, "The multiscale physics of cilia and flagella," *Nature Reviews Physics*, vol. 2, no. 2, pp. 74–88, 2020.

[81] R. E. Goldstein, M. Polin, and I. Tuval, "Emergent collective behavior in cilia and flagella," *Interface Focus*, vol. 1, no. 4, pp. 484–496, 2011.

[82] B. Guirao and J.-F. Joanny, "Spontaneous creation of macroscopic flow and metachronal waves in an array of cilia," *Biophysical Journal*, vol. 92, no. 6, pp. 1900–1917, 2007.

[83] J. Yuan, D. M. Raizen, and H. H. Bau, "Gait synchronization in caenorhabditis elegans," *Proceedings of the National Academy of Sciences*, vol. 111, no. 19, pp. 6865–6870, 2014.

[84] A. C. Quillen, A. Peshkov, E. Wright, and S. McGaffigan, "Metachronal waves in concentrations of swimming turbatrix aceti nematodes and an oscillator chain model for their coordinated motions," *Physical Review E*, vol. 104, no. 1, p. 014 412, 2021.

[85] A. Peshkov, S. McGaffigan, and A. C. Quillen, "Synchronized oscillations in swarms of nematode turbatrix aceti," *Soft Matter*, vol. 18, no. 6, pp. 1174–1182, 2022.

[86] W. Zhou, Z. Hao, and N. Gravish, "Collective synchronization of undulatory movement through contact," *Physical Review X*, vol. 11, no. 3, p. 031 051, 2021.

[87] W. Zhou, J. D. Peralta, Z. Hao, and N. Gravish, "Lateral contact yields longitudinal cohesion in active undulatory systems," *Physical Review E*, vol. 105, no. 5, p. 054 604, 2022.

[88] N. J. Mlot, C. A. Tovey, and D. L. Hu, "Fire ants self-assemble into waterproof rafts to survive floods," *Proceedings of the National Academy of Sciences*, vol. 108, no. 19, pp. 7669–7673, 2011.

[89] W. Savoie *et al.*, "A robot made of robots: Emergent transport and control of a smarticle ensemble," *Science Robotics*, vol. 4, no. 34, eaax4316, 2019.

[90] M. J. Falk, V. Alizadehyazd, H. Jaeger, and A. Murugan, "Learning to control active matter," *Physical Review Research*, vol. 3, no. 3, p. 033 291, 2021.

[91] S. Osat and R. Golestanian, "Non-reciprocal multifarious self-organization," *Nature Nanotechnology*, vol. 18, no. 1, pp. 79–85, 2023.

[92] T. Shimaya and K. A. Takeuchi, "Lane formation and critical coarsening in a model of bacterial competition," *Physical Review E*, vol. 99, no. 4, p. 042 403, 2019.

[93] S. Espada Burriel and R. Colin, "Active density pattern formation in bacterial binary mixtures," *PRX Life*, vol. 2, no. 2, p. 023 002, 2024.

[94] A. Martínez-Calvo, C. Trenado-Yuste, H. Lee, J. Gore, N. S. Wingreen, and S. S. Datta, "Interfacial morphodynamics of proliferating microbial communities," *Physical Review X*, vol. 15, no. 1, p. 011 016, 2025.

[95] L. B. Patterson and D. M. Parichy, "Zebrafish pigment pattern formation: Insights into the development and evolution of adult form," *Annual Review of Genetics*, vol. 53, no. 1, pp. 505–530, 2019.

[96] T. H. Tan *et al.*, "Odd dynamics of living chiral crystals," *Nature*, vol. 607, no. 7918, pp. 287–293, 2022.

[97] S. Saha, J. Agudo-Canalejo, and R. Golestanian, "Scalar active mixtures: The nonreciprocal cahn-hilliard model," *Physical Review X*, vol. 10, no. 4, p. 041 009, 2020.

[98] R. Hanai, "Nonreciprocal frustration: Time crystalline order-by-disorder phenomenon and a spin-glass-like state," *Physical Review X*, vol. 14, no. 1, p. 011 029, 2024.

[99] Z. You, A. Baskaran, and M. C. Marchetti, "Nonreciprocity as a generic route to traveling states," *Proceedings of the National Academy of Sciences*, vol. 117, no. 33, pp. 19 767–19 772, 2020.

[100] D. Helbing and P. Molnar, "Social force model for pedestrian dynamics," *Physical Review E*, vol. 51, no. 5, p. 4282, 1995.

[101] K. W. Rio, G. C. Dachner, and W. H. Warren, "Local interactions underlying collective motion in human crowds," *Proceedings of the Royal Society B: Biological Sciences*, vol. 285, no. 1878, p. 20 180 611, 2018.

[102] N. Bain and D. Bartolo, "Dynamic response and hydrodynamics of polarized crowds," *Science*, vol. 363, no. 6422, pp. 46–49, 2019.

[103] M. Jusup *et al.*, "Social physics," *Physics Reports*, vol. 948, pp. 1–148, 2022.

[104] M. Nagy, Z. Ákos, D. Biro, and T. Vicsek, "Hierarchical group dynamics in pigeon flocks," *Nature*, vol. 464, no. 7290, pp. 890–893, 2010.

[105] L. Conradt, "Models in animal collective decision-making: Information uncertainty and conflicting preferences," *Interface Focus*, vol. 2, no. 2, pp. 226–240, 2012.

[106] B. Wang, Y. Wu, G. Wang, L. Liu, G. Chen, and H.-T. Zhang, "Transition in collective motion decision making," *Physical Review E*, vol. 106, no. 1, p. 014 611, 2022.

[107] A. V. Ivlev, J. Bartnick, M. Heinen, C.-R. Du, V. Nosenko, and H. Löwen, "Statistical mechanics where newton's third law is broken," *Physical Review X*, vol. 5, no. 1, p. 011 035, 2015.

[108] K. Hayashi and S.-i. Sasa, "The law of action and reaction for the effective force in a non-equilibrium colloidal system," *Journal of Physics: Condensed Matter*, vol. 18, no. 10, p. 2825, 2006.

[109] S. Saha, S. Ramaswamy, and R. Golestanian, "Pairing, waltzing and scattering of chemotactic active colloids," *New Journal of Physics*, vol. 21, no. 6, p. 063 006, 2019.

[110] Y. Ashida, Z. Gong, and M. Ueda, "Non-hermitian physics," *Advances in Physics*, vol. 69, no. 3, pp. 249–435, 2020.

[111] H. Nassar *et al.*, "Nonreciprocity in acoustic and elastic materials," *Nature Reviews Materials*, vol. 5, no. 9, pp. 667–685, 2020.

[112] M. Brandenbourger, C. Scheibner, J. Veenstra, V. Vitelli, and C. Coulais, "Active impact and locomotion in robotic matter with nonlinear work cycles," arXiv preprint arXiv:2108.08837, 2021.

[113] J. Veenstra, O. Gamayun, X. Guo, A. Sarvi, C. V. Meinersen, and C. Coulais, "Nonreciprocal topological solitons in active metamaterials," *Nature*, vol. 627, no. 8004, pp. 528–533, 2024.

[114] A. Vardhan *et al.*, "Collisional binding and transport of shape changing robot pairs," Manuscript to be submitted along with this, 2025.

[115] A. Vardhan *et al.*, "Symmetry breaking transport in gliding dyads formed by collisions," 2025.

[116] Z. Jackson and K. Wiesenfeld, "Emergent, linked traits of fluctuation feedback systems," *Physical Review E*, vol. 104, no. 6, p. 064 216, 2021.

[117] J. Calvert and D. Randall, "A local–global principle for nonequilibrium steady states," *Proceedings of the National Academy of Sciences*, vol. 121, no. 42, e2411731121, 2024.

[118] D. Goldman, M. D. Shattuck, C. Bizon, W. D. McCormick, J. B. Swift, and H. L. Swinney, "Absence of inelastic collapse in a realistic three ball model," *Physical Review E*, vol. 57, no. 4, p. 4831, 1998.

[119] S. Ramaswamy and R. A. Simha, "The mechanics of active matter: Broken-symmetry hydrodynamics of motile particles and granular layers," *Solid State Communications*, vol. 139, no. 11-12, pp. 617–622, 2006.

[120] P. Sartori, E. Chiarello, G. Jayaswal, M. Pierno, G. Mistura, and E. Orlandini, "Wall accumulation of bacteria with different motility patterns," *Physical Review E*, vol. 97, no. 2, p. 022 610, 2018.

[121] M. Bär, R. Großmann, S. Heidenreich, and F. Peruani, "Self-propelled rods: Insights and perspectives for active matter," *Annual Review of Condensed Matter Physics*, vol. 11, pp. 441–466, 2020.

[122] H. Chaté, "Dry aligning dilute active matter," *Annual Review of Condensed Matter Physics*, vol. 11, pp. 189–212, 2020.

[123] D. Tam and A. E. Hosoi, "Optimal stroke patterns for purcell's three-link swimmer," *Physical Review Letters*, vol. 98, no. 6, p. 068 105, 2007.

[124] J. Eldering and H. O. Jacobs, "The role of symmetry and dissipation in biolocomotion," *SIAM Journal on Applied Dynamical Systems*, vol. 15, no. 1, pp. 24–59, 2016.

[125] A. Rosenfeld, "Measuring the sizes of concavities," *Pattern Recognition Letters*, vol. 3, no. 1, pp. 71–75, 1985.

[126] S. A. Loos, S. H. Klapp, and T. Martynec, "Long-range order and directional defect propagation in the nonreciprocal xy model with vision cone interactions," *Physical Review Letters*, vol. 130, no. 19, p. 198 301, 2023.

[127] L. P. Dadhichi, J. Kethapelli, R. Chajwa, S. Ramaswamy, and A. Maitra, "Nonmutual torques and the unimportance of motility for long-range order in two-dimensional flocks," *Physical Review E*, vol. 101, no. 5, p. 052 601, 2020.

[128] S. Weinberg, *The Quantum Theory of Fields*. Citado, 1995, vol. 3, pp. 25–26.

[129] A. Beekman, L. Rademaker, and J. Van Wezel, "An introduction to spontaneous symmetry breaking," *SciPost Physics Lecture Notes*, vol. 11, 2019.

[130] L. D. Landau and E. M. Lifshitz, *Statistical Physics: Volume 5*. Elsevier, 2013.

[131] R. E. Peierls, *Quantum Theory of Solids*. Clarendon Press, 1996.

[132] J. Bardeen, L. N. Cooper, and J. R. Schrieffer, "Theory of superconductivity," *Physical Review*, vol. 108, no. 5, p. 1175, 1957.

[133] P. W. Anderson, "Plasmons, gauge invariance, and mass," *Physical Review*, vol. 130, no. 1, p. 439, 1963.

[134] W. Meissner and R. Ochsenfeld, "Ein neuer effekt bei eintritt der supraleitfähigkeit," *Naturwissenschaften*, vol. 21, no. 44, pp. 787–788, 1933.

[135] P. W. Higgs, "Broken symmetries, massless particles and gauge fields," *Physics Letters*, vol. 12, pp. 132–133, 1964.

[136] Y. Nambu, "Quasi-particles and gauge invariance in the theory of superconductivity," *Physical Review*, vol. 117, no. 3, p. 648, 1960.

[137] P. W. Anderson, "More is different: Broken symmetry and the nature of the hierarchical structure of science," *Science*, vol. 177, no. 4047, pp. 393–396, 1972.

[138] J. Denk and E. Frey, "Pattern-induced local symmetry breaking in active-matter systems," *Proceedings of the National Academy of Sciences*, vol. 117, no. 50, pp. 31 623–31 630, 2020.

[139] D. P. Singh *et al.*, "Interface-mediated spontaneous symmetry breaking and mutual communication between drops containing chemically active particles," *Nature Communications*, vol. 11, no. 1, p. 2210, 2020.

[140] R. Golestanian, "Non-reciprocal active-matter: A tale of "loving hate, brawling love" across the scales," *Europhysics News*, vol. 55, no. 3, pp. 12–15, 2024.

[141] T. Frohoff-Hülsmann, U. Thiele, and L. M. Pismen, "Non-reciprocity induces resonances in a two-field cahn–hilliard model," *Philosophical Transactions of the Royal Society A*, vol. 381, no. 2245, p. 20 220 087, 2023.

[142] F. Brauns and M. C. Marchetti, "Nonreciprocal pattern formation of conserved fields," *Physical Review X*, vol. 14, no. 2, p. 021 014, 2024.

[143] R. K. Gupta, R. Kant, H. Soni, A. K. Sood, and S. Ramaswamy, "Active nonreciprocal attraction between motile particles in an elastic medium," *Physical Review E*, vol. 105, no. 6, p. 064 602, 2022.

[144] H. Hong and S. H. Strogatz, "Kuramoto model of coupled oscillators with positive and negative coupling parameters: An example of conformist and contrarian oscillators," *Physical Review Letters*, vol. 106, no. 5, p. 054 102, 2011.

[145] M. Brandenbourger, X. Locsin, E. Lerner, and C. Coulais, "Non-reciprocal robotic metamaterials," *Nature Communications*, vol. 10, no. 1, p. 4608, 2019.

[146] E. Tjhung, D. Marenduzzo, and M. E. Cates, "Spontaneous symmetry breaking in active droplets provides a generic route to motility," *Proceedings of the National Academy of Sciences*, vol. 109, no. 31, pp. 12 381–12 386, 2012.

[147] R. Li and B. Bowerman, "Symmetry breaking in biology," *Cold Spring Harbor Perspectives in Biology*, vol. 2, no. 3, a003475, 2010.

[148] E. M. Purcell, "Life at low reynolds number," in *Physics and Our World: Reissue of the Proceedings of a Symposium in Honor of Victor F. Weisskopf*, 2014, pp. 47–67.

[149] Y. Or, "Asymmetry and stability of shape kinematics in microswimmers' motion," *Physical Review Letters*, vol. 108, no. 25, p. 258 101, 2012.

[150] O. Wiezel and Y. Or, "Optimization and small-amplitude analysis of purcell's three-link microswimmer model," *Proceedings of the Royal Society A: Mathematical, Physical and Engineering Sciences*, vol. 472, no. 2192, p. 20 160 425, 2016.

[151] A. D. Shapere, "Gauge mechanics of deformable bodies: A theory of something," Ph.D. dissertation, University of California, Santa Barbara, 1988.

[152] A. Shapere and F. Wilczek, "Geometry of self-propulsion at low reynolds number," *Journal of Fluid Mechanics*, vol. 198, pp. 557–585, 1989.

[153] R. L. Hatton and H. Choset, "Geometric swimming at low and high reynolds numbers," *IEEE Transactions on Robotics*, vol. 29, no. 3, pp. 615–624, 2013.

[154] C. Budd and F. Dux, "Chattering and related behaviour in impact oscillators," *Philosophical Transactions of the Royal Society of London. Series A: Physical and Engineering Sciences*, vol. 347, no. 1683, pp. 365–389, 1994.

[155] P. J. Holmes, "The dynamics of repeated impacts with a sinusoidally vibrating table," *Journal of Sound and Vibration*, vol. 84, no. 2, pp. 173–189, 1982.

[156] T. Nishikawa and A. E. Motter, "Symmetric states requiring system asymmetry," *Physical Review Letters*, vol. 117, no. 11, p. 114 101, 2016.

[157] Y. Zhang, T. Nishikawa, and A. E. Motter, "Asymmetry-induced synchronization in oscillator networks," *Physical Review E*, vol. 95, no. 6, p. 062 215, 2017.

[158] B. Garbin, J. Fatome, G.-L. Oppo, M. Erkintalo, S. G. Murdoch, and S. Coen, "Asymmetric balance in symmetry breaking," *Physical Review Research*, vol. 2, no. 2, p. 023 244, 2020.

[159] R. M. Murray, Z. Li, and S. S. Sastry, *A Mathematical Introduction to Robotic Manipulation*. CRC Press, 2017.

[160] S. Zhao, A. Halder, and T. Kalmár-Nagy, "Leader-follower dynamics for unicycles," in *2009 American Control Conference*, IEEE, 2009, pp. 1610–1615.

[161] S. Zhao, A. Halder, and T. Kalmár-Nagy, "Nonlinear dynamics of unicycles in leader–follower formation," *Communications in Nonlinear Science and Numerical Simulation*, vol. 14, no. 12, pp. 4204–4219, 2009.

[162] K. S. Galloway, E. W. Justh, and P. S. Krishnaprasad, "Symmetry and reduction in collectives: Cyclic pursuit strategies," *Proceedings of the Royal Society A: Mathematical, Physical and Engineering Sciences*, vol. 469, no. 2158, p. 20 130 264, 2013.

[163] K. S. Galloway, E. W. Justh, and P. S. Krishnaprasad, "Symmetry and reduction in collectives: Low-dimensional cyclic pursuit," *Proceedings of the Royal Society A: Mathematical, Physical and Engineering Sciences*, vol. 472, no. 2194, p. 20 160 465, 2016.

[164] C. Bass, S. Ramasamy, and R. L. Hatton, "Characterizing error in noncommutative geometric gait analysis," in *2022 International Conference on Robotics and Automation (ICRA)*, IEEE, 2022, pp. 9845–9851.

[165] D. Martin, D. Seara, Y. Avni, M. Fruchart, and V. Vitelli, "An exact model for the transition to collective motion in nonreciprocal active matter," arXiv preprint arXiv:2307.08251, 2023.

[166] F. Wilczek, "Gauge symmetry in shape dynamics," in *Dialogues Between Physics and Mathematics: CN Yang at 100*, Cham: Springer International Publishing, 2022, pp. 227–240.

[167] F. Nédélec, T. Surrey, A. C. Maggs, and S. Leibler, "Self-organization of microtubules and motors," *Nature*, vol. 389, no. 6648, pp. 305–308, 1997.

[168] M. Doi and S. F. Edwards, *The Theory of Polymer Dynamics* (International Series of Monographs on Physics). Oxford University Press, 1986, vol. 73.

[169] K. Kremer and G. S. Grest, "Dynamics of entangled linear polymer melts: A molecular-dynamics simulation," *The Journal of Chemical Physics*, vol. 92, no. 8, pp. 5057–5086, 1990.

[170] D. Ma, J. Chen, S. Cutler, and K. Petersen, "Smarticle 2.0: Design of scalable, entangled smart matter," in *International Symposium on Distributed Autonomous Robotic Systems*, Cham: Springer Nature Switzerland, Nov. 2022, pp. 509–522.

[171] W. Savoie, *Arduinosmarticle*, https://github.com/wsavoie/ArduinoSmarticle, Accessed: 2025-04-09.

[172] A. Vardhan, *Local glider simulation*, https://github.com/AkashVardhan7/Local_Glider_Simulation, Accessed: 2025-04-09.

[173] *Project chrono*, https://projectchrono.org/, Accessed: 2025-04-09.

[174] A. Tasora and D. Negrut, "A compliant contact formulation based on differential variational inequalities," *Journal of Computational Physics*, 2010.

[175] S. Heyn and A. Tasora, "Comparison of contact solvers for rigid body dynamics in chrono," in *Proceedings of the ASME IDETC/CIE*, 2017.

[176] A. Pazouki *et al.*, "Compliant contact versus rigid contact: A comparison in the context of granular dynamics," *Physical Review E*, vol. 96, no. 4, p. 042 905, 2017.

[177] *Feedback stabilization of sterically unstable glider mode*, https://drive.google.com/file/d/1PB33gacRS1ePVxkEq-mZxw4W4aEeYNek/view?usp=sharing, Accessed: 2025-04-09.

[178] JWR, *Parking a car and lie brackets*, https://www2.math.upenn.edu/~wziller/Math600F19/parking_a_car.pdf, Accessed: 2025-04-09, 2012.

[179] E. Nelson, *Tensor Analysis*. Princeton University Press, 1967, Accessed: 2025-04-09.

[180] S. Routley, *How to parallel park your car: Another mystery solved with theory of lie groups*, *Medium*, Accessed: 2025-04-09, 2023.

[181] H. Choset and H. Lyness, *Non-holonomic constraints and lie brackets*, Lecture notes, Carnegie Mellon University, Accessed: 2025-04-09, 2023.